In-Depth Study of the Surface of Water

ISBN 978-94-92323-06-4

Cover design: Simona Strazdaitė and Mykolas Parulskis

In-Depth Study of the Surface of Water

ACADEMISCH PROEFSCHRIFT

ter verkrijging van de graad van doctor
aan de Universiteit van Amsterdam
op gezag van de Rector Magnificus
prof. dr. ir. K. I. J. Maex
ten overstaan van een door het College voor Promoties ingestelde
commissie, in het openbaar te verdedigen in de Agnietenkapel
op woensdag 21 december 2016, te 10:00 uur

door

Simona Strazdaitė

geboren te Plungė, Litouwen

Promotiecommissie

Promotor:	
prof. dr. H.J. Bakker	Universiteit van Amsterdam
Overige leden:	
dr. N.E. Ottosson	ARCNL
dr. B. Ensing	Universiteit van Amsterdam
prof. dr. W.J. Buma	Universiteit van Amsterdam
prof. dr. J.T.M. Kennis	Vrije University Amsterdam
prof. dr. F.G. Mugele	University of Twente
prof. dr. S. Woutersen	Universiteit van Amsterdam

Faculteit der Natuurwetenschappen, Wiskunde en Informatica

The work described in this thesis was performed at the FOM Institute AMOLF, Science Park 104, 1098 XG Amsterdam, The Netherlands. This work is part of the research programme of the *Stichting Fundamenteel Onderzoek der Materie* (FOM), which is financially supported by the *Nederlandse Organisatie voor Wetenschappelijk Onderzoek* (NWO).

This thesis is based on the following publications:

S. Strazdaite, J. Versluis, E.H.G. Backus and H.J. Bakker. Enhanced ordering of water at hydrophobic surfaces. *J. Chem. Phys. 140*, 054711 1-5 (2014). *(Chapter 4)*

S. Strazdaite, J. Versluis and H.J. Bakker. Water orientation at hydrophobic interfaces. *J. Chem. Phys. 143(8)*, 084708-6 (2015). *(Chapter 4)*

S. Strazdaite, J. Versluis and H.J. Bakker. The interplay of electrostatic interactions and hydrophobic hydration at the surface of tetra-n-alkylammonium bromide solutions. *J. Phys. Chem. C 120 (31)*, 17290–17295 (2016). *(Chapter 5)*

S. Strazdaite, K. Meister and H.J. Bakker. Orientation of polar molecules near charged protein interfaces. *Phys. Chem. Chem. Phys. 18 (10)*, 7414-7418 (2016). *(Chapter 6)*

S. Strazdaite, J. Versluis, N. Ottosson and H.J. Bakker. Absolute orientation of methylguanidinium at water/air interface *To be submitted (Chapter 7)*

S. Strazdaite, K. Meister and H.J. Bakker. Surface pK_a of amino-acids at water surfaces *To be submitted (Chapter 8)*

Other publications by the same author:

K. Meister, S. Strazdaite, A.L. DeVries, S. Lotze, L.L.C. Olijve, I.K. Voets, H.J. Bakker Observation of ice-like water layers at an aqueous protein surface. *Proc. Natl. Acad. Sci. USA 111 (50)*, 17732-17736 (2014).

L. Liu, S. Strazdaite, H.J. Bakker Strong isotope effect in the vibrational response of the hydration shells of hydrophobic ions. *J. Phys. Chem. C 119 (49)*, 27363-27369 (2015).

Contents

1

Introduction

> *If life can be considered as a massive self-assembly process, then water seems to be a major driving force behind it.*[1]

I could not think of a better quote to begin my PhD thesis entitled *In-Depth Study of the Surface of Water*. Water's necessity and remarkable properties are witnessed in all major classes of biomolecules. For instance, the carrier of our genetic information, deoxyribonucleic acid (DNA), is only functional when its surface is fully covered with water.[2]

All biomolecules need water to acquire their functional structure and function.[3] Lipids in aqueous environments spontaneously rearrange into bilayers in order to shield their hydrophobic aliphatic tails from the solvent. The resulting bilayers form the cell membranes, that separate the cell from its environment, and that form the matrix of many of the cell's biological functions.[4] Carbohydrates, such as glucose, are the most important energy source in human cells. Due to its high solubility in water, glucose can easily pass through the cell membrane into the cell with the assistance of transport channels.[4] Finally, proteins, the molecules that have so many diverse functions in the cells, require hydration water to be biologically active.[5]

Therefore it may seem surprising that until the 1980s, water's role in the functioning of biomolecules was not well recognized. Giorgio Careri was one of the pioneers who proposed that the protein structure and function is controlled by a network of water molecules.[6,7] Nowadays water's role in biology is widely accepted and an actively discussed topic.[3,6,8–10] A central idea is that the layer of water molecules hydrating a biomolecule influences the function and activity of the biomolecule, and that these interfacial water molecules have different properties from those in bulk water due to the interaction with the biomolecule. Water molecules, 'trapped' inside a protein structure have also been observed, and it was suggested that these water molecules play an important role in the protein's function.[11,12]

The reason for water's unique properties and its possibility to strongly interact with several biomolecules lies in its ability to form a complex three-

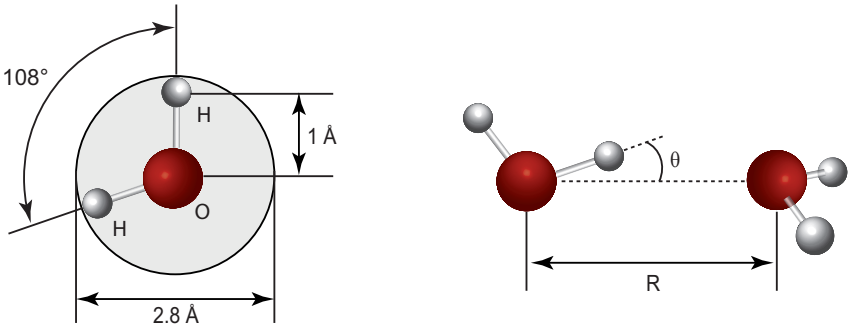

FIGURE 1.1. Geometry of a water molecule (left) and the structure of a hydrogen-bond (right).

dimensional hydrogen bonding network. A water molecule consists of two hydrogen atoms that are covalently bounded to oxygen atoms. The hydrogen atoms are slightly positively charged, whereas the oxygen atom is negatively charged, resulting in a molecule with a dipole. The positive hydrogen atom is attracted by the negative oxygen atom of another water molecule, resulting in the formation of a hydrogen bond between the two water molecules. A water hydrogen bond has a binding energy of ∼6 kcal/mol, which corresponds to ∼10 k_BT at room temperature (25°C). This implies that a hydrogen bond is relatively weak compared to a chemical bond. A hydrogen bond becomes stronger when the distance (R) between the oxygen atoms decreases and/or when the angle (θ) between the O–H and the O$\cdots$O coordinates decreases (Figure 1.1). Each water molecule can donate and accept two hydrogen bonds. Energetically it is most favourable when the four hydrogen bonds arrange tetrahedrally around each water molecule. In frozen water, i.e. ice, the hydrogen-bonding network is nearly defect-free and thus the molecules are arranged in a nearly perfect tetrahedral order. In contrast to ice, liquid water forms a disordered network of hydrogen-bonds. Hydrogen bonds are constantly being broken and reformed on a picosecond timescale. This fast reorganization of hydrogen bonds adds to the uniqueness of the water as a solvent. Water can rapidly re-arrange and adapt to structural changes of a biomolecule.

THE HYDROPHOBIC EFFECT Water can solvate many different compounds (polar molecules, salts, etc.), thanks to its polar nature and its ability to accept and donate hydrogen bonds. However, apolar molecules such as hydrocarbons or oil show a very low solubility in water. Such compounds are typically described as hydrophobic. The fact that oil does not mix with water is not very special in itself, as many other compounds such as hexane and ethylene glycol also do not mix with each other. However, the reason why the latter two compounds do not mix with each other is very different from the reason why water and oil do not mix.

A process of mixing two different liquids is governed by the Gibbs free energy,

TABLE I. Thermodynamic properties for the solvation of small hydrocarbons in water, based on solubilities at 298 K temperature.[13]

Compound	*Formula*	ΔG^0_{mix} kJ/mol	ΔH^0_{mix} kJ/mol	$T\Delta S^0_{mix}$ J/deg mol
Benzene	C_6H_6	19.33	2.08	-57.8
Toluene	C_7H_8	22.82	1.73	-70.7
Ethyl benzene	C_8H_{10}	26.19	2.02	-81.1
Propyl benzene	C_9H_{10}	28.8	2.3	-88.9
Pentane	C_5H_{12}	28.62	-2.0	-102.7
Cyclohexane	C_6H_{12}	28.13	-0.1	-94.7
Hexane	C_6H_{14}	32.54	0.0	-109.1

which contains two terms, enthalpy and entropy: $\Delta G_{mix} = \Delta H_{mix}$ - $T\Delta S_{mix}$. In the context of mixing, the change in free energy represents the reversible work for the solvent to reorganize and solvate molecules. Mixing will be spontaneous if the free energy will be negative. It is clear from the Gibbs equation that mixing is favored by entropy and that the tendency of mixing increases with temperature. The enthalpy can be viewed as the net potential energy of the interactions between all molecules. Two compounds do not mix, if they have more favorable interactions among themselves than with the other compound. In this case the enthalpic part overcomes the entropic tendency to mix and such a process is named as an enthalpy-driven process. The change in enthalpy upon mixing explains why, for example, hexane and ethylene glycol do not mix.

Mixing hydrophobic molecules with water is a different case, which becomes clear by looking at the solubilities of various hydrocarbon compounds as shown in Table I. The enthalpies of solvating hydrocarbons are around zero or even negative, which means that the enthalpy favors mixing. However, the entropic part is negative, which means that it favors de-mixing. Hence, the dependence of mixing and separation on enthalpy and entropy is exactly opposite to what we would expect for a 'normal' mixing process.

In 1945, Frank and Evans explained the decrease in entropy upon adding hydrophobic compounds to water by proposing the so-called iceberg model.[14] In this model water molecules form an ordered structure around hydrophobic solute, resembling that of ice. Such an ordering of water molecules has a negative associated entropy. The relatively favorable enthalpy of solvating hydrophobic molecule suggests that water molecules in the first solvation shell form stronger hydrogen bonds than in bulk water. Moreover, due to the decrease in entropy, hydrophobic molecules tend to cluster in water to minimize their surface area. When less surface area is exposed, fewer water molecules experience a loss of conformational entropy. This tendency of clustering of hydrophobic molecules in water is called the hydrophobic effect. Kauzmann refined this idea of entropic attraction between hydrophobic molecules and proposed its importance in protein folding.[15]

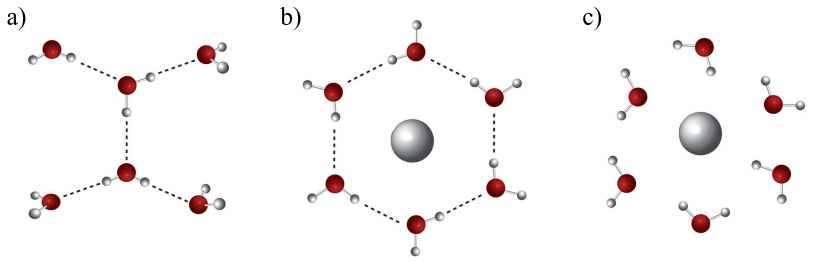

FIGURE 1.2. 'Iceberg' model proposed by Frank and Evans. Water hydrogen-bond network without hydrophobic solute (a). Water solvating hydrophobic solute at room temperature – water molecules form ordered 'ice-like' structures (b), which become disordered 'vapour-like' at higher temperatures (c).

Recent theoretical works predicted that the solvation of hydrophobic solutes is a more complex process that undergoes a transition depending on the size of the hydrophobic molecule.[16,17] Small hydrophobic solutes, with a radius smaller than a nanometer, maintain an intact hydrogen-bonded network of water molecules around them. In this situation, the hydrogen bonds between the water molecules are strengthened thus partly compensating the loss of entropy. When the solute is larger than a nanometer, the hydrogen-bond network of water gets disrupted, and the free energy is minimized by forming vapour-like water layers around the solute, which increases the entropy.

The hydrophobic effect is considered to be one of the major driving forces for protein folding, self-assembly, micelle formation and other processes. Most biologically relevant molecules like fatty acids and proteins, contain both hydrophobic and hydrophilic parts. When these molecules are immersed in water, they tend to organize in such a way that the hydrophobic parts are shielded from the interaction with water, while the hydrophilic parts are exposed to water. This structural re-arrangement forms an essential step in the formation of the functional conformation of the biomolecule.

SPECTROSCOPY OF BIOLOGICAL SYSTEMS Various techniques have been used to study the hydration of biomolecules. These techniques include spectroscopic approaches such as dielectric relaxation,[18–21] nuclear magnetic resonance,[22–24] infrared absorption,[25–28] and Raman spectroscopy,[29–31] and structural techniques like X-ray diffraction,[32–35] and neutron scattering.[35,36] Since usually only a small amount of water, the interfacial water, is directly affected by a biomolecule, it is experimentally difficult to selectively probe the structure and hydrogen-bonding of water in contact with biomolecules, and in particular the water structure around hydrophobic molecules. In the latter case the low solubility of hydrophobic molecules presents an additional challenge to study the hydration water.

One particularly promising and versatile technique for studying water surrounding biomolecules is vibrational sum-frequency generation spectroscopy

(VSFG). In VSFG spectroscopy, an infrared (IR) and a visible (VIS) beam are combined at an interface to generate light at their sum-frequency. The generated VSFG electric field depends on the second-order nonlinear susceptibility ($\chi^{(2)}$) and the electric fields of incoming VIS and IR beams. The sum-frequency signal is enhanced when the IR beam is resonant with a molecular vibration at the interface. This technique relies on the second-order nonlinear response of the sytem under study, and thus has an intrinsic surface specificity due to the fact that the second-order nonlinear response is only non-zero in non-centrosymmetric media. Thus, with VSFG one does not have difficulties separating the interfacial signal from the signal arising from the isotropic bulk medium.

VSFG spectroscopy is still a relatively new technique, but the number of reported studies with this technique rapidly increases. The first VSFG spectra were reported by Shen and coworkers in 1987, and involved a study of hydrocarbon monolayers adsorbed to glass and water.[37] Not much later Harris *et al.*[38] reported VSFG data of molecular monolayers on metal and semiconductor surfaces.

The VSFG spectrum of the surface of neat water was measured a few years later by Superfine *et al.*[39] In this pioneering work it was shown that the VSFG signal from bulk water is negligible, and that the VSFG signal indeed only represents the spectrum of the interfacial molecules. Over the years, the principles of the VSFG technique remained the same, but various more advanced VSFG variations have emerged. First, a broad-band VSFG has been developed,[40] which enabled to cover a broad vibrational region of interest with a single infrared pulse (for example, the region of the hydrogen-bonded O—H stretch vibrations of water). Another major advancement was the development of phase-sensitive (also called heterodyne-detected VSFG) technique[41] that allows the measurement of the absolute orientation of molecules at the interface. Further recent developments include time-resolved[42–44] and two-dimensional VSFG experiments.[45–47]

One of the most widely studied system by VSFG is the surface of neat water.

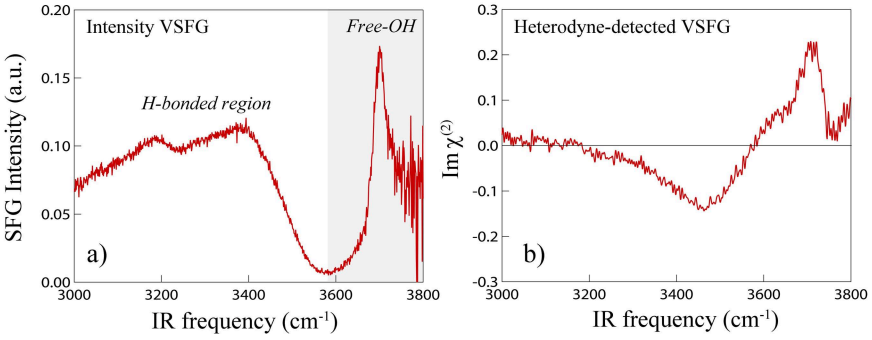

FIGURE 1.3. Intensity VSFG spectrum (a) and heterodyne-detected VSFG spectrum (b) of the water/air interface.

Despite its apparent simplicity, this is still one of the most discussed systems in the literature.[48] The first VSFG spectra measured by Superfine *et al.*[39] were reproduced by many other groups.[49] The measured spectra show a prominent peak at $\sim$3700 cm^{-1}, that can be unambiguously assigned to water molecules with one non-hydrogen bonded OH group sticking into the air. In addition, two broad, strongly overlapping bands with maxima at $\sim$3200 cm^{-1} and $\sim$3400 cm^{-1} have been observed (see Figure 1.1 a). For more than a decade, these two peaks have been assigned to "ice-like" and "water-like" hydrogen-bonded molecules, because of the resemblance to the IR absorption spectrum of ice and liquid water, respectively.[50–52] However, VSFG experiments on isotopically diluted H_2O/HDO system demonstrated that the double-peak shape disappears upon isotopic dilution.[53,54] If the peaks would have corresponded to two distinct hydrogen-bonded water species, the two-peak structure should have remained after isotopic dilution. It was thus proposed that the double-peak shape structure in the hydrogen-bonded region spectra may result from intramolecular coupling of the symmetric stretch to the bending overtone,[54] or from intermolecular coupling of O—H stretch vibrations located on different H_2O molecules.[55] Both interactions vanish upon isotopic dilution, in agreement with the observation that the double-peak structure vanishes.

The development of new phase-resolved VSFG[56] (and heterodyne-detected VSFG[57]) techniques provided additional information on the interfacial structure of water. It enabled the determination of the imaginary part of the second-order susceptibility (Im $\chi^{(2)}$), whereas in previous intensity VSFG experiments only the square of the amplitude of the second-order susceptibility ($|\chi^{(2)}|^2$) was measured. The measurement of Im $\chi^{(2)}$ with phase-resolved VSFG reveals the orientation of the water molecules at the surface. Again three peaks were observed in the Im$\chi^{(2)}$ spectra of water/air as shown in Figure 1.1 b). A narrow positive free-OH band at 3700 cm^{-1}, a negative band at $\sim$3400 cm^{-1} and a weak positive broad band at $\sim$3100 cm^{-1}. The molecular origin of the broad band at $\sim$3100 cm^{-1} has been extensively discussed,[58,59] but recently it was concluded that the weak positive band most likely arises from an artefact associated with the phase inaccuracy in PS-VSFG (or HD-VSFG) measurements.[60] Moreover, MD simulations provide an invaluable understanding of peak origins in the VSFG spectra and structure of interfacial water. There are many different theoretical approaches in simulating VSFG spectra, and in all cases the experimental spectra of the water/air interface was reproduced qualitatively.[61–65] A detailed review on MD simulations of the liquid interfaces can be found in reference.[66] Theoretical works revealed that different hydrogen-bonded species overlap spectrally, and that the biggest contribution to the hydrogen-bonded region and free-OH region comes from water molecules with a single donor and a single acceptor hydrogen bond.[59]

In this thesis we employ VSFG and heterodyne-detected VSFG to study neat liquid water and other, more complex aqueous interfaces. We focus in particular on hydrophobe/water interfaces to study the structure of water in contact with hydrophobic molecules. VSFG forms an ideal technique to study hydrophobe/water interfaces. With most other spectroscopic techniques the

signal is dominated by the bulk, which implies that water-hydrophobe interactions can only be studied using amphiphilic molecules (for example alcohols) containing both hydrophobic and hydrophilic groups (to make them soluble in water). With VSFG it is possible to probe the interface of water and a layer of hydrophobic molecules with extremely high surface specificity. We thus study the properties of water near a layer of oil. We also investigate the surfaces of aqueous solutions of hydrophobic ions, and biologically relevant molecules like proteins and amino-acids.

Outline of this Thesis The following two chapters cover the theoretical background and experimental aspects of the work described in the later chapters of this thesis. In Chapter 2 we describe the origin of a nonlinear polarization response and how this response can lead to sum-frequency generation of the incoming light fields. The anharmonic oscillator model is presented to illustrate the origin and resonant nature of the second-order nonlinear susceptibility. We also explain how the measured spectra can be used to determine the orientation of molecular groups at the surface. In Chapter 3, we describe the intensity VSFG and the heterodyne-detected VSFG setups used for the experiments. We also explain the methods of data analysis.

After introducing the relevant theoretical and experimental characteristics in Chapters 2 and 3, the following chapters describe the results of different VSFG studies on interfaces of aqueous solutions. Chapter 4 presents the most fundamental system studied in this thesis - a hydrophobic layer of alkanes and a hydrophobic polymer PDMS on a water surface. Using both VSFG and HD-VSFG techniques, we investigate how the water structure and the hydrogen-bonding are affected due to the presence of a hydrophobic layer. In Chapter 5, we investigate the structure of water at the surface of aqueous tetra-n-alkylammonium salt solutions. Tetra-n-alkylammonium salts have been widely used as a hydrophobic model system.[67] We probe the surface of different tetra-n-alkylammonium salt solutions to determine the relative importance of hydrophobic and electrostatic interactions on the water structure. In Chapter 6 we study the pH-dependent orientation of water and urea molecules at α-lactalbumin protein interfaces. In Chapter 7 we apply HD-VSFG to investigate the absolute orientation of methylguanidinium at the water surface. In Chapter 8 we study the difference in acidity of amino-acids at the water surface and in bulk water.

2

Theory and its Implementation

In this thesis, vibrational sum-frequency generation spectroscopy has been employed to study various molecular systems. Findings of those experiments are described in the following chapters. An overall understanding of the VSFG technique and the theoretical background is needed to comprehend those results. In this chapter, the fundamental theory of a nonlinear response is presented, as well as equations of the sum-frequency generation and its properties. Also an implementation of VSFG for a molecular orientational analysis is described in detail.

2.1 The Origin of Nonlinear Polarization

All spectroscopic experiments are based on the interaction of light with matter. If the intensity of the light is low, the light-induced response of a material depends linearly on the intensity of the incident light. This is the linear optical regime that includes processes such as reflection and refraction. If the intensity is sufficiently high, the optical response of a material will include terms that depend on higher orders of the incident light intensity. This is the regime of nonlinear optics. For example, second-harmonic generation is a nonlinear optical process for which the intensity of the generated light is proportional to the square of the incident light intensity. Nonlinear interactions with a material provide insight into the molecular structure and properties of the material.

The nonlinear interaction between light and matter can be described using classical mechanics, which provides a very intuitive picture of when and why nonlinear optical behavior arises. In a classical picture, a material is considered to consist of negative and positive particles: the electrons and the ions. When an electric field is applied, the charges are displaced from their positions in opposite directions, thus creating induced electric dipoles. As a result, the material becomes polarized. In case the material has no dispersion, and the response is instantaneous, the induced polarization $\mathbf{P}(t)$ can be written as a power series in terms of the applied electric field $\mathbf{E}(t)$:

$$\mathbf{P}(t) = \varepsilon_0(\chi^{(1)}\mathbf{E}(t) + \chi^{(2)}\mathbf{E}^2(t) + \chi^{(3)}\mathbf{E}^3(t) + ...) \tag{2.1}$$

where $\chi^{(1)}$ is the linear susceptibility, and $\chi^{(2)}$ and $\chi^{(3)}$ are the second-order and

third-order susceptibilities, respectively. $\mathbf{P}^2(t) = \varepsilon_0 \chi^{(2)} \mathbf{E}^2(t)$ will be referred to as the second-order nonlinear polarization.

The induced nonlinear polarization in the material acts as a source for new frequency components to be emitted. For instance, in the case of incident electric fields at frequencies of ω_1 and ω_2, due to the nonlinearity, each induced dipole will oscillate at frequencies (ω_1 - ω_2), (ω_1 + ω_2) as well at $2\omega_1$ and $2\omega_2$ (it will be shown in the following section) and will radiate an electric field at those frequencies, which will interfere constructively or destructively depending on the relative phase between each radiated field.

For an unmagnetized material with no free charges and currents, the propagation of light is expressed by the wave equation in its general form:

$$\nabla^2 \tilde{\mathbf{E}} + \frac{1}{c^2} \frac{\partial^2}{\partial t} \tilde{\mathbf{E}} = -\frac{4\pi}{c^2} \frac{\partial^2}{\partial t} \left(\mathbf{P}_{\mathrm{L}} + \mathbf{P}_{\mathrm{NL}} \right) \tag{2.2}$$

where $\tilde{\mathbf{E}}$ is the electric field, $\mathbf{P}_{\mathrm{L}}$ is the linear polarization, and $\mathbf{P}_{\mathrm{NL}}$ is the nonlinear polarization. The wave equation describes the dispersive propagation, creation, amplification, and attenuation of the electric field resulting from the linear and nonlinear polarization of the material. From the wave equation one can derive coupled-wave equations, which describe how the amplitudes of the newly produced electric field and the incident electric fields change as a result of the nonlinear interaction. The derivation of coupled-wave equations for the case of frequency-mixing processes can be found in reference.[68]

THE ANHARMONIC OSCILLATOR MODEL FOR THE SECOND-ORDER NONLINEAR SUSCEPTIBILITY The linear optical properties of a material like the refractive index and the absorption coefficient, can be described as the response of a driven harmonic oscillator. To explain nonlinear optical phenomena this description can be extended to the response of an anharmonic oscillator. The equation of motion for an anharmonic oscillator driven by an electric field is:

$$m \left[\frac{\partial^2 x}{\partial t} + 2\gamma \frac{\partial x}{\partial t} + \omega_0^2 x - (ax^2 + bx^3 + ...) \right] = -e\mathbf{E}(t) \tag{2.3}$$

where x is the displacement from the mean position of the oscillator, ω_0 is the resonance frequency and γ is a damping constant. The right-hand term represents the force exerted by the electric field. The terms $ax^2 + bx^3 + ...$ on the left-hand side describe the anharmonicity, obtained by assuming that the restoring force is a nonlinear function of the displacement of the electron from its equilibrium position. When considering only the first quadratic nonlinear term, the restoring force will be given by:

$$\mathbf{F}_{\mathrm{restoring}} = -m\omega_0^2 x + max^2 \tag{2.4}$$

which corresponds to a potential energy:

$$U = -\int \mathbf{F}_{\mathrm{restoring}} dx = \frac{1}{2} m\omega_0^2 x^2 - \frac{1}{3} max^3 \tag{2.5}$$

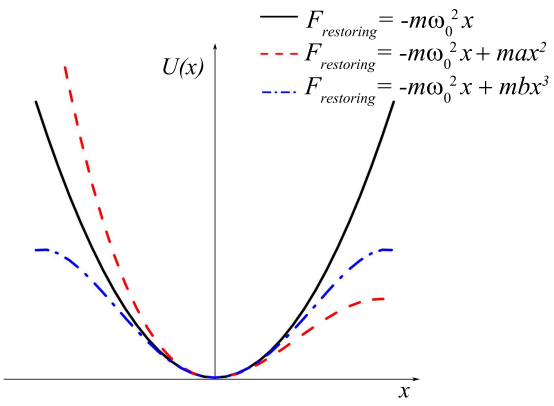

FIGURE 2.1. Schematic picture of the potential energy function for a harmonic oscillator (black line). Two cases for an anharmonic oscillator are shown: when the restoring force has linear and quadratic components (red dashed line) and when the restoring force has linear and cubic components (blue dot-dashed line).

For a cubic term in the restoring force expression ($\mathbf{F}_{\text{restoring}} = -m\omega_0^2 x + mbx^3$), the potential energy equals:

$$U = \frac{1}{2}m\omega_0^2 x^2 - \frac{1}{4}mbx^4 \tag{2.6}$$

Figure 2.1 shows the potential energy of a harmonic oscillator, and of anharmonic oscillators in case a quadratic (Eq. 2.5) or cubic (Eq. 2.6) anharmonicity term is included in the restoring force. The potential when quadratic term is included is not symmetric in x, which means that $U(x) \neq U(-x)$. Hence, the presence of anharmonic terms with even powers of x implies that the material is non-centrosymmetric medium. For a centrosymmetric medium the potential must not change the sign when the axis is reversed, $U(x) = U(-x)$. This can be achieved only when the anharmonicity contains terms with odd powers of x.

We now look at the case of a non-centrosymmetric medium. We will later see that such a medium gives rise to a second-order nonlinearity and is responsible for sum-frequency generation. In this case Equation 2.3 can be written as:

$$m\left[\frac{\partial^2 x}{\partial t} + 2\gamma\frac{\partial x}{\partial t} + \omega_0^2 x - ax^2\right] = -e\mathbf{E}(t) \tag{2.7}$$

The applied electric field can be expressed as a sum of two monochromatic electric fields oscillating at frequencies ω_1 and ω_2:

$$\mathbf{E}(t) = E_1 e^{-i\omega_1 t} + E_2 e^{-i\omega_2 t} + c.c. \tag{2.8}$$

Equation 2.7 can be solved with a perturbation expansion, assuming that the applied electric field is weak and that the anharmonic term is much smaller

than the linear term. The solution of Eq. 2.7 can then be written in the form of a power series:

$$x = x^{(1)} + x^{(2)} + x^{(3)} + ... \tag{2.9}$$

where $x^{(1)}$ describes the first-order solution for a harmonic oscillator:

$$\begin{aligned} x^{(1)}(\omega_i) &= -\frac{e}{m}\frac{E_i}{D(\omega_i)}, \\ D(\omega_i) &= \omega_0 - \omega_i - 2i\omega_i\gamma \end{aligned} \tag{2.10}$$

The second-order solution $x^{(2)}$ will contain terms at frequencies $2\omega_1$, $2\omega_2$, $\omega_1 + \omega_2$, $\omega_1 - \omega_2$ and 0. The solution at sum-frequency $\omega_1 + \omega_2$ is given by:

$$x^{(2)}(\omega_1 + \omega_2) = -\frac{2a(e/m)^2 E_1 E_2}{D(\omega_1 + \omega_2)D(\omega_1)D(\omega_2)} \tag{2.11}$$

Solutions for other frequency terms can be found in reference.[68] The relation between the displacement $x^{(2)}$ and the second-order susceptibility can be obtained by considering that the n-th order polarization represents the sum of all induced dipoles:

$$\mathbf{P}^{(n)} = -Nex^{(n)} \tag{2.12}$$

where n is 1, 2,..., and N is the number of atoms. By comparing this expression with Eq. 2.1, 2.10 and 2.11, we obtain expressions for the different susceptibilities. The second-order susceptibility is given by:

$$\chi^{(2)}(\omega_1 + \omega_2) = \frac{Na(e^3/m^2)^2}{D(\omega_1 + \omega_2)D(\omega_1)D(\omega_2)} \tag{2.13}$$

From the presence of the D terms in the denominator of Equation 2.13, it follows that the second-order susceptibility becomes large when the resonance frequency of the anharmonic oscillator equals ω_1 or ω_2 or $\omega_1 + \omega_2$. An expression for the nonlinear susceptibility can also be derived with a quantum-mechanical model for the material response. In this case the susceptibilities follows from a perturbation expansion of the time-dependent Schrödinger equation. In such a description the anharmoncity coefficient a is replaced by products of transition dipole moments between the quantum-mechanical levels of the material. A full derivation can be found in the literature.[37,68] The quantum-mechanical model shows the same resonance behavior near the transition energies between the levels as the classical model near the resonance frequency of the anharmonic oscillator.

2.2 SUM-FREQUENCY GENERATION

The origin of the sum-frequency generation can be demonstrated in a simple electromagnetic approach by considering two incident electric fields, oscillating at frequencies ω_1 and ω_2. Their sum can be written as:

$$\begin{aligned}\mathbf{E}(t) &= 2\mathbf{E}_1\cos(\omega_1 t) + 2\mathbf{E}_2\cos(\omega_2 t)\\ &= \mathbf{E}_1(e^{-i\omega_1 t} + e^{i\omega_1 t}) + \mathbf{E}_2(e^{-i\omega_2 t} + e^{i\omega_2 t})\end{aligned} \tag{2.14}$$

Taking only the second order non-linear polarization $\mathbf{P}^2(t) = \varepsilon_0\chi^{(2)}\mathbf{E}^2(t)$, and substituting the sum of the electric fields leads to:

$$\begin{aligned}\mathbf{P}^{(2)}(t) = \varepsilon_0\chi^{(2)}[&\mathbf{E}_1^2(e^{-i2\omega_1 t} + e^{i2\omega_1 t}) +\\ &\mathbf{E}_2^2(e^{-i2\omega_2 t} + e^{i2\omega_2 t}) +\\ &2\mathbf{E}_1\mathbf{E}_2(e^{-i(\omega_1+\omega_2)t} + e^{i(\omega_1+\omega_2)t}) +\\ &2\mathbf{E}_1\mathbf{E}_2(e^{-i(\omega_1-\omega_2)t} + e^{i(\omega_1-\omega_2)t}) +\\ &2(\mathbf{E}_1^2 + \mathbf{E}_2^2)]\end{aligned} \tag{2.15}$$

Therefore two incident electric fields give rise to second-harmonic generation (SHG) at frequencies $2\omega_1$ and $2\omega_2$, sum-frequency generation (SFG, highlighted term) $\omega_1 + \omega_2$, difference-frequency generation (DFG) at $\omega_1 - \omega_2$, and the creation of a DC field (no frequency dependence), denoted as optical rectification.

Omitting the time dependence of the electric fields, the polarization at the sum-frequency is given by:

$$\mathbf{P}_{\mathrm{SF}}^{(2)} = \varepsilon_0\chi^{(2)}\mathbf{E}_1\mathbf{E}_2 \tag{2.16}$$

In vibrational sum-frequency generation spectroscopy, one of the incident beams is chosen to be resonant with the vibrations of molecules, which will lead to an enhancement of the second-order susceptibility $\chi^{(2)}$, as illustrated in Equation 2.13. The second beam is fixed at a visible frequency.

From the conservation of momentum it follows that the sum-frequency wavevector is the sum of the infrared and visible beam wavevectors:

$$\mathbf{k}_{\mathrm{VIS}} + \mathbf{k}_{\mathrm{IR}} = \mathbf{k}_{\mathrm{SF}} \tag{2.17}$$

When the beams are not propagating collinearly, the conservation of momentum in the x-direction will be given by:

$$n_{\mathrm{VIS}}\omega_{\mathrm{VIS}}\sin\eta_{\mathrm{VIS}} + n_{\mathrm{IR}}\omega_{\mathrm{IR}}\sin\eta_{\mathrm{IR}} = n_{\mathrm{SF}}\omega_{\mathrm{SF}}\sin\eta_{\mathrm{SF}} \tag{2.18}$$

where η_{VIS} and η_{IR} are the incident angles of the VIS and IR beams respectively. The generated SF signal is reflected from the surface at an angle η_{SF}. This is called the phase matching condition. For clarity reasons, it is important to

mention that there will also be SF signal generated in the transmission direction, as depicted in Figure 2.2. However, in our experimental setup we always detect the reflected SF beam.

2.3 The Effective Susceptibility and Fresnel Factors

Equation 2.16 fully describes the process of sum-frequency generation. However, the probed second-order susceptibility (named here as $\chi^{(2)}_{\text{eff}}$, effective susceptibility) depends on the experimental geometry, such as the incident angles of the beams and their polarizations. Thus, to understand the magnitude of the generated VSFG signal it is important to define the dependence of $\chi^{(2)}_{\text{eff}}$ on the experimental geometry as expressed in the surface bound co-ordinates (also called laboratory co-ordinates).

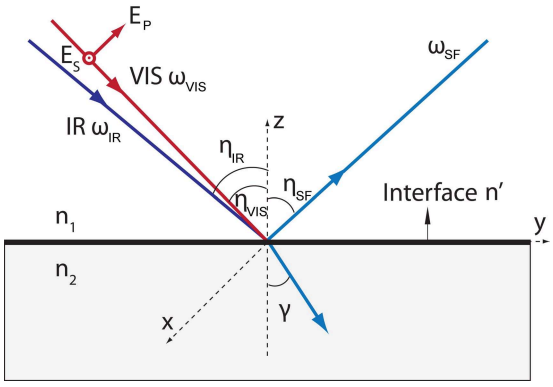

FIGURE 2.2. Geometry for VSFG generation in the surface fixed laboratory co-ordinate system. The incident and emitted beams are depicted and propagate in the yz plane.

In general, $\chi^{(2)}$ is a third-rank tensor with 27 components in the laboratory co-ordinate system, $\chi^{(2)}_{ijk}$. When considering an induced polarization in the i direction, and $\mathbf{E}$ fields in the j and k directions Equation 2.16 can be written as:

$$\mathbf{P}^{(2)}_{i,\text{SF}} = \varepsilon_0 \chi^{(2)}_{ijk} \mathbf{E}_{j,\text{VIS}} \mathbf{E}_{k,\text{IR}} \tag{2.19}$$

In a centrosymmetric environment, the value of $\chi^{(2)}$ for opposing directions should be identical since all directions are equivalent:

$$\chi^{(2)}_{ijk} = \chi^{(2)}_{-i-j-k} \tag{2.20}$$

However, as a third rank tensor, a change in the sign of all three axes is equivalent to reversing the system axis:

$$\chi^{(2)}_{-i-j-k} = -\chi^{(2)}_{ijk} \tag{2.21}$$

In order to satisfy both equations Eq. 2.20 and 2.21, $\chi^{(2)}_{ijk}$ must be zero. Hence, for centrosymmetric media $\chi^{(2)}_{ijk} = 0$. Only at the surface of a centrosymmetric medium the centrosymmetry will be broken, which explains the intrinsic surface specificity of VSFG for centrosymmetric bulk media.

In order to find the relation between effective susceptibility $\chi^{(2)}_{\text{eff}}$ and macroscopic susceptibility $\chi^{(2)}_{ijk}$ we define the laboratory coordinates with the z-axis as the surface normal and xy as the surface plane (see Figure 2.2). All beams are defined to propagate in the yz plane. P denotes a polarization of the optical field in the yz plane, and S denotes a polarization, along the x axis, i.e. perpendicular to the yz plane.

Of the total number of 27 macroscopic susceptibility tensor elements $\chi^{(2)}_{ijk}$ ($(i,j,k) = (x,y,z)$) only 7 can be non-zero in view of the symmetry constraints of an achiral rotationally isotropic interface with $C_{\infty\nu}$ symmetry (see Appendinx A for a more detailed derivation). The nonzero elements are:

$$\chi^{(2)}_{xxz} = \chi^{(2)}_{yyz}, \chi^{(2)}_{xzx} = \chi^{(2)}_{yzy}, \chi^{(2)}_{zxx} = \chi^{(2)}_{zyy}, \chi^{(2)}_{zzz}. \tag{2.22}$$

Overall there are thus only four independent non-zero $\chi^{(2)}_{ijk}$ components, since the x and the y axes are equivalent for an isotropic surface. These four components can be deduced by measuring VSFG with different input and output polarization combinations, such as SSP (S polarized VSFG, S polarized VIS and P polarized IR), SPS, PSS and PPP. From Figure 2.2 one can see that P-polarized light has components along the y and the z axis, while S-polarized light has only a component in x. Using the SSP polarization configuration only one tensor element will be probed $\chi^{(2)}_{xxz}$, while with SPS and PSS polarization combinations $\chi^{(2)}_{xzx}$ and $\chi^{(2)}_{zxx}$ tensor elements will be probed, respectively. Using a PPP polarization configuration, a mix of all non-zero tensor elements will be measured. For the above mentioned polarization configurations, $\chi^{(2)}_{\text{eff}}$ is related to the four non-zero macroscopic susceptibilities in the following way:

$$\begin{aligned}
\chi^{(2),\text{SSP}}_{\text{eff}} =& L_{yy}(\omega_{\text{SF}})L_{yy}(\omega_{\text{VIS}})L_{zz}(\omega_{\text{IR}})\sin\eta_{\text{IR}}\chi^{(2)}_{xxz} \\
\chi^{(2),\text{SPS}}_{\text{eff}} =& L_{yy}(\omega_{\text{SF}})L_{zz}(\omega_{\text{VIS}})L_{yy}(\omega_{\text{IR}})\sin\eta_{\text{VIS}}\chi^{(2)}_{xzx} \\
\chi^{(2),\text{PSS}}_{\text{eff}} =& L_{zz}(\omega_{\text{SF}})L_{yy}(\omega_{\text{VIS}})L_{yy}(\omega_{\text{IR}})\sin\eta_{\text{SF}}\chi^{(2)}_{zxx} \\
\chi^{(2),\text{PPP}}_{\text{eff}} =& -L_{xx}(\omega_{\text{SF}})L_{xx}(\omega_{\text{VIS}})L_{zz}(\omega_{\text{IR}})\cos\eta_{\text{SF}}\cos\eta_{\text{VIS}}\sin\eta_{\text{IR}}\chi^{(2)}_{xxz} \\
& -L_{xx}(\omega_{\text{SF}})L_{zz}(\omega_{\text{VIS}})L_{xx}(\omega_{\text{IR}})\cos\eta_{\text{SF}}\sin\eta_{\text{VIS}}\cos\eta_{\text{IR}}\chi^{(2)}_{xzx} \\
& +L_{zz}(\omega_{\text{SF}})L_{xx}(\omega_{\text{VIS}})L_{xx}(\omega_{\text{IR}})\sin\eta_{\text{SF}}\cos\eta_{\text{VIS}}\cos\eta_{\text{IR}}\chi^{(2)}_{zxx} \\
& +L_{zz}(\omega_{\text{SF}})L_{zz}(\omega_{\text{VIS}})L_{zz}(\omega_{\text{IR}})\sin\eta_{\text{SF}}\sin\eta_{\text{VIS}}\sin\eta_{\text{IR}}\chi^{(2)}_{zzz}
\end{aligned} \tag{2.23}$$

where $L_{ii}(i = x,y,z)$ are the Fresnel coefficients that are determined by the

refractive indices of the two media ($n_1(\omega_i)$, $n_2(\omega_i)$) and the refractive index of the interfacial layer ($n^{'}(\omega_i)$), and the incident angles (η_{VIS} and η_{IR}), reflected angle (η_{SF}) and the angles of transmission (γ_i):

$$\begin{aligned} L_{xx}(\omega_i) =& \frac{2n_1(\omega_i)cos\gamma_i}{n_1(\omega_i)cos\gamma_i + n_2(\omega_i)cos\eta_i} \\ L_{yy}(\omega_i) =& \frac{2n_1(\omega_i)cos\eta_i}{n_1(\omega_i)cos\eta_i + n_2(\omega_i)cos\gamma_i} \\ L_{zz}(\omega_i) =& \frac{2n_2(\omega_i)cos\eta_i}{n_1(\omega_i)cos\gamma_i + n_2(\omega_i)cos\eta_i}\left(\frac{n_1(\omega_i)}{n^{'}(\omega_i)}\right)^2 \end{aligned} \tag{2.24}$$

where i denotes VIS, IR or SF beams.

The Fresnel factors act as a correction of the amplitude of each electric field when the beams propagate across the boundary that separates two isotropic media. A detailed derivation of all three tensorial Fresnel factors has been presented by Shen *et al.*[69,70] The only unknown parameter in the Fresnel expressions is the refractive index of the interfacial layer $n^{'}(\omega_i)$, which enters in the expression of $L_{zz}(\omega_i)$. The refractive index of the interfacial layer may be different from the bulk refractive index of the bulk medium at the same frequency. This issue will be discussed further in Chapter 7.

The Fresnel factors affect the spectral shape and intensity of the measured VSFG spectra. Thus ideally, all spectra should be corrected for Fresnel factors when comparing different VSFG spectra. Recently, Feng *et al.* have shown that the water/air spectra from different research groups are quantitatively consistent when corrected for the Fresnel factors.[49] However, due to the complexity of data processing, most VSFG studies only report the measured $\chi^{(2)}_{\mathrm{eff}}$. In this thesis, the Fresnel factors are only explicitly accounted for in Chapter 7, where we determine the orientation of molecular groups. In the remaining chapters the presented VSFG spectra are not corrected for the Fresnel factors. We do normalize the spectra with respect to the spectral dependence of the incident IR beam by dividing the measured VSFG spectra by the SFG spectrum obtained from a reference (non-resonant) quartz crystal.

2.4 Relation between the Susceptibility to the Molecular Hyperpolarizability

The measured $\chi^{(2)}$ is an overall average of the molecular hyperpolarizabilities β of all probed molecules at the interface. As we saw in the previous chapter the experimentally determined $\chi^{(2)}_{\mathrm{eff}}$ is defined in the co-ordinates of the surface (or laboratory) system. However, molecular hyperpolarizabilities are defined in the molecular axes system, which do not necessarily coincide with the surface axes. Most molecules at the interface are oriented at a certain angle (or a distribution of angles) with respect to the surface normal (z-axis). The relation

between the two coordinate systems can be described with the three Euler angles (ψ, ϕ, θ) and applying three rotation matrices. The macroscopic susceptibility $\chi^{(2)}_{ijk}$ can thus be expressed in term of the molecular hyperpolarizability $\beta_{i'j'k'}$ ($(i', j', k') = (a, b, c)$ denotes molecular co-ordinates):

$$\chi^{(2)}_{ijk} = \frac{N_S}{\epsilon_0} \sum_{i'j'k'} \langle R_{ii'} R_{jj'} R_{kk'} \rangle \beta_{i'j'k'} \tag{2.25}$$

where N_S is the number of the molecules probed at the interface. $R_{\lambda\lambda'}$ is the element of the rotational transformation matrix that is used to convert the molecular system to the surface co-ordinate system.

The ensemble average is expressed as:

$$\langle R_{ii'} R_{jj'} R_{kk'} \rangle = \frac{\int_0^\pi \int_0^{2\pi} \int_0^{2\pi} R_{ii'} R_{jj'} R_{kk'} f(\theta, \phi, \psi) \sin\theta d\theta d\phi d\psi}{\int_0^\pi \int_0^{2\pi} \int_0^{2\pi} f(\theta, \phi, \psi) \sin\theta d\theta d\phi d\psi} \tag{2.26}$$

where $f(\theta, \phi, \psi)$ is the molecular orientation distribution function. Typically a Gaussian function is used to describe a broader angular distribution of $f(\theta, \phi, \psi)$. The $\sin\theta$ enters the ensemble average to account for the volume element. The detailed description of the Euler transformation can be found in Goldstein's book *Classical Mechanics*[71] and have also been worked out by Hirose *et al.*[72, 73]

The molecular hyperpolarizability tensor elements of a particular vibrational mode q are proportional to the derivatives of Raman polarizability ($\alpha_{i'j'}$) and dipole moment ($\mu_{k'}$) tensor elements:[74]

$$\beta_{i'j'k'} = -\frac{1}{2\varepsilon_0 \omega_q} \frac{\partial \alpha_{i'j'}}{\partial Q_q} \frac{\partial \mu_{k'}}{\partial Q_q} \tag{2.27}$$

where ω_q is the resonant frequency and Q_q is the normal coordinate of the q-th vibrational mode. Therefore, a vibrational mode has to be Raman and IR active in order to be VSFG active.

The relation between $\chi^{(2)}_{ijk}$ and $\beta_{i'j'k'}$ can be simplified by using the symmetry properties of the molecular vibration under study. The molecular symmetry determines which of the molecular hyperpolarizability tensor $\beta_{i'j'k'}$ are non-zero. The non-zero elements for most common symmetries, i.e. $C_{3\nu}$, $C_{2\nu}$ and $C_{\infty\nu}$, as well expressions for the resulting macroscopic susceptibility tensor elements can be found in the literature.[75–78]

2.4.1 Expressions of the Macroscopic Susceptibilities for $C_{3\nu}$ Symmetry Group

In this section we will consider a special case – the methyl group with $C_{3\nu}$ symmetry. We define a molecular co-ordinate system, such that the c-axis is along the symmetry axis of the $C_{3\nu}$ methyl group, and the a and b axes form a plane perpendicular to c-axis. The a-axis runs along the projection of one

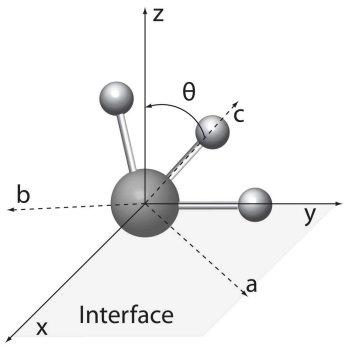

FIGURE 2.3. Schematic representation of a methyl group adsorbed at the interface. The surface and molecular bound axis are shown.

of the C–H bonds in the *ab* plane (see Figure 2.3). There are eleven non-zero molecular hyperpolarizability elements for a methyl group, three for the symmetric stretching vibration and eight for the antisymmetric:

$$\begin{aligned} \mathrm{CH_{3,SS}}: &\beta_{aac} = \beta_{bbc}, \beta_{ccc} \\ \mathrm{CH_{3,AS}}: &\beta_{aca} = \beta_{bcb}, \beta_{caa} = \beta_{cbb}, \beta_{aaa} = -\beta_{bba} = -\beta_{abb} = -\beta_{bab} \end{aligned} \tag{2.28}$$

In Appendix B a method for determining the non zero hyperpolarizability elements for a molecular group with $C_{3\nu}$ symmetry is presented.

The macroscopic susceptibility elements for a rotationally isotropic surface can be obtained by integration over the two Euler angles (ϕ and ψ), which will reduce their angle dependence to the angle θ only,[75] where θ is the tilt angle between the methyl C_3 axis and surface normal z. For the symmetric stretching vibration this procedure yields:

$$\begin{aligned} \chi^{(2),\mathrm{SS}}_{xxz} =& \frac{1}{2} N_s \beta^{(2)}_{ccc} [(1+R)\langle cos\theta\rangle - (1-R)\langle cos^3\theta\rangle] \\ \chi^{(2),\mathrm{SS}}_{xzx} =& \chi^{(2),\mathrm{SS}}_{zxx} = \frac{1}{2} N_s \beta^{(2)}_{ccc} (1-R)[\langle cos\theta\rangle - \langle cos^3\theta\rangle] \\ \chi^{(2),\mathrm{SS}}_{zzz} =& N_s \beta^{(2)}_{ccc} [(R)\langle cos\theta\rangle + (1-R)\langle cos^3\theta\rangle] \end{aligned} \tag{2.29}$$

and for the asymmetric vibration:

$$\begin{aligned} \chi^{(2),\mathrm{AS}}_{xxz} =& - N_s \beta^{(2)}_{aca} (\langle cos\theta\rangle - \langle cos^3\theta\rangle) \\ \chi^{(2),\mathrm{AS}}_{xzx} =& \chi^{(2),\mathrm{AS}}_{zxx} = N_s \beta^{(2)}_{aca} \langle cos^3\theta\rangle] \\ \chi^{(2),\mathrm{AS}}_{zzz} =& 2 N_s \beta^{(2)}_{aca} (\langle cos\theta\rangle - \langle cos^3\theta\rangle) \end{aligned} \tag{2.30}$$

where the hyperpolarizability ratio $R = \beta^{(2)}_{aac}/\beta^{(2)}_{ccc}$ of the methyl group is known to be in the range of 1 to 4 for different molecules.[74]

Using the equations presented in this section and in the previous one, the experimentally measured VSFG intensity in different polarization combinations can be directly related to the molecular hyperpolarizability elements $\beta_{i'j'k'}$. Hence, if all parameters (such as the refractive indexes of a medium and the interface) and R value are known, then the orientation of the molecules can be quantitatively extracted from the VSFG spectra. In Chapter 7 this formalism will be applied to determine the absolute orientation of methylguanadinium ions at the water surface.

2.5 The Macroscopic Susceptbility of Water

In this thesis, a major focus lies in determining the orientation of water molecules at various solution interfaces. As described earlier, the macroscopic second-order susceptibility $\chi^{(2)}_{\text{eff}}$ is an average of the molecular hyperpolarizabilities β_{ijk} and holds all the information on the average molecular orientation. It consists of real and imaginary parts, and the sign of the imaginary part is related to an average orientation of the molecules at the interface. The measurement of the imaginary and real parts of the second-order susceptibility with heterodyne-detected VSFG technique will be described in the next chapter. Here, the relationship between the sign of the $\chi^{(2)}$ and the net orientation of water molecules is explained.

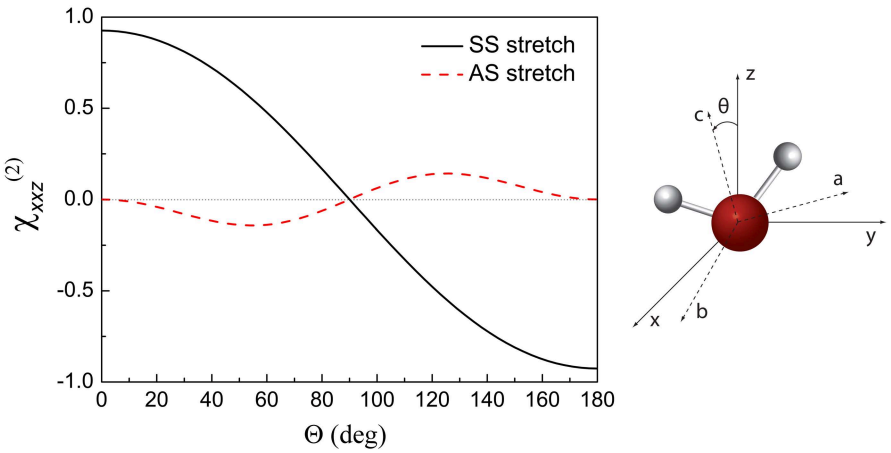

FIGURE 2.4. $\chi^{(2)}_{xxz}$ tensor element for the symmetric and asymmetric stretch vibrations of water molecule with $C_{2\nu}$ symmetry.

Water molecules can be considered to possess $C_{2\nu}$ symmetry, unless the two O–H bonds are very asymmetrically hydrogen bonded (for example, in the

case of the free OH group). In the latter case the O–H bonds have to be treated separately with $C_{\infty\nu}$ symmetry. For $C_{2\nu}$ symmetry the macroscopic second-order susceptibilities in the xxz combination (that is probed with an SSP polarization configuration) for symmetric and asymmetric vibrations are given by:[79]

$$\chi^{(2),\mathrm{SS}}_{xxz} = \frac{1}{4}N_s(\beta^{(2)}_{aac} + \beta^{(2)}_{bbc} + \beta^{(2)}_{ccc})\langle cos\theta\rangle + \frac{1}{4}N_s(\beta^{(2)}_{aac} + \beta^{(2)}_{bbc} - 2\beta^{(2)}_{ccc})\langle cos^3\theta\rangle$$
$$\chi^{(2),\mathrm{AS}}_{xxz} = -\frac{1}{2}N_s\beta^{(2)}_{aca}(\langle cos\theta\rangle - \langle cos^3\theta\rangle) \tag{2.31}$$

The molecular co-ordinates are defined such that the O atom is located at the co-ordinate centre, the molecule plane is in the ac plane, and the c-axis is along the C_2 symmetry axis. The angle θ is the angle between the surface normal or z-axis of the laboratory co-ordinate frame and the molecular c-axis. The hyperpolarizability tensor elements of the water molecule have been reported by Gen *et al.*:[79] $\beta_{aac} = 1.296$, $\beta_{bbc} = 0.557$, $\beta_{ccc} = 1$, $\beta_{aca} = \beta_{caa} = 0.741$, and $\beta_{bcb} = \beta_{cbb} = 0$. Figure 2.4 shows the $\chi^{(2)}_{xxz}$ for the symmetric and asymmetric stretch of a water molecule (Fresnel factors are not included in this plot). It is clear from this figure, that the symmetric stretch is dominant in the SSP polarization combination, and that $\chi^{(2)}_{xxz}$ is positive when $0^\circ \leqslant \theta \leqslant 90^\circ$ and negative when $90^\circ \leqslant \theta \leqslant 180^\circ$. In other words, when $\chi^{(2)}_{xxz}$ is positive, the water molecules have an average orientation with both hydrogen atoms into the air phase.

2.6 The Non-Resonant Second-Order Susceptibility

So far we only described the second-order susceptibility originating from the resonant behavior of interfacial molecules. However, there are also non-resonant contributions, and the overall second-order susceptibility of the interface is the sum of both:

$$\chi^{(2)} = \chi^{(2)}_{\mathrm{NR}} + \chi^{(2)}_{\mathrm{R}} = A_{\mathrm{NR}}e^{i\phi} + \sum_q \frac{A_{\mathrm{R}}}{\omega_{\mathrm{IR}} - \omega_q + i\Gamma_q} \tag{2.32}$$

in this equation, $\chi^{(2)}_{\mathrm{NR}}$ and $\chi^{(2)}_{\mathrm{R}}$ are the effective non-resonant (NR) and resonant (R) susceptibilities, respectively. A_{NR} is the non-resonant amplitude, A_{R} is the resonant amplitude, and ϕ is the phase difference between the resonant and non-resonant signals. ω_q and Γ_q represent the frequency and width of the q-th vibration. The resonant contribution is the sum of the responses of all vibrations q. Thus, the measured VSFG intensity is proportional to:

$$I_{\mathrm{VSFG}} \propto |\chi^{(2)}_{\mathrm{NR}} + \chi^{(2)}_{\mathrm{R}}|^2 = |\chi^{(2)}_{\mathrm{NR}}|^2 + |\chi^{(2)}_{\mathrm{R}}|^2 + 2|\chi^{(2)}_{\mathrm{NR}}||\chi^{(2)}_{\mathrm{R}}|cos(\delta(\omega)) \tag{2.33}$$

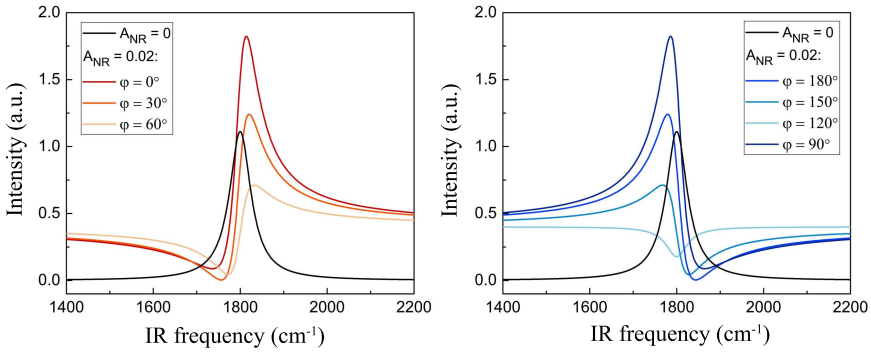

FIGURE 2.5. Lineshapes of a single resonance (1800 cm^{-1}) when it interfers with a non-resonant background of the same amplitude, but different phases.

where $\delta(\omega)$ is a frequency-dependent phase term that accounts for the phase difference between the resonant and non-resonant signals (determined by ϕ, ω_{IR} and ω_q). This interference term leads to distortions of the measured VSFG spectrum, which can affect its interpretation.

The interference between resonant and non-resonant signals is particularly problematic when molecules are adsorbed on a metal substrate,[80] as metal surfaces give significant non-resonant signals. However, even for molecules on dielectric substrates with small non-resonant signals (for example fused silica), the spectrum can be heavily distorted as the effect of the non-resonant term gets amplified due to the cross-term in Eq. 2.33. Lagutchev *et al.* have developed a method using a Fabry-Pèrot etalon to suppress the contribution of the non-resonant background.[81] Applying this method, Curtis *et al.* have demonstrated that VSFG spectra of thin polystyrene films on three different substrates (silicon, fused silica and sapphire) are identical.[80] In VSFG spectra of liquid interfaces, a non-resonant background is also observed, but no definite conclusion has been reached about the origin of this non-resonant background. Recently, it was shown using electronic heterodyne-detected SFG, that the non-resonant background of the SFG spectrum of water is predominantly due to a quadrupole contribution from the bulk.[82]

Figure 2.5 illustrates how the spectral shape of the VSFG spectrum changes due to the interference with the non-resonant background. In this figure the resonance is centered at 1800 cm^{-1}, and $A_{\text{R}} = 1$, $\Gamma = 30$ cm^{-1}, $A_{\text{NR}} = 0.02$, and the phase ϕ was varied from 0° to 180°.

THE NON-RESONANT SFG SIGNAL FROM QUARTZ A z-cut α-quartz crystal is commonly used as a normalization standard in VSFG measurements, as its non-resonant response is spectroscopically flat in a broad spectral range from UV to mid-IR.

When we wish to compare the intensities of VSFG spectra measured with

different polarization combinations, and that are normalized by the SFG response of quartz, we need to know the effective susceptibilities of quartz in those polarization combinations. The relations between the effective second-order susceptibilities and macroscopic β_{ijk} elements for crystalline quartz can be derived in a similar manner as for the $C_{3\nu}$ symmetry group. Unfortunately, there have been some inconsistencies in these relations presented in the literature,[83,84] but recently Fu *et al.* have published revised and detailed relations.[85]

The α-quartz[0001] crystal unit cell has a threefold symmetry (D_3) and has four non-zero achiral polarizability tensor elements:

$$\beta_{aaa} = \beta_{abb} = \beta_{bcb} = \beta_{bbc}. \tag{2.34}$$

where the crystal coordinates are defined in such a way that the c-axis is along the [0001] axis, the b-axis along the two fold axis, and $a \perp b$. The effective second-order susceptibilities of quartz in SSP and PPP polarization configurations are given by:

$$\begin{aligned} \chi_{\text{eff}}^{(2),\text{SSP}} &= -L_{yy}(\omega_{\text{SF}})L_{yy}(\omega_{\text{VIS}})L_{xx}(\omega_{\text{IR}})cos\eta_{\text{IR}}\beta_{aaa}cos(3\phi) \\ \chi_{\text{eff}}^{(2),\text{PPP}} &= -L_{xx}(\omega_{\text{SF}})L_{xx}(\omega_{\text{VIS}})L_{xx}(\omega_{\text{IR}})cos\eta_{\text{SF}}cos\eta_{\text{VIS}}cos\eta_{\text{IR}}\beta_{aaa}cos(3\phi) \end{aligned} \tag{2.35}$$

here ϕ is the azimuthal rotation angle around the z-axis and η_i are the incident angles of the VIS, IR and VSFG beams. A complete derivation is given in the reference.[85]

2.A Appendix: $\chi_{ijk}^{(2)}$ Elements for an Isotropic Surface

The non-zero $\chi_{ijk}^{(2)}$ elements for an isotropic surface can be deduced by taking the fundamental tensor rule into consideration (Eq. 2.20). Reversing the direction of any individual axis leads to a change of the $\chi_{ijk}^{(2)}$ sign. However, for an isotropic surface with $C_{\infty\nu}$ symmetry x = -x and y = -y while z $\neq$ -z. This means with reversal of the x or y axis, $\chi_{ijk}^{(2)}$ must not change its sign. For instance, when reversing the x-axis, $\chi_{xzz}^{(2)}$ element becomes $\chi_{-xzz}^{(2)}$. From the fundamental tensor rule it follows that $\chi_{-xzz}^{(2)}$ should be equal to -$\chi_{xzz}^{(2)}$, meaning that $\chi_{xzz}^{(2)}$ must be zero. When the x-axis is reversed for $\chi_{xxz}^{(2)}$, we obtain $\chi_{-x-xz}^{(2)}$ = -$\chi_{x-xz}^{(2)}$ = $\chi_{xxz}^{(2)}$. Hence, reversing the x-axis does not change the sign of $\chi_{xxz}^{(2)}$, which means that it can be non-zero. Hence, only $\chi_{ijk}^{(2)}$ elements with even number in x or y (x and y are identical for an isotropic surface) will contribute to the VSFG spectra. In addition, the $\chi_{zzz}^{(2)}$ element will contribute, because reversing the x (or y) axis has no effect on this element. As a result, the interface with $C_{\infty\nu}$ symmetry has only four independent non-zero $\chi_{ijk}^{(2)}$ elements:

$$\chi_{xxz}^{(2)} = \chi_{yyz}^{(2)}, \chi_{xzx}^{(2)} = \chi_{yzy}^{(2)}, \chi_{zxx}^{(2)} = \chi_{zyy}^{(2)}, \chi_{zzz}^{(2)}. \tag{2.36}$$

2.B APPENDIX: MOLECULAR HYPERPOLARIZABILITY ELEMENTS FOR $C_{3\nu}$ SYMMETRY

$\beta_{i'j'k'}$ has a total number of 27 elements. In order to find which elements are non-zero for a particular molecular group, one needs to consider its symmetry operations.[86] $C_{3\nu}$ has in total 6 symmetry operations: the identity operation (E), the two 3-fold rotational axis ($C_{3\nu}$) and three mirror planes (σ_ν). Figure 2.6 shows a methyl group, which has $C_{3\nu}$ symmetry and for which we will apply all three symmetry operations to deduce which elements can be non-zero.

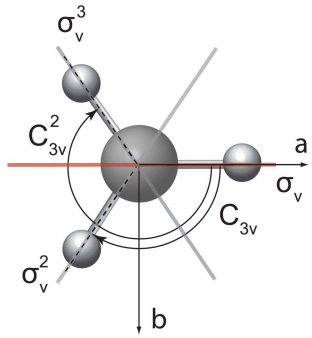

FIGURE 2.6. Schematic structure of a methyl group with the corresponding molecular axis and its symmetry opperations.

- From Figure 2.6 it is clear that the mirror plane (marked in red) divides the methyl group in two equal parts, hence the b-axis is equal to the $-b$-axis. Now the same argumentation applies as previously for isotropic surface (Appendix 2.A): only $\beta_{i'j'k'}$ with even number of b's can be non-zero.

- After a C_3 rotation the molecular co-ordinates change to:

$$\begin{aligned} a &= a\cos\theta + b\sin\theta \\ b &= -a\sin\theta + b\cos\theta \qquad (2.37) \\ c &= c \end{aligned}$$

(2.38)

We will first consider the β_{acc} element. After a C_3 rotation it becomes $\beta_{acc}cos\theta + \beta_{bcc}sin\theta$ and applying the symmetry operations leads to the following equalities:

E:	θ=0°	$\beta_{acc} = \beta_{acc}$
C_3:	θ=120°	$\beta_{acc} = -\frac{1}{2}\beta_{acc} + \frac{\sqrt{3}}{2}\beta_{bcc}$
C_3^2:	θ=240°	$\beta_{acc} = -\frac{1}{2}\beta_{acc} - \frac{\sqrt{3}}{2}\beta_{bcc}$

From the first argument we deduced that $\beta_{bcc} = 0$, thus the second and third equalities become $\beta_{acc} = -\frac{1}{2}\beta_{acc}$ and this can be true only if $\beta_{acc} = 0$. Using an analogous formulation, one can show that all $\beta^{(2)}_{i'j'k'}$ with only one a element are zero: $\beta_{acc} = \beta_{cac} = \beta_{cca} = 0$.

- Let's now consider a more complex element β_{aac}, after a first C_3 rotation it becomes:

$$\beta_{aac} \xrightarrow{C_3} \beta_{aac}\cos\theta + \beta_{bac}\sin\theta \tag{2.39}$$

After a second C_3 rotation:

$$\beta_{aac} \xrightarrow{C_3^2} \beta_{aac}\cos^2\theta + \beta_{bbc}\sin^2\theta + \beta_{abc}\cos\theta\sin\theta + \beta_{bac}\sin\theta\cos\theta \tag{2.40}$$

Then:

E:	θ=0°	$\beta_{aac} = \beta_{aac}$
C_3:	θ=120°	$\beta_{aac} = \frac{1}{4}\beta_{aac} + \frac{3}{4}\beta_{bbc}$
C_3^2:	θ=240°	$\beta_{aac} = \frac{1}{4}\beta_{aac} + \frac{3}{4}\beta_{bbc}$

and from this it becomes clear that $\beta_{aac} = \beta_{bbc}$

- Further applying a rotation matrix in the same manner on other $\beta_{i'j'k'}$ elements would lead to the existing relationships between all non-zero molecular hyperpolarizability elements for a $C_{3\nu}$ group:

$$\begin{aligned}
&\beta_{aac} = \beta_{bbc}, \beta_{ccc}\\
&\beta_{aca} = \beta_{bcb}\\
&\beta_{caa} = \beta_{cbb}\\
&\beta_{aaa} = -\beta_{bba} = -\beta_{abb} = -\beta_{bab}
\end{aligned} \tag{2.41}$$

- To determine which of those elements will be active for a symmetric stretch and which for an antisymmetric stretch, one needs to look at a character table for $C_{3\nu}$ symmetry, which is shown in Table I (derived from reference[87]). From the character table one can determine which components of the dipole moment and the polarizability will be active for each vibration. The symmetric methyl stretch has a dipole moment only along the c-axis (μ_c), consequently the resonance of the symmetric stretch vibration (A_1) will only enhance $\beta_{aac} = \beta_{bbc}$, and β_{ccc}.

TABLE I. Character table of the $C_{3\nu}$ point group.[87]

$C_{3\nu}$	E	$2C_3$	$3\sigma_\nu$		
A_1	1	1	1	μ_c	$(\alpha_{aa}+\alpha_{bb}), \alpha_{cc}$
A_2	1	1	-1		
E	2	-1	0	μ_a, μ_b	$\alpha_{ac}, \alpha_{bc}, (\alpha_{aa}-\alpha_{bb}), \alpha_{ab}$

3

Experiment

In this chapter we will give a detailed description of the VSFG setups that were used to obtain the results presented in this thesis. The VSFG setup can be divided into four main parts: the femtosecond laser system, the infrared light generation, the sum-frequency generation, and the detection part.

3.1 Laser System and Infrared Light Generation

In order to induce a nonlinear response of a medium, (e.g. sum-frequency generation) an intense light source is required. Nowadays, most nonlinear optical spectroscopy systems are based on a femtosecond Ti:Sapphire laser. We use a regenerative Ti:Sapphire laser system, which consists of two parts: the amplifier (Coherent "Legend Elite Duo") and the oscillator (Coherent "Mantis"). The oscillator produces low energy pulses (∼35 fs) centered at 800 nm (bandwidth ∼80 nm (FWHM)). The femtosecond pulses generated by the oscillator are used to seed the amplifier. The used Legend Elite Duo employs a chirped pulse amplification method. The low-energy pulse is initially stretched using a single-grating pulse stretcher, in order to reduce its power. After the amplification, the pulse is re-compressed close to its original duration. The Ti:Sapphire crystal is pumped by a high-energy Nd:YLF laser, which produces 527 nm pulses (Coherent "Evolution"). The resulting pulse energy of the Ti:Sapphire laser is ∼3.5 mJ with a pulse duration of ∼35 fs at a repetition rate of 1 kHz.

The Ti:Sapphire laser can be tuned in a small range around 800 nm. In order to perform vibrational nonlinear spectroscopy experiments intense mid-infrared pulses are needed. Such wavelengths can be achieved with parametric devices based on the use of nonlinear crystals with large second-order susceptibility values, e.g. β-barium borate (BBO) and lithium triborate (LBO).

As shown in Chapter 2, the second-order susceptibility is responsible for various frequency conversion processes such as the second-harmonic generation, sum-frequency and difference-frequency generation, as well as optical parametric amplification (OPA). The OPA process can be seen as a special case of the difference-frequency generation. When a nonlinear crystal is illuminated with a strong pump pulse ω_1 and a weak signal ω_2, two new photons are emitted, one

with the frequency of the signal ω_2 and one with the new frequency ω_3, called idler. Such a process can exist only if the following two conditions are fulfilled:

$$\omega_1 = \omega_2 + \omega_3, \tag{3.1}$$
$$\boldsymbol{k}_1 = \boldsymbol{k}_2 + \boldsymbol{k}_3. \tag{3.2}$$

Here, $\boldsymbol{k}_i$ are the wave vectors of the propagating waves. The second relation is known as the phase-matching condition, and in the case that the waves propagate colinearly, it can be written as:

$$n_1(\omega_1)\omega_1 = n_2(\omega_2)\omega_2 + n_3(\omega_3)\omega_3 \tag{3.3}$$

Materials with a normal dispersion, in which the index of refraction increases with frequency, can never fulfill this relation. The phase matching condition can however be achieved by using birefringent materials. Such materials have different refractive indices for different polarization directions. By rotating a birefringent crystal (changing the angle between the optical axis of the crystal and the direction of beam propagation) the wavelength combination for which the phase matching condition is fulfilled can be changed. Thereby the optical parametric amplification can be optimized.

To get an efficient conversion and no pulse distortion (pulse lengthening) the phase matching condition must be fulfilled over the entire spectral range of the input and generated pulses. Often, the phase-matching condition is only fulfilled near the center wavelengths of the interacting pulses, leading to a distortion of the pulses and a decreased conversion efficiency. These effects can be avoided by using a short interaction length. i.e. by using thin crystals.

EXPERIMENTAL OPA IMPLEMENTATION The home-built OPA (Figure 3.1) geometry and IR light generation was implemented from P. Hamm *et al.*[88] Approximately two thirds of the Ti:sapphire laser output is used to pump an OPA to produce the signal and idler which are later combined at the difference-frequency generation (DFG) stage to generate infrared light.

Figure 3.1 shows a scheme of the used OPA system including all optical elements. The 800 nm visible beam enters the OPA system (top left) and is split in two parts by a beam splitter (BS1). A first part (reflected from BS1), which is only a few percent of the incoming 800 nm light, passes through a $\lambda/2$-plate (Λ) and a polariser (P1) and is focused with lens (L1) on a sapphire plate (S1), where white light is generated. This white light is used as a seed pulse to generate signal and idler. It is crucial that the white light is stable, which strongly depends on the intensity of the incident 800 nm light, which we can regulate by rotating the $\lambda/2$-plate. The polarization of the white light is rotated perpendicular to that of the 800 nm pulse to achieve phase matching in the nonlinear crystal. After passing the sapphire plate, the white light is collimated with a second lens (L2) and continues to travel to the BBO crystal (1 mm thick), while the remaining 800 nm is filtered out.

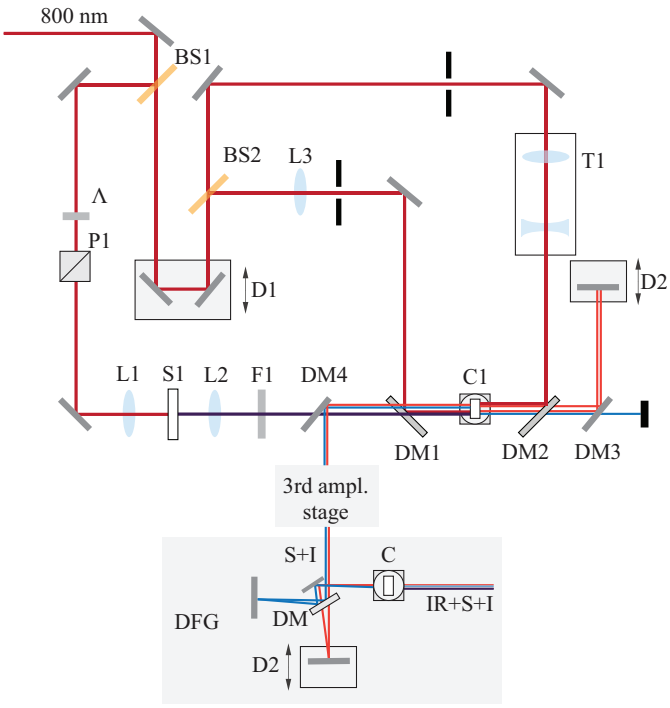

FIGURE 3.1. The principal scheme of the homebuilt optical parametric amplifier, used to generate the signal and idler, which later are combined to produce the mid-IR pulses for the VSFG experiments. Abbreviations: BS - beam splitter; Λ - $\lambda/2$-plate; L - lens; P - polariser; D - delay line; F - filter; S1 - sapphire plate; DM - dichroic mirror; C1 - β-barium borate (BBO) crystal; T - telescope; C2 - silver gallium disulphate ($AgGaS_2$) crystal; S+I - signal and idler; IR+S+I - infrared, signal and idler.

The main part of the 800 nm pulse is transmitted through BS1 and is guided into the delay stage (D1), and then onto the second beam splitter (BS2). Approximately 10% of the 800 nm is reflected and focused with a 50 mm lens into a BBO crystal, where it overlaps with the white light (first amplification stage). To generate the first signal and idler pulses, the 800 nm and white light must overlap spatially and temporally. The time overlap is adjusted with delay D1. The frequency of the signal ω_S and idler ω_I ranges between 1200 - 1600 μm and 1600 - 2400 μm, respectively.

At this stage the energy of the signal and idler pulses is only $\sim$10 μJ and to amplify it further, a second amplification stage is implemented. The idler is transmitted through a dichroic mirror and then is blocked, while the signal is reflected back by means of a refocusing mirror (DM3) mounted on a delay stage (D2). The part of the 800 nm that was transmitted by BS2 ($\sim$90 % of the incoming 800 nm pulse) is collimated using a telescope (T1). Due to the very high intensity it cannot directly be focused on the crystal as that would cause damage. After the second spatial and temporal overlap on the crystal between

the signal and the 800 nm light, the signal pulse gets amplified and meanwhile the idler pulse gets regenerated. The overall efficiency of this process can be up to ∼30 %, which results in a total energy of the signal and idler of ∼300 μJ. We further use a third amplification stage (not shown in Fig. 3.1 for simplicity reasons), to produce even higher pulse energies of the signal and idler. After the second amplification stage we again block the idler and use the signal to combine with ∼1.5 μJ of the 800 nm on a second BBO crystal. The resulting total energy of the signal and idler is ∼700 - 800 μJ.

The mid-infrared pulses are generated by combining the signal and idler in a silver gallium disulfide ($AgGaS_2$) crystal (difference-frequency mixing, DFG). To achieve an optimal temporal overlap, the signal and idler are spatially separated using a dichroic mirror. The frequency of the mid-infrared pulses can be varied by changing the orientation of the BBO and $AgGaS_2$ crystals, along with subsequent adjustments of temporal and spatial overlaps within the OPA and DFG. Hence, the center frequency of the mid-IR pulses can be tuned in the range of ∼1400 to 5000 cm^{-1} (∼2 - 7 μm). The OPA and DFG processes are most efficient in the wavelength region of ∼2800 - 3200 cm^{-1}. Pulse energies are typically in the range of ∼15 - 20 μJ with a bandwidth of ∼400 - 500 cm^{-1} (FWHM). This process is the least efficient in the amide vibrational region. In this region typical pulse energies range from ∼5 to 8 μJ with a bandwidth of ∼200 cm^{-1} (FWHM).

3.2 Vibrational Sum-Frequency Generation Spectroscopy

3.2.1 Intensity VSFG

In order to generate the sum-frequency at the sample surface two pulses are needed. A broadband mid-IR pulse sets up a coherent polarization at the interface as well as in the bulk, and a narrow band visible pulse upconverts the interfacial polarization. A broadband IR allows us to instantly probe the entire vibrational region of interest, for example the water hydrogen-bonded region (bandwidth ∼300 cm^{-1} at FWHM). The narrow band VIS pulse determines the frequency resolution of the VSFG spectrum. We use a Fabry-Pérot etalon to narrow down the initial 800 nm (bandwidth ∼12 nm at FWHM) pulse to ∼15 - 20 cm^{-1}. The etalon consists of two reflecting mirrors. One of which partially transmits light and another that is highly reflecting. The light enters the etalon and undergoes multiple internal reflections. When the reflected beams are in phase, constructive interference occurs and this results in a high transmission. The central frequency and bandwidth of the transmitted light depends on the distance between the mirrors, the refractive index of the medium between the two mirrors and on the angle at which the light enters the etalon. Thus, the central frequency of the transmitted beam can be easily varied by rotating the etalon with respect to the beam.

After passing the etalon, the 800 nm pulse has to travel approximately the

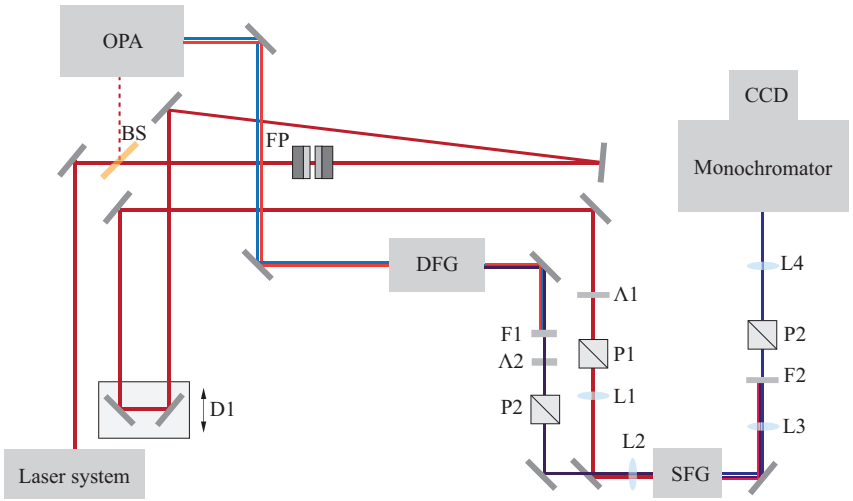

FIGURE 3.2. The principal scheme of the VSFG experiment and detection part. Approximately two thirds of the laser output (∼3.5 W) is used to pump the OPA and the DFG to produce mid-IR pulses. The remaining part is sent through an etalon to narrow down its bandwidth to ∼15 cm^{-1}. The resulting narrow-band 800 nm pulse and the broadband IR pulse are directed and focused on the sample surface, where after spatial and temporal overlap VSFG light is generated. The VSFG light is sent to a monochromator and is detected with an Electron-Multiplied Charge Coupled Device (EMCCD, Andor Technologies). Abbreviations: BS - beam splitter; FP - Fabry-Pérot etalon; Λ - $\lambda/2$-plate; P - polariser; L - lens; D - delay line; F - filter.

same distance as the IR pulse travels in the OPA and DFG (∼4 m). To make the 800 nm pulse path length longer it is sent on a few mirrors back and forth and then on a delay line (see Figure 3.2). A precise time overlap between the IR and VIS pulses at the sample position can be achieved by adjusting the delay line (D1). Before being focused on the sample, the IR and VIS beams pass through $\lambda/2$ plates and polarizers, which are used to control the polarizations. It is important to note that the polarizations at the sample position are defined with respect to the plane of incidence (perpendicular to the sample surface), whereas the generated IR pulse and also the 800 nm pulse polarizations are defined with respect to the plane in which they travel (parallel to the table). The generated IR pulse (after DFG) has P polarization in respect to the travelling plane (800 nm as well), which corresponds to S polarization with respect to the sample. The VIS and IR beams are focused using lenses with a focal length of 20 mm and 10 mm, respectively. The VIS focus is located ∼0.5 - 1 cm above the sample surface.

When a spatial and temporal overlap of the IR and VIS pulse is achieved at the sample surface, the VSFG light will be generated. The reflected VSFG signal passes through two high-pass filters to remove the remaining 800 nm light. Afterwards it passes a polarizer and is focused on the detector's slit. A

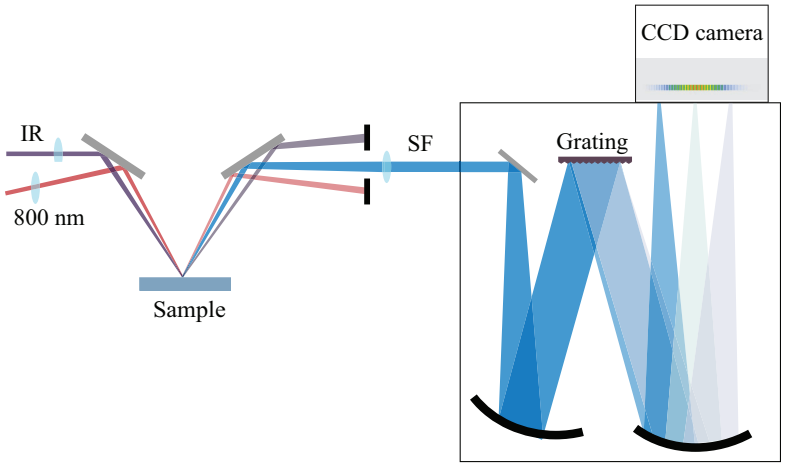

FIGURE 3.3. A schematic picture of the VSFG generation and detection. The VIS and IR pulses are focused on the sample surface, where they overlap spatially and temporally, generating the VSFG pulse that is sent to the spectrograph and detected with the EMCCD camera.

shamrock Spectrograph (Andor Technologies) is used to disperse the VSFG light into its frequency components and to focus the dispersed light on an electron multiplied charge coupled device (EMCCD, Newton 970, Andor Technologies).

3.2.2 HETERODYNE-DETECTED VSFG

In the previous section the intensity VSFG technique has been described. Using this technique the intensity of the sum-frequency light is detected, which only provides information on the absolute square of the second-order susceptibility $\chi^{(2)}$. From the intensity VSFG measurements the sign (phase) of $\chi^{(2)}$ can not be retrieved and hence information about the orientation of molecules can not be obtained. Information on the orientation can be obtained using interference based heterodyne-detected vibrational sum-frequency generation (HD-VSFG) spectroscopy.[89–91] In this technique, the VSFG electric field of the sample is combined with that of a local oscillator at the same frequency and of a known phase:

$$\begin{aligned} I_{\mathrm{SFG}} = & \mid E_{\mathrm{LO}} + E_{\mathrm{Sample}} \mid^2 = \mid E_{\mathrm{LO}} \mid^2 + \mid E_{\mathrm{Sample}} \mid^2 \\ & + E_{\mathrm{LO}} E^*_{\mathrm{Sample}} + E^*_{\mathrm{LO}} E_{\mathrm{Sample}} \end{aligned} \tag{3.4}$$

The detected VSFG intensity contains cross terms from which the real and imaginary part of $\chi^{(2)}$ can be extracted.

The experimental setup for HD-VSFG only differs from the intensity VSFG setup in the part where VSFG light is generated. The IR and VIS beams are first focused on a metal surface to create an SFG signal from a local oscillator

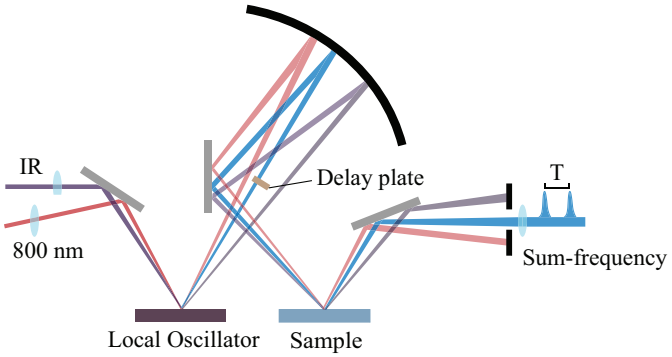

FIGURE 3.4. Experimental lay-out of the used heterodyne-detected VSFG. A broadband femtosecond IR pulse and a narrowband 800 nm pulse are focused onto a metal surface, generating an intense local oscillator SFG (LO-SFG) response that is delayed by a silica plate. The three beams are refocused on the sample surface, producing a sample VSFG signal that interferes with the LO-SFG signal on the EMCCD camera.

(LO-SFG). This LO-SFG signal originates from a strong non-resonant $\chi^{(2)}$ of the metal. We typically use a gold mirror as the local oscillator (Thorlabs model PF-10-03-M01). It should be noted though, that gold can only be used as a local oscillator for particular polarization combinations, since in the infrared region of the spectrum, metal surfaces generate a large electric field in the z direction and negligible fields in the x and y directions. As a result, the use of gold is limited to SSP and PPP polarization combinations. The spectral shape of the LO-SFG signal is a convolution of the spectra of the broad input IR pulse and the narrow-band visible pulse. This LO-SFG signal is sent through a silica plate to delay it in time with respect to the VIS and IR beams ($\sim$1.6 ps). The remaining IR and VIS beams are refocused with a spherical mirror onto the sample interface to generate the sample VSFG signal. The LO-SFG and sample VSFG beams are sent collinearly into a spectrograph and the spectral interference pattern of the two SFG beams is detected with EMCCD.

HD-VSFG experiments have been reported previously in which the LO-SFG beam was generated after the sample.[57,89] This approach has the disadvantage that the LO-SFG signal needs to be corrected for the frequency-dependent reflectivity of the sample interface in the IR spectral region.[92] In the present method such a correction is not needed, since the LO-SFG beam is created before the VSFG signal of interest, and because the LO-SFG signal beam is generated via a metal surface for which the reflection is $\sim$100% for all frequency components contained in the IR pulse. In the used geometry the LO-SFG beam is reflected from the sample interface, but for the studied samples the reflectivity of this beam does not depend on frequency within its bandwidth. The advantages of the used geometry have been realized by several groups and is now commonly used in HD-VSFG experiments.

In our HD-VSFG experiments we use z-cut quartz as a reference. It is

important that the sample and quartz crystal must be placed at the same height, as a height uncertainty would lead to an uncertainty of the extracted phase of the sample. We control the height of the reference quartz crystal and the sample by monitoring the position of the VSFG signal on the EMCCD camera. This enables us to define the SFG signal on the camera with a precision of 1 pixel size (16 x 16 µm). In combination with the used setup geometry this results in a phase uncertainty of $\sim \pi/10$ ($\sim$20°).

It is further worth mentioning that this interference based phase retrieval VSFG technique is sometimes named differently in the literature. The technique was first established by Shen *et al.* using a picosecond scanning laser system and was called phase-sensitive VSFG (PS-VSFG).[41,89,93,94] Later Tahara *et al.*[57,95] and Benderskii *et al.*[96] have implemented this method for broad-band IR systems and named it heterodyne-detected VSFG (HD-VSFG). However, some groups have argued that heterodyne-detected VSFG method should also be called phase-sensitive VSFG.[92] In this thesis I use both names interchangeably and I will call our used method heterodyne-detected VSFG.

3.2.3 Analysis of Heterodyne-Detected VSFG spectra

The heterodyne-detected VSFG technique is based on the interference between a local oscillator SFG signal and the sample VSFG signal. The LO-SFG signal is delayed in time, but when both SFG pulses enter the monochromator, they are stretched in time and thus interfere to produce a characteristic interference pattern in the frequency domain. Figure 3.5 a) shows detected raw interference pattern of which the sum of the electric field in the time domain can be written as:

$$E_{\mathrm{det}}(t) = r_{\mathrm{sample}} E_{\mathrm{LO}}(t + \Delta t) + E_{\mathrm{sample}}(t) \tag{3.5}$$

here E_{sample} is the electric field generated from the sample, E_{LO} - from the LO (gold mirror) and r_{sample} is the complex reflectivity for the electric field at the frequency ω_{VSFG} from the sample surface. Δt is the time delay induced by the silica plate.

Equation 3.5 can be written in the frequency domain using a Fourier transformation:

$$E_{\mathrm{det}}(\omega) = r_{\mathrm{sample}} E_{\mathrm{LO}}(\omega) e^{-i\omega\Delta t} + E_{\mathrm{sample}}(\omega) \tag{3.6}$$

The total detected intensity of the raw HD-VSFG spectrum is given by:

$$\begin{aligned} I_{\mathrm{det}} = &\mid r_{\mathrm{sample}} E_{\mathrm{LO}}(\omega) e^{-i\omega\Delta t} + E_{\mathrm{sample}}(\omega) \mid^2 = \\ &\mid r_{\mathrm{sample}} E_{\mathrm{LO}} \mid^2 + \mid E_{\mathrm{sample}} \mid^2 + \\ &+ r^*_{\mathrm{sample}} E^*_{LO} e^{i\omega\Delta t} E_{\mathrm{sample}} + r_{\mathrm{sample}} E_{LO} e^{-i\omega\Delta t} E^*_{\mathrm{sample}} \end{aligned} \tag{3.7}$$

The first two quadratic terms of Eq. 3.7 give rise to an intense signal at $t = 0$ (Figure 3.5 b). Cross-terms (second and third term in Eq. 3.7) are

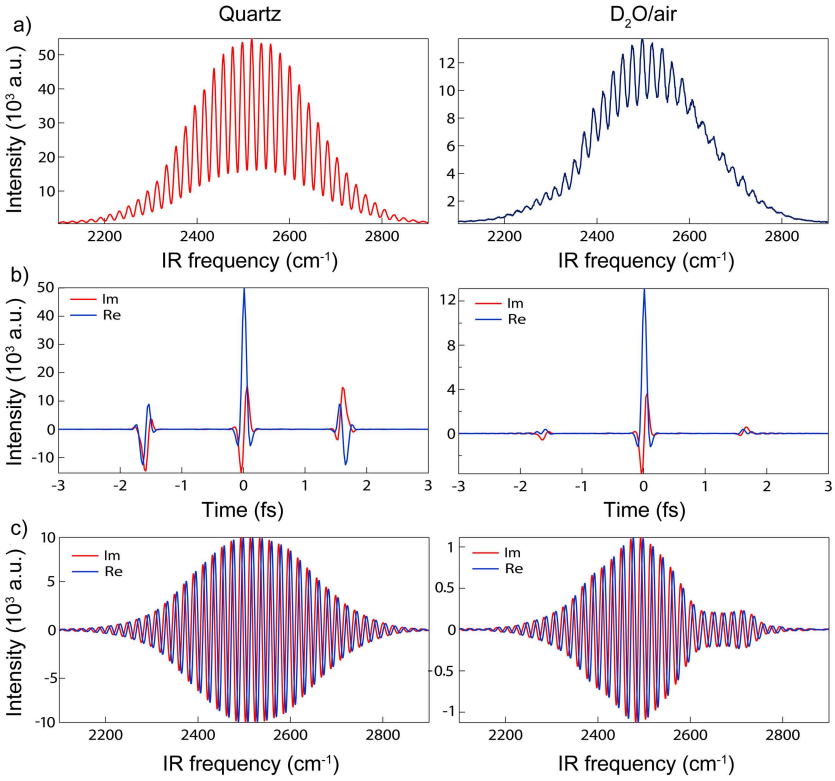

FIGURE 3.5. a) Raw detected spectra of a z-cut quartz (left) and D_2O/air interface (right). b) Fourier transformations of the detected spectra into the time domain; grey areas mark the regions, which are selected for the inverse Fourier transformation. c) Real and imaginary parts of a z-cut quarzt and D_2O/air interface in the frequency domain.

located at negative and positive times with respect to this peak. Both cross-terms contain information of the imaginary and real parts of the sample $\chi^{(2)}$. One of those components (we use the term at positive time) is extracted by filtering (Figure 3.5 b) and the resulting complex spectrum is obtained by an inverse Fourier transformation (Figure 3.5 c).

The reference SFG signal of z-cut quartz is measured under identical conditions and used to normalize the measured VSFG signal, in particular to normalize the spectrum for the spectral dependence of the broadband IR pulse. The sample interferogram is divided by the quartz interferogram, yielding the HD-VSFG signal S_{HD}:

$$S_{\mathrm{HD}} = \frac{r^*_{\mathrm{sample}} E^*_{\mathrm{LO}} e^{i\omega\Delta t} E_{\mathrm{sample}}}{r^*_{\mathrm{quartz}} E^*_{\mathrm{LO}} e^{i\omega\Delta t} i E_{\mathrm{quartz}}} \tag{3.8}$$

The imaginary factor i is included in the denominator to account for the phase difference of 90° between VSFG light generated from the sample surface and SFG light generated from the quartz bulk.[97]

The electric field of the sample and quartz are defined by the vacuum permittivity (ϵ_0), the Fresnel factors ($F_{sample/quartz}$), and the reflectivities of the VIS and IR pulses from the LO (gold), second order susceptibilities ($\chi^{(2)}_{\text{sample/quartz}}$) and the electric fields of the VIS and IR pulses (E_{IR} and E_{VIS}):

$$\begin{aligned} E_{\text{sample}} &= \epsilon_0 F_{\text{sample}} r_{LO}(\omega_{\text{VIS}}) r_{\text{LO}}(\omega_{\text{IR}}) \chi^{(2)}_{\text{sample}} E_{\text{IR}} E_{VIS} \\ E_{\text{quartz}} &= \epsilon_0 F_{\text{quartz}} r_{\text{LO}}(\omega_{\text{VIS}}) r_{\text{LO}}(\omega_{\text{IR}}) \chi^{(2)}_{\text{quartz}} E_{\text{IR}} E_{\text{VIS}} \end{aligned} \tag{3.9}$$

Substituting those expressions into Eq. (3.8) results in:

$$S_{\text{HD}} = \frac{r^*_{\text{sample}} F_{\text{sample}} \chi^{(2)}_{\text{sample}}}{r^*_{\text{quartz}} F_{\text{quartz}} i \chi^{(2)}_{\text{quartz}}} \tag{3.10}$$

The ratio of the reflection coefficients $r^*_{\text{sample}}/r^*_{\text{quartz}}$ for the electric field at the frequency ω_{VSFG} is approximately 1 (in the ~3000 cm^{-1} region). The ratio of Fresnel factors ($F_{\text{sample}}/F_{\text{quartz}}$) is also assumed to be 1, although there might be difference due to resonant character of the infrared pulse at the sample.

DETERMINATION OF THE Z-CUT QUARTZ PHASE Quartz is the most commonly used material as a reference in VSFG experiments, because it has a large and solely real $\chi^{(2)}$ response. The theoretically predicted value of the phase difference between $\chi^{(2)}$ of the water/air interface and quartz SFG signal is 90° (factor i in Eq. 3.8 and Eq. 3.10).[97] However, Wang et al. showed using second harmonic generation that the phase difference is 115° ± 15°,[49] which deviates from the theoretically predicted value by 25° ± 15°. Therefore an extra phase is sometimes used in the data analysis. In these cases Eq. 3.10 is multiplied by $e^{-i\psi}$, where $\psi \simeq 25° \pm 15°$. The exact value of this correction and if it is needed at all is currently widely debated.[60]

The exact phase of quartz can be examined by measuring the VSFG spectra of a liquid sample in a non-resonant frequency region.[60] In order to determine the precise phase of the $\chi^{(2)}$ of quartz, D_2O can be measured in the water vibrational region (~2900 – 3200 cm^{-1}). The signal in this region from D_2O will be solely non-resonant. In such a case, the imaginary part should be zero and the real part should be negative.

Figure 3.6 a) shows the real and imaginary $\chi^{(2)}$ spectra of D_2O/air interface normalized by quartz (in SSP polarization combination). When the quartz phase value is taken to be 90° (because of its bulk origin), then the imaginary part of the $\chi^{(2)}$ of D_2O/air is zero, and the real part is negative, as expected in this non-resonant frequency regime. When an extra phase of 18° is added to the quartz phase, the derived imaginary part of the $\chi^{(2)}$ of D_2O/air becomes slightly positive, which should not be the case. This result shows that there is no need to add an extra phase when quartz is used as a reference. Sometimes

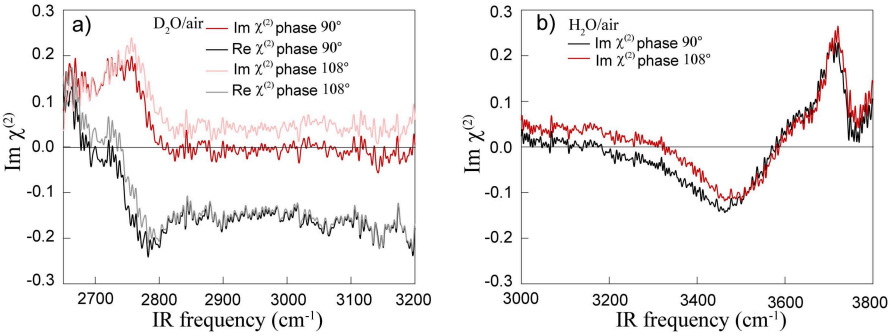

FIGURE 3.6. a) Real and imaginary $\chi^{(2)}$ spectra of the D_2O/air interface normalized by quartz using $\pi/2$ (black and red) and $\pi/2 + \pi/10$ (grey and light red) as the phase. b) Imaginary $\chi^{(2)}$ spectrum of the H_2O/air normalized by quartz with $\pi/2$ and with $\pi/2 + \pi/10$ phase.

a deviation from the exact quartz phase was observed, which might come from a contamination of the quartz surface.

Figure 3.6 b) shows the imaginary $\chi^{(2)}$ spectrum normalized by quartz with 90° phase and with a 108° phase. In section 3.2.2 we reported the uncertainty in the phase of our measurements, which is approximately 20° ($\sim \pi/10$). Hence, from Fig.3.6 b) one can see the effect of our experimental inaccuracy on the imaginary $\chi^{(2)}$ spectrum.

4

Water Structure and Orientation at Hydrophobic Surfaces

We study the structure and orientation of water molecules at water/alkane and water/polydimethylsiloxane interfaces with surface specific intensity VSFG and HD-VSFG spectroscopy. We find that the water molecules at D_2O/hexane, D_2O/heptane and D_2O/polydimethylsiloxane interfaces show an enhanced ordering and stronger hydrogen-bond interactions than the water molecules at an D_2O/air interface. With increasing temperature (up to 80°C) the water structure becomes significantly less ordered and the hydrogen bonds become weaker. We also find that the water molecules at the interface show a net orientation of their O–H groups pointing towards to the hydrophobic layer and that this orientation depends on the pH of the solution.

4.1 Introduction

The structure of water solvating hydrophobic solutes has been debated for almost 70 years. Frank and Evans were the first who investigated the properties of water surrounding hydrophobic molecular groups.[14] They observed that the dissolution of hydrophobes in water is associated with surprising thermodynamic changes like a decrease in entropy and an increase in heat capacity. To explain these observations they proposed the so-called 'iceberg' model for hydrophobic hydration, which implies that water hydrating a hydrophobic solute becomes highly ordered and acquires a structure that resembles that of ice. The iceberg model was later disputed by neutron scattering studies that showed that the water structure near hydrophobic solutes is characterized by an oxygen-oxygen correlation function $g_{OO}(R)$ that is much more similar to that of bulk water than to that of ice.[98,99] Theoretical work, in particular by Chandler and coworkers, did find that the hydrogen bond network of water surrounding small hydrophobic solute (<1 nm) remains intact, whereas for water surrounding large hydrophobic solutes the hydrogen-bonding network becomes disrupted.[16,100]

Recently, a Raman spectroscopy study of the vibrational spectrum of water molecules solvating small alcohols provided the first molecular-scale evidence for the enhanced ordering of water around small hydrophobic solutes.[101] Further

evidence for the different behaviour of water molecules in hydrophobic hydration shells was obtained from dynamic studies. Water molecules hydrating hydrophobic molecular groups were observed to show much slower orientational dynamics and hydrogen-bond dynamics than bulk water.[102–105] The slowing down of the dynamics of water molecules surrounding hydrophobic groups was reproduced by both classical and *ab initio* molecular dynamics simulations.[106,107]

Only few VSFG studies of water/oil systems have been reported, probably because it is not straightforward to produce a stable water/oil interface.[108–115] The Shen group has measured the structure of water at a fused quartz surface covered with an octadecyltrichlorosilane (OTS) monolayer.[108] The VSFG spectrum was observed to be red-shifted compared to that of a water/air interface, which was attributed to the adsorption of hydroxide ions to the interface of the hydrophobic tails of OTS and water. However, in another study of the same Quartz/OTS/water system, the changes in the VSFG spectra were attributed to the water molecules that are adsorbed near the polar head groups of the OTS molecules and the quartz surface.[109] In a very recent work by the group of Tyrode *et al.* it was shown that the VSFG response of water near an OTS coated silica surface strongly depends on the quality of the self-assembled OTS layer.[115] The signal increase of the hydrogen-bonded water molecules observed for some of the self-assembled OTS layers was assigned to water directly interacting with the fused silica substrate. Finally, the Richmond group[111–113] has investigated water/CCl_4 and water/alkane systems and concluded that the hydrogen bonds between water molecules at these interfaces are significantly weaker than at a water/air interface.

The orientation of water molecules at an oil interface has been investigated by probing the surface of oil droplets immersed in water with VSFG scattering spectroscopy.[110] In this study information on the orientation of the water molecules was obtained from the interference of the response of the C–H stretch vibrations of the oil with the low-frequency tail of the water hydroxyl vibrations. This interference was observed to be the same at the interface of a neutral oil droplet as at an interface covered with a negatively charged surfactant, which indicated that the water molecules are preferentially oriented with their hydroxyl groups pointing to the hydrophobic droplets. However, the main response of the water hydroxyl vibration could not be observed because of the strong infrared absorption of the water phase embedding the oil droplets.

Here we present intensity VSFG and HD-VSFG studies of the ordering and hydrogen-bonding of water molecules at water/hexane, water/heptane and water/polydimethylsiloxane interfaces. We find evidence that the structure of water at these interfaces is enhanced compared to the structure of water at a water/air interface. Further, we find that the water molecules have a preferred orientation with their dipole moments pointing to the hydrophobic layer.

4.2 Experimental

The experiments in this chapter were performed with intensity VSFG and HD-VSFG setups described in Chapter 3. We probe the OD stretch vibration of D_2O/air, D_2O/hexane, D_2O/heptane and D_2O/polydimethylsiloxane (PDMS) interfaces.

The formation of a stable layer of a hydrophobic material on a water surface depends on a subtle balance between short-range and long-range van der Waals forces. For short n-alkanes ($n \geq 4$) complete wetting of the surface is observed, whereas for alkanes with $5 \leq n \leq 8$ incomplete wetting state (partial wetting) occurs, implying a coexistence of an ultrathin layer and lenses on the surface. Alkanes with $n > 8$ form lenses without a thin film.[116]

In our experiments we form hexane and heptane layers on a water surface by adsorption of the alkanes from their saturated vapors. This method of sample preparation strongly reduces the possibility of contamination, because only volatile materials such as alkanes can evaporate and form a layer on water. It was shown with ellipsometry that this technique leads to hexane and heptane layers consisting of a thin film with droplets of micrometer dimensions.[116] The formation of alkane layers from saturated vapors was also demonstrated by X-ray reflectometry.[117] In these studies it was reported that the alkane layer thickness varies from 10 - 50 Å.

The water surface was enclosed in a Teflon coated aluminium cell with a CaF_2 window on top, ∼2 cm above the water surface (Fig. 4.1 a). The hexane or heptane (∼3 ml) is placed around the water reservoir, and not in contact with the water, after which the cell is sealed. The temperature of the cell can be varied from 0 till 80°C using a peltier element. The top CaF_2 window is heated to ∼5°C above the temperature of the sample, to prevent water condensation (for clarity not shown in the Fig. 4.1 a).

The PDMS layer was formed by depositing ∼200 μl PDMS directly on the water surface, which resulted in a thin PDMS layer (thickness ∼50 - 100 μm). PDMS is a hydrophobic polymer consisting of $(CH_3)_2SiO$ structural units and has a very low solubility in water, but due to its flexible backbone and weak intermolecular interactions between the methyl groups, it can wet the water surface.

We used D_2O (≥99.96%, Cambridge Isotope Laboratories), n-hexane (≥97.0%, Aldrich), n-heptane (≥99.0%, Aldrich), NaOH (50% in water, Aldrich), HCl (1 M in water, Aldrich) and polydimethylsiloxane (PDMS, M_r = 162.38, ≥98.5%, Aldrich) as received.

4.3 Results

4.3.1 Intensity VSFG

Figure 4.1 b – d shows intensity VSFG spectra in the frequency region of the OD stretch vibrations measured for D_2O/hexane, D_2O/heptane, and D_2O/PDMS. For comparison, we also show the VSFG spectrum of a D_2O/air interface

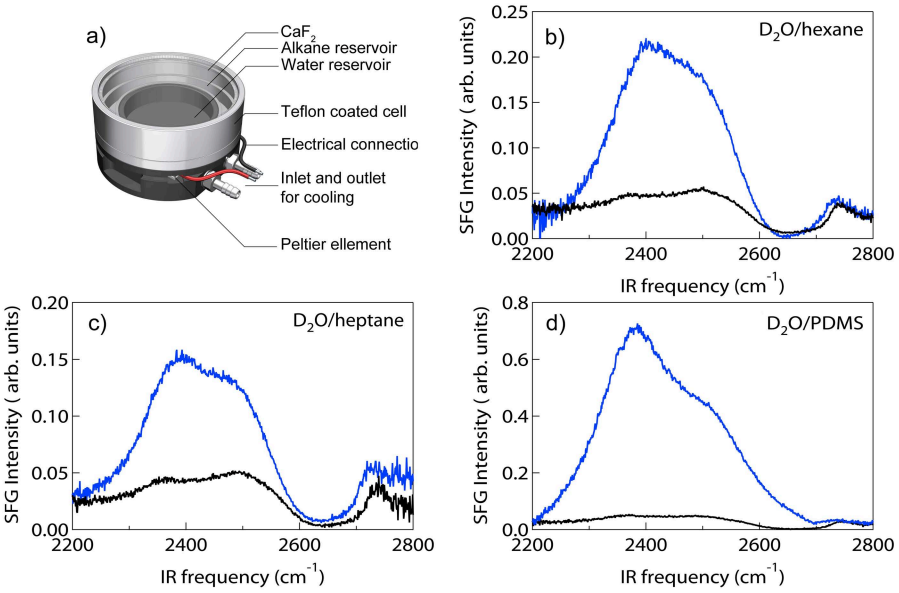

Figure 4.1. Schematic illustration of the closed cell used for the formation of a hexane or heptane layer on a water surface (a). Intensity VSFG spectra of a D_2O/hexane (b), D_2O/heptane (c), D_2O/polydimethylsiloxane (d). All spectra are compared with a D_2O/air spectrum (black line).

(Fig. 4.1 b – d, black line). All spectra have been recorded with a polarization combination S-SFG, S-VIS, P-IR. With this specific light polarization combination, water transition dipoles perpendicular to the surface are probed.

Figure 4.1 b – d show that the VSFG spectra of the D_2O/hydrophobe interfaces have much higher intensities than the D_2O/air interface. The VSFG intensity is proportional to the net ordering of the probed molecular vibrations. Hence, the strong increase in VSFG intensity indicates that there are more water molecules with a preferred orientation at D_2O/hydrophobe interfaces than at the D_2O/air interface. This indicates that water molecules at hydrophobic interfaces are less randomly oriented than at water/air interface. This increase in VSFG intensity cannot be caused by changes in Fresnel factors. It has been shown that the dispersion of bulk water only leads to enhancement of the local infrared electric field at frequencies well above the hydrogen-bonded region of the infrared spectrum.[118]

It is also seen in Figure 4.1 b – d that for the D_2O/hydrophobe interfaces the low-frequency peak (OD(I) $\sim$2370 cm^{-1}) is stronger than the high-frequency peak (OD(II) $\sim$2500 cm^{-1}), whereas for the D_2O/air interface the two peaks are of nearly equal intensity. In a recent study these two peaks have been explained from a Fermi resonance of the symmetric OD stretch vibration and the overtone of the bending mode.[54] The coupling of the OD stretch and the

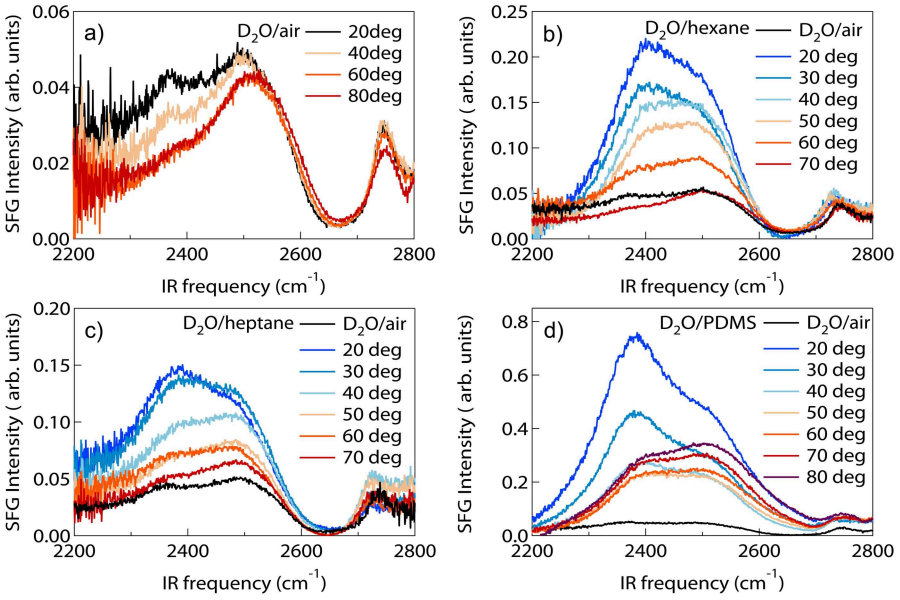

Figure 4.2. Intensity VSFG spectra of D_2O/air (a), D_2O/hexane (b), D_2O/heptane (c), D_2O/polydimethylsiloxane (d) at different temperatures (see inset). All spectra are compared with a D_2O/air spectrum (black line).

overtone of the bending vibration would lead to a so-called Evans window (region of lower intensity) within the broad band of the symmetric OD stretch vibration, thus giving the appearance of a double-peak structure. The relative intensities of the two peaks around the Evans window are dependent on the average H-bond strength of the water molecules at the interface. In case the hydrogen bonding is enhanced, the low-frequency peak becomes stronger than the high-frequency peak. Hence, the stronger low-frequency peak observed for the D_2O/hydrophobe interfaces indicates that the hydrogen bonds between the water molecules are stronger at these interfaces than at the D_2O/air interface. The free OD peak at $\sim$2745 cm^{-1} is not strongly affected by the presence of a hydrophobic layer. The peak is slightly red-shifted by $\sim$20 cm^{-1} and somewhat broadened, probably as a result of the van der Waals interactions between the water molecules and the molecules in the hydrophobic layer.

Figure 4.2 presents intensity VSFG spectra at different temperatures, up to a temperature of 80°C. For the D_2O/air interface the VSFG spectrum does not change dramatically in amplitude. An increase in temperature primarily leads to a decrease of the intensity of the low-frequency part of the hydrogen-bonded spectrum, meaning that the hydrogen bonds between the water molecules become weaker (Fig.4.2 a). For the water/hydrophobe interfaces the intensity of the VSFG spectrum decreases at all frequencies in the hydrogen-bonded region of the spectrum. The overall decrease in VSFG intensity is accompanied

by a relative increase of the high-frequency part of the hydrogen-bonded region of the VSFG spectrum relative to the low-frequency part of this spectrum. This change in spectral shape reflects a decrease of the average hydrogen-bond strength between the water molecules.

For the D_2O/hexane and D_2O/heptane interfaces the decrease in VSFG intensity is much stronger than for the D_2O/PDMS interface. This difference can be explained from the lower boiling point of the alkanes and the resulting evaporation of the alkane layer. At 70°C, the VSFG spectrum of the D_2O/hexane interface has become similar to that of the D_2O/air interface at the same temperature, because this temperature exceeds the boiling point of the hexane (68°C). For the D_2O/PDMS system the decrease in VSFG observed is not due to evaporation (boiling point of PDMS is >100 °C). For this system the decrease in VSFG intensity with temperature can be explained from the decrease in structuring effect of the hydrophobic molecules on the nearby water layers. For the D_2O/hexane and D_2O/heptane interfaces the decrease in VSFG intensity with temperature results both from a decreased order of the water layer and from (partial) evaporation of the hydrophobic layer.

4.3.2 Heterodyne-Detected VSFG

Intensity VSFG experiments show that water molecules are much more strongly ordered at the interface with a hydrophobic liquid than at the interface with air. However, from these measurements it is not clear how the water molecules are oriented at the interface.

In Figure 4.3 the real and imaginary part of $\chi^{(2)}$ ($\mathrm{Re}\chi^{(2)}$ and $\mathrm{Im}\chi^{(2)}$) are presented for D_2O/air and for three water/hydrophobic liquid interfaces. The sign of the $\mathrm{Im}\chi^{(2)}$ depends on the orientation of the vibrational transition dipole with respect to the surface normal, meaning that a positive $\mathrm{Im}\chi^{(2)}$ is associated with H_2O/D_2O molecules that have a net orientation of their hydrogen/deuterium atoms towards the other phase, e.g. pointing away from the bulk of the water phase.[119] The positive band at 2745 cm^{-1} observed for the D_2O/air interface has thus been assigned to dangling OD groups pointing into air, and the negative part around 2500 cm^{-1} to hydrogen-bonded D_2O molecules with a net orientation of their OD groups towards the bulk liquid. The $\mathrm{Im}\chi^{(2)}$ spectrum also shows a weak positive band between 2200 and ∼2400 cm^{-1}. Pieniazek *et al.*[59] explained this positive band from the competition of the low-frequency contribution of four-hydrogen-bonded molecules with their O–H groups pointing to the interface. Ishiyama and Morita[58,120] presented a different explanation for the observation of a positive $\mathrm{Im}\chi^{(2)}$ at low frequencies. According to this explanation the low-frequency vibration of a strongly hydrogen-bonded water molecule induces an oscillatory dipole moment in its hydrogen-bonded partner with a dipole orientation perpendicular to the surface. Hence, in this explanation the low-frequency part of $\mathrm{Im}\chi^{(2)}$ is not assigned to single strongly hydrogen-bonded water molecules but rather to an anisotropic polarization coupling between different water molecules. Recently, the Tahara group showed that there is no significant positive signal in the low-frequency region of the VSFG spectrum

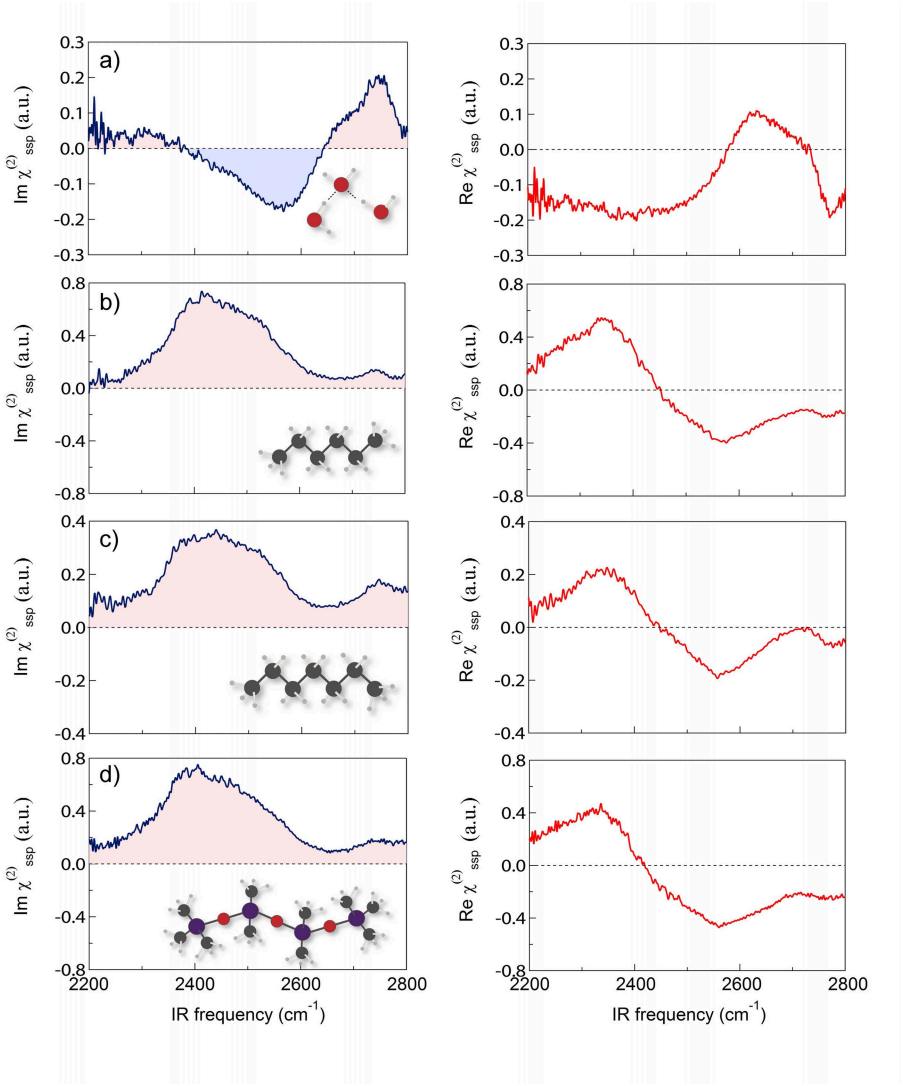

Figure 4.3. Imaginary $\chi^{(2)}$ (blue) and real $\chi^{(2)}$ (red) parts of (a) D_2O/air, (b) D_2O/hexane, (c) D_2O/heptane, (d) D_2O/polydimethysiloxane. The spectra are measured with heterodyne-detected VSFG spectroscopy with an s-SFG, s-VIS, and p-IR polarization combination.

of the OH stretch vibrations.[60] In this study it is also shown that previous reports of such a positive signal may well be due to an error in the phase of the experimentally determined Im$\chi^{(2)}$. Recent calculations also did not find evidence for the presence of a positive feature in the Im$\chi^{(2)}$ spectra at frequencies <3200 cm^{-1}.[121]

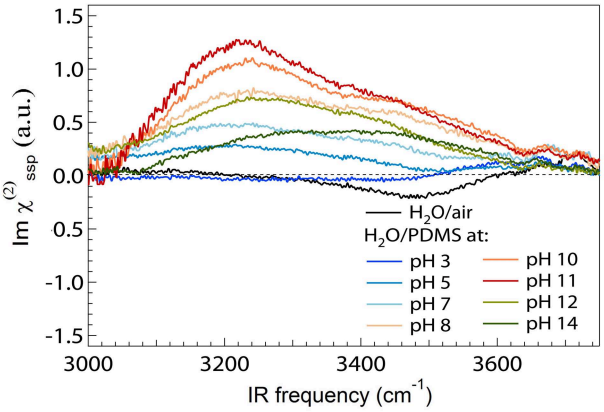

Figure 4.4. Imaginary $\chi^{(2)}$ part of H_2O/polydimethysiloxane interface at different pH values (indicated in the legend).

In Figure 4.3 we show that the Re$\chi^{(2)}$ and Im$\chi^{(2)}$ spectra of the hydrophobe/water interfaces strongly differ from the corresponding spectra of the D_2O/air interface. For all hydrophobic interfaces Im$\chi^{(2)}$ is positive throughout the hydrogen-bonded band, indicating that the hydrogen-bonded O–D groups show a quite strong net orientation towards the hydrophobic phase. In addition, at low OD frequencies, there can also be a contribution from the anisotropic polarization effect that was proposed for the water/air interface.[58]

Figure 4.4 presents Im$\chi^{(2)}$ spectra of H_2O/PDMS at different pH values (ranging from pH 3 to pH 14). The pH was increased by adding NaOH and decreased by adding HCl to the water phase. The results clearly show that changing the pH strongly affects the magnitude of Im$\chi^{(2)}$. With increasing pH, Im$\chi^{(2)}$ increases (becomes more positive), reaching a maximum value at ∼pH 11. This finding shows that at higher pH the water molecules become even more strongly oriented with their O–H groups pointing towards the oil phase than at neutral pH. Decreasing the pH below pH 7 leads to a decrease of Im$\chi^{(2)}$, meaning that water molecules become less oriented. At the lowest studied pH value of 3 the Im$\chi^{(2)}$ spectrum becomes even slightly negative over a large frequency of 3000 - 3500 cm^{-1}, indicating a net orientation of the water molecules with their O–H groups away from the oil phase.

4.4 Discussion

We find that water shows an enhanced ordering and stronger hydrogen bonding next to a hydrophobic interface at room temperature. This finding is quite different from the results of previous studies of the intensity VSFG spectrum of water/CCl_4 and water/alkane interface.[111–113, 122] In these studies it was found that at room temperature the hydrogen bonding between adjacent water

molecules is weaker than at an water/air interface. This difference is probably related to differences in the experimental parameters. The previous work was performed with high-energy (2 mJ at 2.5 μm to 1 mJ at 4 μm) nanosecond narrow-bandwidth IR beams,[111] whereas we use low-energy ($\sim$10 μJ) femtosecond broadband IR pulses. Our observation of enhanced order and increased hydrogen bonding of water at hydrophobic interfaces agrees with the results of VSFG scattering studies of oil droplets dispersed in water[110] and of a Raman spectroscopic investigation of the response of water molecules hydrating hydrophobic molecular groups in bulk alcohol/water mixtures.[101] Molecular dynamics simulations of water/heptane interface and water/decane interfaces also show the presence of an enhanced ordering of the water molecules at the interface at room temperature.[110,123]

We observe that the enhanced ordering of water at room temperature completely vanishes at elevated temperatures. This temperature dependence also agrees very well with the results of the recent Raman spectroscopic study of hydrophobic molecular groups in bulk alcohol/water mixtures.[101] The observation hydrophobic hydration effects decrease with increasing temperature agrees with thermodynamic observations and with studies of the dynamics of water hydrating hydrophobic solutes. In femtosecond infrared and NMR spectroscopic studies it was found that the reorientation of water molecules in the hydration shells of hydrophobic solutes is strongly slowed down compared to bulk water at room temperature, but speeds up when the temperature is increased.[103–105]

An interesting observation is that the temperature dependence of the intensity of the VSFG spectrum differs from the temperature dependence of the shape of the spectrum (Fig. 4.2). Up to $\sim$40°C the temperature increase leads to a decrease in intensity, while the shape of the spectrum remains rather similar to that at room temperature. At temperatures >40°C the spectrum shows a clear blue-shift. This type of behavior is especially clear for the D_2O/PDMS interface (Fig.4.2 d) for which the hydrophobic layer will not evaporate when the temperature is increased (in contrast to hexane and heptane that will (partly) evaporate). These findings indicate that the enhanced order of water surrounding hydrophobic molecular groups is even more strongly dependent on temperature than the strength of the average hydrogen-bond interaction. It thus appears that a minor change in temperature already suffices to change the ordering and net orientation of the water molecules induced by the hydrophobic surface.

The molecular-scale origin of the orientation of water molecules at an interface with alkane molecules has been a subject of intense debate. It has been proposed that this orientation arises from the presence of excess hydroxide ions at the water/oil interface.[108] As a result, the water/oil interface would possess a net negative charge, thereby inducing a preferred orientation of the O–H groups of water molecules in the adjacent layers towards the oil phase. The presence of excess hydroxide ions at the water/oil interface has also been proposed to be the origin of the observed negative ζ potential of oil droplets in water.[124] However, molecular dynamics simulations showed that the orientation of water molecules at water/alkane interfaces can also result from a purely structural effect, i.e. without invoking the presence of hydroxide ions.[110,123] In these simulations it

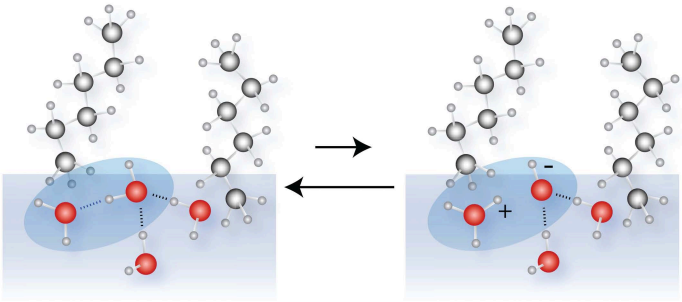

Figure 4.5. Schematic illustration of the formation of a water/oil interface with the water O–H groups showing a net orientation to the hydrophobic layer.

was shown that there exists an imbalance in donating and accepting hydrogen bonds close to the interface, leading to a net orientation of the water dipole moments and O–H groups towards the hydrophobic phase. The imbalance in donating and accepting hydrogen bonds also gives rise to a local region of excess negative charge in the water phase at ∼0.5 nm from the Gibbs dividing surface.

It should be noted that the two explanations for the net orientation of water molecules at the interface of water and alkanes are not mutually exclusive and could in fact represent the same physical effect. The imbalance in donating and accepting hydrogen bonds resulting from the truncation of the hydrogen-bond network will be accompanied by changes in the electron density. In a valence bond picture this would mean that the hydrogen-bonded $H_2O\cdots HOH$ pairs would have a stronger admixture of $H_2O^+H\cdots OH^-$ character, which would imply that the concentration of both hydronium (H_3O^+) and hydroxide (OH^-) would be increased near a water/alkane interface. In *ab initio* MD simulations of the water/air interface it was shown that the solvation structure of hydroxide ions is more flexible than that of hydronium and that the hydroxide ion becomes partially desolvated as it approaches the interface.[125] Moreover, the hydrogen bond donated by a hydroxide ion is weak, which implies that for a weakly hydrogen-bonded (dangling) OH group at the interface the energy cost of acquiring OH^- character is smaller than for a strongly hydrogen-bonded OH group in the bulk. It is thus conceivable that the hydroxide character is more pronounced on the water OH groups that are in direct contact with the alkane molecules than on water OH groups that are deeper down in the water layer, meaning that an enhancement of the $H_2O^+H\cdots OH^-$ valence bond character would have a preferential orientation with the OH^- close to the alkane phase. This $H_2O^+H\cdots OH^-$ valence-bond character is further stabilized in case the OH group acquiring the OH^- character accepts two hydrogen bonds donated by H_2O molecule that are one layer deeper, as the formation of these hydrogen bonds is accompanied by a transfer of a small amount of negative charge from the hydrogen-bond accepting OH^- group to the two hydrogen-bond donating OH groups.[110] The configuration showing enhanced $H_2O^+H\cdots OH^-$ valence-bond character is schematically depicted in Fig. 4.5. An increase in

$H_2O^+H\cdots OH^-$ valence-bond character at the interface will create a local electric field that orients nearby water OH groups towards the alkane phase.

This explanation is consistent with the observation that the orientation of water is further enhanced when the pH is increased, as shown in Figure 4.4. The higher bulk hydroxide concentration will stimulate the fraction of water molecules at the interface showing $H_2O^+H\cdots OH^-$ valence bond character, thereby increasing the local electric field that orients water OH groups towards the alkane phase. The surface concentration of $H_2O^+H\cdots OH^-$ valence bond structures will be very small (<<mmolar) and the OH^- vibrations are thus not directly observable in the VSFG response. However, an increase in $H_2O^+H\cdots OH^-$ valence-bond character at the interface will create a local electric field that orients nearby water OH groups towards the alkane phase. As a result, $\mathrm{Im}\chi^{(2)}$ acquires a positive sign at all frequencies, as is observed in Fig. 4.3.

Further *ab initio* molecular dynamics simulations will be needed to elucidate the potentially cooperative effect of local structure and charge redistribution on the hydrogen-bond structure and orientation of water molecules at the water/oil interface. These simulations should specifically address water/oil interfaces, as we observe the properties of water molecules at these interfaces to be substantially different from that of water molecules at the water/air interface.

4.5 Conclusions

We studied the structure and net orientation of water molecules at the water/hexane, water/heptane, and water/polydimethylsiloxane interfaces. With intensity VSFG spectroscopy we observe that the water hydrogen-bond structure at these interfaces is enhanced in comparison to the hydrogen-bond structure at the water/air interface. We also observe that the VSFG spectrum is red-shifted compared to that of a water/air interface, which points at a strengthening of the hydrogen bonds between the water molecules. With increasing temperature the VSFG intensity strongly decreases and the VSFG spectrum shows a significant blue-shift, indicating that the ordering of the water decreases, and that the hydrogen bonds become weaker. By interfering the VSFG light with the light of a local oscillator we determine the absolute phase of the VSFG light generated by the water/alkane and water/polydimethylsiloxane interfaces. Thereby we determine the orientation of the water molecules at all frequencies of the O–H stretch absorption band. For all three studied interfaces the water molecules show a net orientation with their O–H groups pointing towards the hydrophobic phase. This net orientation is observed at all frequencies of the O–H stretch vibrational absorption spectrum. This behavior strongly differs from that of water molecules at the water/air interface, where the orientation depends on the O–H stretch frequency and where most hydrogen-bonded water molecules have their O–H groups pointing towards the water phase.

5

The Interplay of Electrostatic Interactions and Hydrophobic Hydration at the Surface of Tetra-n-Alkylammonium Bromide Solutions

We use intensity VSFG and HD-VSFG to study the structure of water at the surface of aqueous tetra-n-alkylammonium bromide (TAABr) solutions. We compare the water structure for four different n-alkyl chains (n = 1, 2, 3, 4). For solutions of tetra-n-alkylammonium bromides with short n-alkyl chains (n = 1, 2), we observe the structure of the surface water to be similar to the structure observed for simple inorganic salt solutions. For these solutions, the presence of Br^- at the interface is observed to lead to a small decrease in the average strength of the hydrogen bonds. For solutions of tetra-n-alkylammonium bromides with long n-alkyl chains (n = 3, 4), we observe a strong ordering of the water molecules at the solution surface. The water molecules show a net orientation of their O–H group towards the bulk, which can be explained from the high surface propensity of positively charged tetra-n-alkylammonium ions with long alkyl chains (n = 3, 4). With increasing concentration of TAABr this ordering decreases and at very high concentrations (> 2 M) the orientation of the water molecules reverses. This latter finding can be explained from the formation of aggregated clusters of TAA^+ cations and Br^- anions near the solution surface.

5.1 Introduction

Hydrophobic interactions play an essential role in several biological phenomena, such as protein folding and the formation of biological membranes.[9] This interaction is governed by the thermodynamics of the hydration of hydrophobic molecular groups. These thermodynamics show a remarkable dependence on the size of the hydrophobic solute. In particular, for small solutes with a typi-

cal size <1 nm, the entropy of hydration is negative, which indicates that small solutes are well accommodated in water, leading to an enhancement of the water structure and hydrogen-bonding network. In contrast, large solutes disrupt the water structure, leading to the formation of a vapour-like interface. An elegant theoretical description of this length-scale dependence was developed by Lum, Chandler and Weeks.[16,126]

Tetra-n-alkylammonium halides (TAAX, X = Br^-, Cl^- and etc.) are widely used as model systems to study hydrophobic phenomena, because the tetra-alkyl-ammonimum (TAA^+) ion is well soluble in water and its hydrophobicity can be tuned by varying the length of the alkyl chain. TAA^+ ions display both electrostatic and hydrophobic interactions. A number of studies have been performed on TAA salt solutions to investigate hydrophobic hydration and in particular the cross-over behavior of small and large hydrophobic solutes. Early thermodynamic and transport studies have pointed indirectly to an increased ordering of water around large TAA^+ cations such as tetra-propyl-ammonium (TPA) and tetra-butyl-ammonium (TBA).[14,127] In contrast to that, a later neutron diffraction study of TAABr solutions found that the hydrogen-bond structure of water around TAA^+ cations does not differ from that of bulk water, meaning that the structural enhancement of water commonly associated with hydrophobic hydration was not observed.[98,99] Recent small-angle X-ray scattering experiments did find the water structure around the hydrophobic TAA^+ ions to be enhanced compared to bulk water. This enhancement was observed to be more pronounced for TPABr and TBABr solutions than for tetra-methyl-ammonium bromide (TMABr) and tetra-ethyl-ammonium bromide (TEABr) solutions.[128]

With most spectroscopic techniques such as infrared or Raman, it is challenging to measure the effect of hydrophobic moieties on the structure of water, because the contribution of the hydration shells to the signal is usually much smaller than the bulk water signal. Here we use the highly surface-specific techniques of VSFG and HD-VSFG spectroscopy to study the effects of TAA^+ and Br^- ions on the hydrogen-bond structure of water.

5.2 Experimental

We studied aqueous TAABr solutions with different alkly groups and at a range of concentrations. In the preparation of the samples we used water from a Millipore Nanopure system (18.2 MΩ cm). TMABr (≥98 %), TEABr (≥99 %), TPABr (≥98 %), TBABr (≥99 %), and TPACl (≥98 %) were purchased from Sigma Aldrich and used without further purification. We measured linear infrared spectra of all samples with an FTIR spectrometer (Bruker Vertex 80v). The surface tension of the solutions was measured with a Langmuir tensiometer (Kibron DeltaPi).

5.3 Results

5.3.1 Intensity VSFG

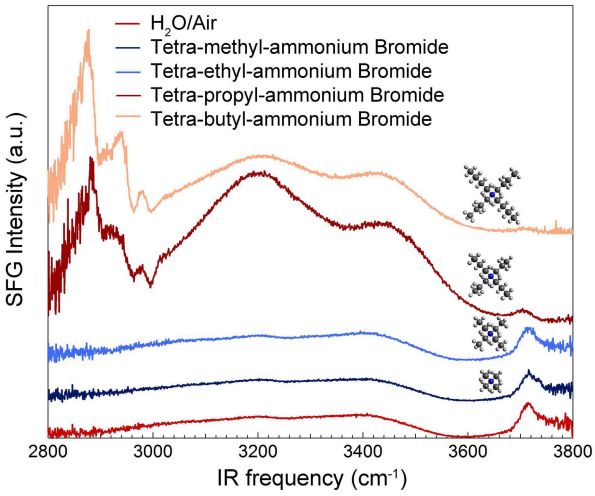

Figure 5.1. Intensity VSFG spectra of pure water and 0.1 M tetra-n-alkylammonium bromide salt solutions.

Figure 5.1 shows intensity VSFG spectra of neat water and 0.1 M tetra-n-alkylammonium bromide solutions. The VSFG spectra of 0.1 M concentration tetra-methyl-ammonium bromide and tetra-ethyl-ammonium bromide solutions are practically indistinguishable from the pure water spectrum. In contrast, the VSFG spectra of tetra-propyl-ammonium bromide and tetra-butyl-ammonium bromide are quite different. The VSFG spectra of TPABr and TBABr solutions show a clear response in the spectral region of the CH stretch vibrations (2800 - 3100 cm^{-1}) that is not observed for the TMABr and TEABr solutions and also show a much higher intensity than the VSFG spectrum of bulk water in the O–H vibrational region. These observations indicate that TAA^+ ions with long alkyl chains (n = 3, 4) have a much higher surface propensity than TAA^+ ions with short alkyl chains (n = 1, 2).

In Figure 5.2 we present VSFG spectra of solutions of TEABr and TPABr at different concentrations. For TEABr (Figure 5.2 a) the VSFG intensity shows a gradual increase with concentration, and there is no significant change in the shape of the spectrum, except for a small blue-shift at the highest measured concentration of 8 M. For TPABr the VSFG intensity strongly increases with concentration. At a bulk concentration of ∼0.001 M of TPABr, the VSFG intensity is already substantially higher than that of pure water. The VSFG intensity reaches a maximum value at a low bulk concentration of ∼0.01 M: a further increase of the concentration leads to a decrease of the VSFG signal. Besides the clear intensity changes, the addition of TPABr is observed to lead

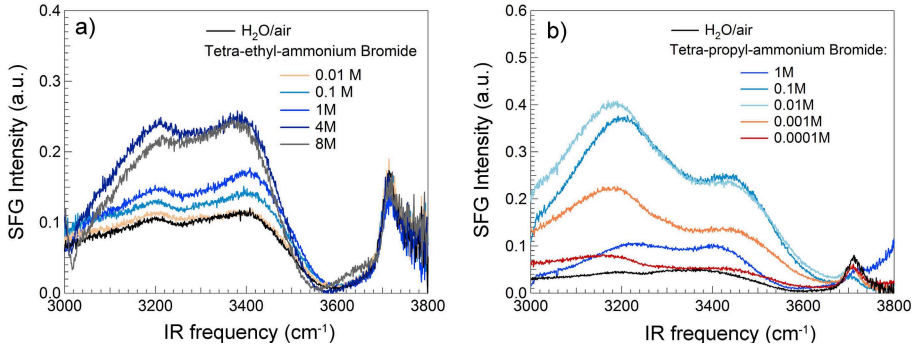

FIGURE 5.2. Intensity VSFG spectra of (a) TEABr and (b) TPABr salts at different concentrations.

to a red-shift of the broad hydrogen bonded water band. Up to concentrations of 1 M, the low-frequency peak (∼3200 cm^{-1}) is much stronger than the high-frequency peak (∼3400 cm^{-1}), which is quite different from the VSFG signal of the surface of pure water, for which the two peaks are of approximately equal intensity.

In Figure 5.3 we present VSFG spectra of solutions of TBABr at different concentrations. In Figure 5.3 a) we probe the C–H stretch vibrational region and here we observe a gradual increase of the bands at 2865 cm^{-1}, 2940 cm^{-1} and 2980 cm^{-1}. We assign these bands to the symmetric C–H stretch vibration, the Fermi resonance and the asymmetric C–H stretch vibration of the CH_3 groups of the butyl chains, respectively. In Figure 5.3 b) we probe the O–H stretch vibrational region of the interfacial water molecules. The VSFG spectra of TBABr solutions show a very similar shape and concentration dependence as the VSFG spectra of TPABr solutions in the same frequency region (Figure 5.2 b). For TBABr the VSFG signal reaches a maximum intensity at an even lower concentration (∼0.001 M for TBABr and ∼0.01 M for TPABr), which indicates that TBABr has an even higher surface propensity than TPABr. For concentrations >0.001 M the VSFG signal of TBABr solutions starts to decrease and at ∼1 M the VSFG spectrum in the O–H region looks quite similar to that of pure water. Finally, at higher concentrations (>1 M) the spectrum shows a slight increase again and the high-frequency peak of the O–H stretch spectrum becomes larger than the low-frequency peak.

The concentration range of the VSFG spectra of TPABr and TBABr solutions in the O–H stretch vibrational region can thus be divided into three regions: a low concentration range (0 – 0.01 M), in which the VSFG signal strongly increases and red-shifts, indicating that the water molecules at the surface become much more oriented and more strongly hydrogen bonded; a medium concentration range (0.01 – 1 M), where the VSFG signal decreases and becomes less red-shifted, which means that the water molecules become less oriented and less strongly hydrogen bonded; and a high concentration range (1 –

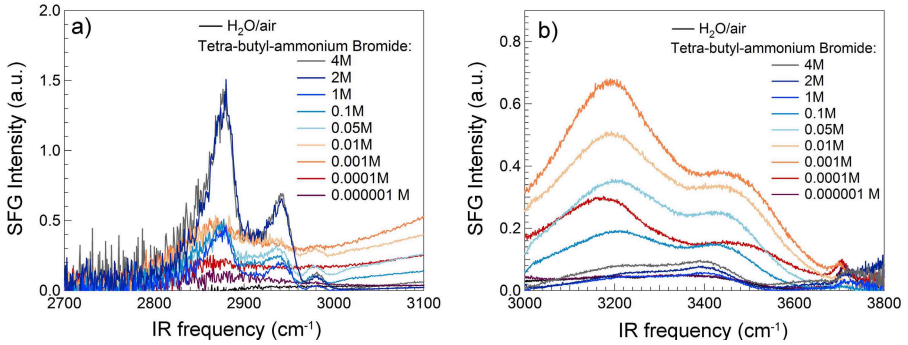

Figure 5.3. Intensity VSFG spectra of solutions at different concentrations of TBABr in H_2O. (a) Frequency region of the C–H stretch vibrations, and (b) frequency region of the O–H stretch vibrations.

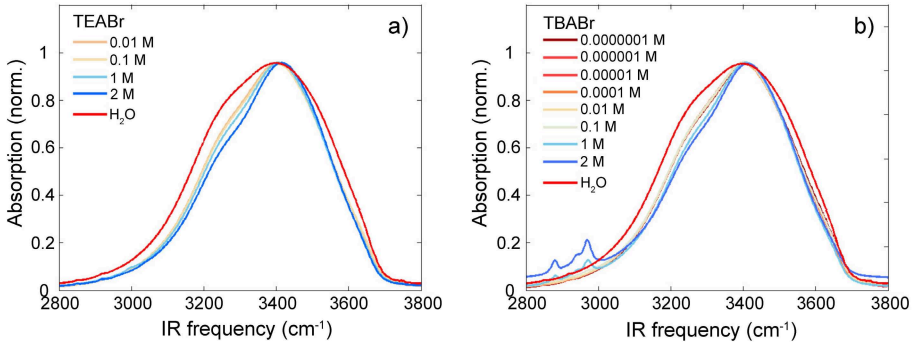

Figure 5.4. Linear IR spectra of (a) TEABr and (b) TBABr at different concentrations.

4 M), where the VSFG signal again slightly increases and the spectral response gets blue-shifted, indicating that the probed water molecules are more weakly hydrogen bonded.

The red-shift of the VSFG spectrum of the O–H stretch vibrations is a quite interesting observation. Infrared absorption spectra of TBABr solutions that probe the response of the bulk water molecules do not show such a red-shift of the response of the O–H stretch vibrations (see Figure 5.4). In fact, the infrared absorption shows a blue-shift of the O–H stretch absorption band that gets more pronounced with increasing concentration. The blue shift can be explained from the fact that the hydrogen bonds between water molecules and bromide ions are weaker than water-water hydrogen bonds. As a result, the O–H stretch vibrations of water molecules hydrating the Br^- ions appear at higher frequencies (blue-shifted).[129] The Raman spectra of TMACl, TEACl and TPACl also show an enhancement of the high frequency water peak, which

is explained from the formation of hydrogen bonds to Cl^- ions that are weaker than the hydrogen bonds between water molecules.[130] Clearly, the red-shift of the O–H stretch VSFG response of low-concentration solutions of TPABr and TBABr solutions is quite anomalous and likely a highly surface-specific phenomenon.

5.3.2 HETERODYNE-DETECTED VSFG

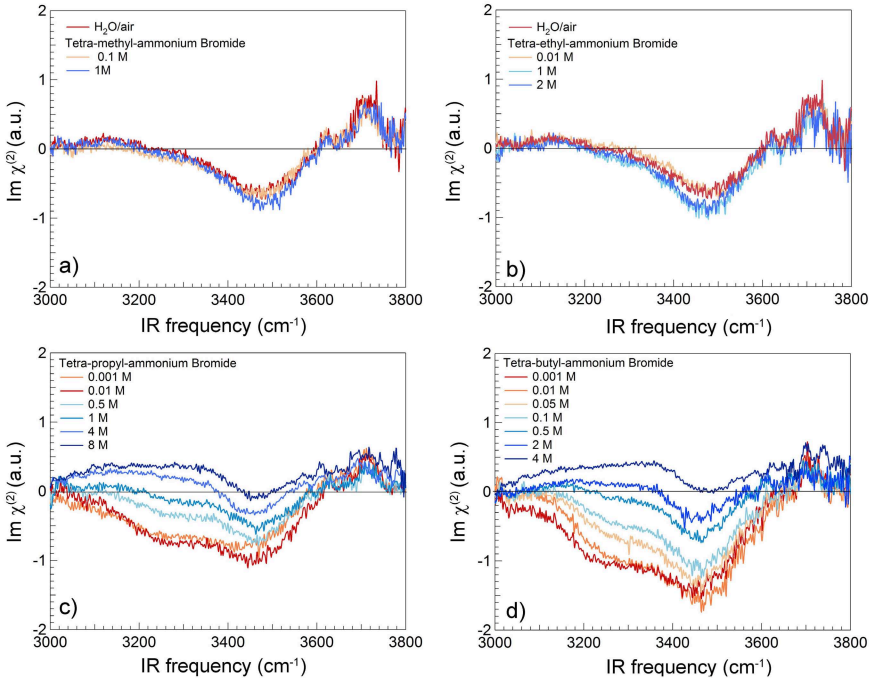

FIGURE 5.5. Imaginary $\chi^{(2)}$ spectra of (a) TMABr, (b) TEABr, (c) TPABr, and (d) TBABr at different concentrations (see legend).

To investigate the effect of TAABr salts on the orientation and hydrogen bonding of surface water molecules in more detail, we performed HD-VSFG experiments. In Figure 5.5 we present the Im $\chi^{(2)}$ for the surfaces of pure water and tetra-n-alkylammonium bromide (n = 1, 2, 3, 4) solutions at different concentrations. The Im $\chi^{(2)}$ spectra of TMABr and TEABr differ only slightly from the Im $\chi^{(2)}$ spectrum of the pure water surface (Figure 5.5 a and b), in agreement with the intensity VSFG data. In contrast, the Im $\chi^{(2)}$ spectra of TPABr and TBABr are strongly concentration dependant. At low concentrations of TPABr or TBABr (~0.001 M), the Im $\chi^{(2)}$ spectra are negative throughout the hydrogen-bonded region, indicating that the water OH groups show a net orientation towards the bulk. Interestingly, the amplitude of this negative band decreases with increasing concentration. At high concentrations

of TPABr (∼1 M) and TBABr (∼0.5 - 1 M) solutions the Im $\chi^{(2)}$ spectra become similar to the Im $\chi^{(2)}$ spectrum of the pure water surface. At extremely high concentrations of TPABr (∼8 M) and TBABr (∼4 M) the Im $\chi^{(2)}$ spectra acquire an overall positive sign, indicating that the O–H groups of the water molecules show a net orientation away from the water bulk. For solutions of tetra-propyl-ammonium chloride (TPACl) we observe a very similar concentration dependence of the Im $\chi^{(2)}$ spectrum of the water band (Figure 5.6).

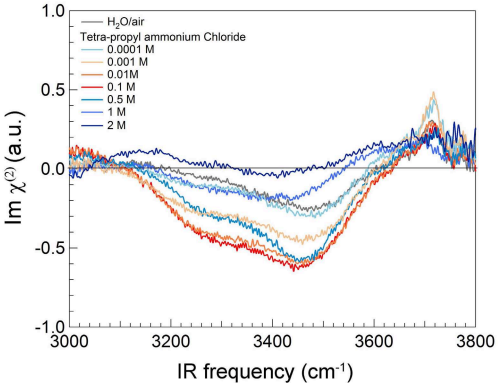

Figure 5.6. Imaginary $\chi^{(2)}$ spectra of TPACl at different concentrations.

5.4 Discussion

The intensity and heterodyne-detected VSFG spectra of short-chain (n = 1, 2) TAABr salts are completely different from those of long-chain (n = 3, 4) TAABr salts. The VSFG spectra of solutions of short chain TAA^+ cations are quite similar to the VSFG spectrum of the surface of pure water, indicating a low surface propensity of these ions. Apparently, short chain TAA^+ cations are well solvated in bulk liquid water, which implies that the electrostatic interactions of the TAA^+ cations dominate over the hydrophobic interactions. In contrast, long chain TAA^+ cations are expelled from the bulk liquid leading to a high surface concentration. For long chain TAA^+ cations hydrophobic interactions between water and the n-alkyl chains are hence more relevant than electrostatic interactions. This result agrees with surface tension measurements.[131] In Figure 5.7 a we present the surface tension of solutions of TEABr and TBABr as a function of concentration. It is observed that the surface tension of TEABr remains constant (∼72 mN/m) over the whole studied concentration range of 0 - 4 M, whereas the surface tension of TBABr solutions strongly decreases with increasing concentration, reaching a low value of ∼45 mN/m for concentrations >1 M. In Figure 5.7 b) we compare the concentration dependence of the surface tension of TBABr with that of the intensity of the VSFG signal at 3200 cm^{-1}. It is seen that at low concentrations the VSFG intensity strongly increases with

concentration, while the surface tension is negligibly affected. At concentrations >0.001 M both the VSFG intensity and the surface tension decrease, indicating a similar origin, i.e. the presence of a high density of TBA^+ and Br^- ions in the interfacial region. Figure 5.7 b) thus clearly shows that the surface tension is not representing the propensity of particular ions in the top molecular layers of the solution, but rather the interfacial salt concentration probed over a much larger depth.

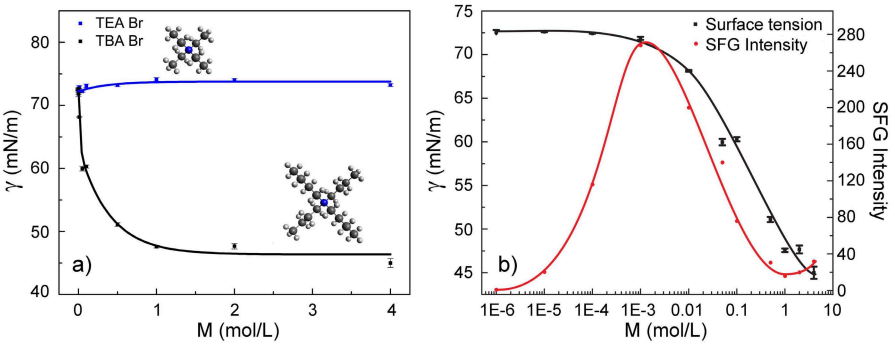

FIGURE 5.7. (a) Surface tension as a function of concentration for TEABr and TBABr solutions; (b) Surface tension and VSFG intensity at 3200 cm^{-1} as a function of concentration for TBABr solutions. The lines are guides to the eye.

For solutions of short-chain TAA^+ ions, the increase of the concentration leads to a small blue-shift of the hydrogen-bonded water band. This blue-shift indicates the presence of relatively weak hydrogen bonds and can be explained from the increased contribution of water O–H groups forming hydrogen bonds to Br^- ions. This result agrees with the work by Allen and coworkers in which it was shown that the addition of halide salts to water leads to a blue-shift of the intensity VSFG spectrum.[132,133] For TPABr and TBABr solutions the VSFG spectrum shows a strong red-shift at low concentrations, which obviously cannot be caused by hydrogen bonding to Br^- ions. In previous studies we found that the hydrogen bonds between water molecules become stronger at the interface of water and hydrophobic liquids like hexane, heptane and polydimethylsiloxane.[134] A similar result was found in advanced spontaneous Raman scattering studies of solutions of alcohols. In these studies it was shown that the hydrogen-bond structure of water hydrating the alkyl chains of the alcohols is enhanced in comparison to the hydrogen-bond structure of bulk liquid water.[101] Hence, the observed red-shift of the intensity and VSFG spectrum of solutions of TPABr and TBABr can be explained from the hydration of the hydrophobic alkyl chains of these ions near the solution surface.

In addition to the red-shift, we observe an increase in intensity of the VSFG spectrum of TPABr and TBABr solutions in comparison to bulk liquid water. This intensity increase can be explained from the electric field that is created by

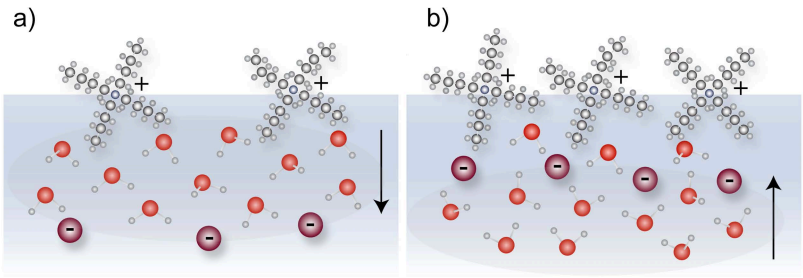

Figure 5.8. Schematic picture of the interfacial configuration of cations and anions at (a) low and (b) high concentrations of TPABr and TBABr.

the large concentration of hydrophobic cations at the surface and the Br^- ions that on average are located deeper down in the liquid. Br^- ions tend to have a somewhat higher concentration at the surface than in the bulk.[135–137] However, in comparison to TPA^+ and TBA^+ ions the surface propensity of Br^- is weak. The separation of the positive TPA^+ and TBA^+ ions and the negative Br^- ions leads to an electric field pointing away from the surface, thereby orienting the water O–H groups towards the bulk phase, thus explaining the large negative value of Im $\chi^{(2)}$ of the water O–H band for low-concentration solutions of TPABr and TBABr. For the VSFG signal of the C–H vibrations the electric field effect is far less pronounced. In Figure 5.3 a) it is seen that the VSFG intensity of the C–H vibrations increases only gradually with increasing concentration. This strong difference in concentration dependence of the C–H and the water O–H signal can be explained from the fact that the water molecules possess a dipole moment, and thus strongly orient in the electric field created by TPA^+ and TBA^+ ions at the surface and Br^- ions deeper down in the liquid. The TPA^+ and TBA^+ ions do not possess a dipole moment as the alkyl chains are symmetrically (tetrahedrally) arranged around the N atom. For TPACl solutions we observe a similar concentration dependence of the Im $\chi^{(2)}$ spectrum of the water band, showing that Cl^- ions behave very similar to Br^- ions.

When the concentration of TPABr and TBABr is increased, the amplitude of the negative band decreases. This decrease can be explained from the decrease in distance between the centers of positive and negative charge in the interfacial region. As a result, there are less water molecules confined in between the TAA^+ and Br^- ions, and the VSFG signal decreases. At very high TPABr and TBABr concentrations, the TAA^+ cations and Br^- ions will form aggregated clusters at the solution surface, with a somewhat higher concentration of Br^- ions deeper down in the solution. In Figure 5.8 we present a schematic picture of the interfacial configuration of the cations and anions at low and high concentrations of TPABr and TBABr. In the high-concentration regime there will be very few water molecules enclosed by the TAA^+ and Br^- ions, and the VSFG spectrum will become dominated by water molecules form-

ing hydrogen bonds to the Br^- ions of the aggregated cation-anion layer at the surface. For these water molecules the O–H will have a net orientation away from the bulk, explaining the positive sign of the Im $\chi^{(2)}$ spectra in the high concentration regime. In addition, the hydrogen bonds to the Br^- ions are somewhat weaker than the hydrogen bonds between water molecules, thus explaining the blue-shift of the intensity and heterodyne-detected VSFG spectra of highly concentrated solutions of TPABr and TBABr.

5.5 CONCLUSIONS

We studied the surface properties of solutions of tetra-n-alkylammonium bromide salts using intensity and heterodyne-detected VSFG spectroscopy. We observe that short-chain tetra-n-alkylammonium bromides (n = 1, 2) behave like simple inorganic salts. TMA^+ and TEA^+ ions show little surface propensity. As a result, the VSFG spectra of short-chain tetra-n-alkylammonium bromides (n = 1, 2) are similar to the VSFG spectrum of pure liquid water. A slight blue shift of the spectrum is observed that can be explained from the contribution of water molecules forming hydrogen bonds to the Br^- ions. For long-chain tetra-n-alkylammonium bromides (n = 3, 4) we observe a very different VSFG spectrum, due to the high surface propensity of the tetra-propyl-ammonium and tetra-butyl-ammonium cations. At low bulk concentrations, the VSFG spectra are dominated by hydrophobic hydration effects, leading to a red-shift of the response of hydrogen-bonded water molecules. In addition the amplitude of the VSFG spectrum is strongly enhanced due to the orienting electric field that is created by the separation of the center of positive charge associated with the positive TAA^+ ions at the surface and the center of negative charge associated with the Br^- ions deeper down in the solution. At high concentrations, the TAA^+ and Br^- ions form aggregated clusters at the solution surface and the VSFG spectrum is dominated by water molecules forming hydrogen bonds to the Br^- ions of these clusters.

6

Orientation of Polar Molecules near Charged α-Lactalbumin Protein Interfaces

We study the orientation of water, urea molecules and protein amide vibrations at aqueous α-lactalbumin and α-lactalbumin/urea interfaces using heterodyne-detected VSFG. We vary the net charge of the protein by changing the pH. We find that the orientation of the water and urea molecules closely follows the net charge of the protein at the surface of the solution. In contrast, the net orientation of the amide groups of the backbone of the protein is independent of pH. We discuss the implications of these results for the mechanism by which urea denatures proteins.

6.1 Introduction

Water plays a crucial role in the functioning and dynamics of proteins. Several recent experimental and theoretical studies indicate that water not only determines the conformation of proteins, but can also play an active role in their function.[138] For instance, water molecules can form essential parts of enzymatic pockets,[139,140] and the structuring of water layers adjacent to the ice-binding site of an antifreeze protein can provide the protein with a high affinity for nascent ice crystals.[141] Protein/water interfaces further play an important role in colloid research and the food industry. The macroscopic material properties of aqueous-protein mixtures can often be tuned by subtle changes in the composition, because these changes can induce interfacial rearrangements that in turn strongly affect the intermolecular interactions.[142] A detailed investigation of the structural and dynamical properties of water molecules at protein surfaces is therefore of great interest for both the understanding of biomolecular processes and for industrial applications.

Vibrational sum-frequency generation spectroscopy has been demonstrated to be a powerful tool to study the molecular orientation and conformation at protein/water interfaces.[143,144] Intensity VSFG studies showed that a change of the pH induces a strong change in the signal of the water molecules, and this

change can be explained from the pH-dependent net charge of the protein.[145,146] In an intensity VSFG study of aqueous protein solutions by the group of Paul Cremer, it was proposed that these changes can be well explained from a change of the orientation of the water molecules in response to the variation of the total charge on the protein as a function of pH.[147] Using heterodyne-detected VSFG it has been shown that charged lipid monolayers and organic molecules can orient interfacial water molecules.[95,148]

Urea is a small, highly polarizable molecule with similar properties as water, and it is widely used to denature proteins. The underlying mechanism of the denaturation is still under debate.[149–151] Denaturation can either occur through a direct or an indirect mechanism. In the direct mechanism, urea accumulates at the protein surface and replaces water molecules solvating the protein, meaning that urea directly binds to the backbone of the protein.[149,152,153] In the indirect mechanism the denaturation results from a urea-induced change in the water structure.[150,154] The effects of urea on the structure and dynamics of water are observed to be small, which points at a direct denaturation mechanism of urea.[155]

In a recent intensity VSFG study by the group of Paul Cremer evidence was found for an indirect denaturation mechanism of urea.[147] In this study it was shown that the orientation of urea molecules at the protein interface depends on the net charge of the protein and, moreover, that this orientation follows the orientation of the interfacial water molecules. This finding was interpreted as urea molecules being completely enclosed by the hydrogen-bond network of water thus closely following the orientation of the water molecules.[147] However, the net orientation of the dipolar amide groups of the protein may show a similar dependence on the protein charge state and thus on the pH as the urea and water molecules. Hence, a change in the orientation of the urea molecules could be induced by the flipping of the net orientation of the water molecules (pointing at an indirect denaturation mechanism) or by the flipping of the amide groups. In the latter case the urea molecules can be hydrogen bonded to the amide groups, which would point at a direct denaturation mechanism. A distinction between these two scenarios can be possibly made by probing not only the orientation of the urea and water molecules, but also the orientation of the amide groups of the protein.

Here we study the structure and orientation of water, urea and the amide groups of α-lactalbumin using heterodyne-detected VSFG. α-lactalbumin is a common protein that is present in the milk of almost all mammalian species used in industrial food products. The structure of α-lactalbumin is known and has been widely investigated.[156,157] The protein consists of 123 amino acids and its structure contains α-helical ($\sim$34%), β-sheet ($\sim$12%) and disordered ($\sim$50%) elements.[158,159] The molecular weight is 14 kDa and the isoelectric point (IEP) is $\sim$4.9.

6.2 EXPERIMENTAL

α-Lactalbumin (BioPure) was purchased from Davisco and was used without further purification. Urea (ACS reagent, ≥99.0 %) was purchased from Sigma Aldrich. D_2O (≥99.96 %) was purchased from Cambridge Isotope Laboratories. The HD-VSFG measurements were performed in ultrapure water or D_2O, and the pH/pD was adjusted using NaOH/NaOD (1 M in water, Aldrich) and HCl/DCl (50 % H_2O/D_2O, Aldrich).

6.3 RESULTS AND DISCUSSION

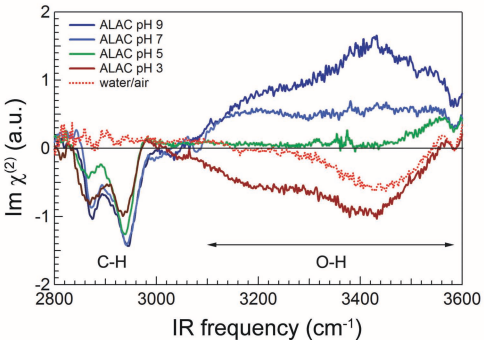

FIGURE 6.1. Imaginary $\chi^{(2)}$ spectra of aqueous α-lactalbumin at different pH values in the region of 2800 - 3600 cm^{-1}.

Figure 6.1 shows HD-VSFG spectra of water and aqueous α-lactalbumin at the air/water interface at different pH values, measured in ssp polarization (s-SFG, s-VIS, p-IR). The sign of the $Im\chi^{(2)}$ spectrum of the OH vibrations depends on the projection of its vibrational transition dipole moment on the surface normal. A negative $Im\chi^{(2)}$ corresponds to OH groups that on average point to the bulk of the liquid, while a positive $Im\chi^{(2)}$ corresponds to OH groups pointing away from the bulk. The $Im\chi^{(2)}$ spectrum of α-lactalbumin at the water/air interface strongly differs from that of pure water. In addition to the response of the water OH vibrations, this spectrum shows two negative bands at ∼2880 cm^{-1} and ∼2950 cm^{-1}. We assign the 2880 cm^{-1} band to the methyl symmetric stretching vibration (CH_3, SS) and the 2950 cm^{-1} band to the Fermi resonance (CH_3, FR) of this vibration and the overtone of the methyl bending vibration.[57] A much weaker positive band is observed at ∼2990 cm^{-1} which we assign to the methyl anti-symmetric stretching vibration (CH_3, AS).[160] The negative signs of the CH_3, SS and CH_3, FR bands, and the positive sign of CH_3, AS indicate that the associated methyl groups are oriented towards the air phase.[148,161] We attribute the CH stretch vibrations to the methyl groups of amino acid residues. An additional weak band is observed at 3060 cm^{-1}. This band can be assigned to aromatic CH stretch vibrations of the aromatic

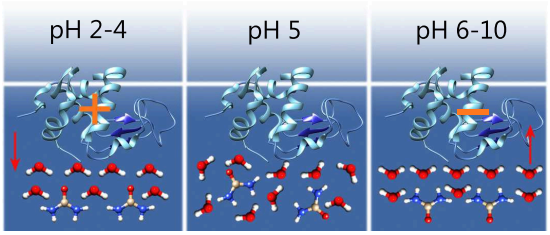

FIGURE 6.2. Schematic representation of α-lactalbumin and the water subphase for neutral, negatively and positively charged proteins at the water/air interface.

amino acids present in the protein (4x tryptophan, 4x tyrosin, 4x phenylalanin, 3x histidin). In a previous intensity VSFG study of aqueous β-lactoglobulin the band at $\sim$3060 cm^{-1} was used to deduce the absolute water orientation at the protein/water interface by considering its interference with the broad hydrogen-bonded water band.[146]

Changing the pH of the solution does not have a prominent effect on the intensity of the CH vibrational bands at $\sim$2880 and $\sim$2950 cm^{-1}, indicating that the net orientation of the CH groups of the protein does not change when varying the pH. The HD-VSFG signal scales with the number of molecules probed and strongly depends on the net orientation of probed molecules. Hence, the constant intensity of the CH signals indicates that the surface propensity of the protein does not change significantly when varying the pH. The aromatic CH band at $\sim$3060 cm^{-1} only appears as a small dip in the Im$\chi^{(2)}$ spectra and shows no significant change of its phase upon changing the pH.

The OH region of the Im$\chi^{(2)}$ spectrum of aqueous solutions of α-lactalbumin shows substantial changes when the pH is changed. These changes closely follow the net charge of the protein (see Figure 6.7 in Appendix 6.A). At the isoelectric point (IEP) of α-lactalbumin (pH $\sim$4.9), at which the overall charge of the protein is zero, the VSFG signals of the OH stretch vibrations at 3200 cm^{-1} and 3500 cm^{-1} are small, indicating very little net orientation of the OH groups of the water molecules. At pHs above the IEP of α-lactalbumin the signals at 3200 cm^{-1} and 3500 cm^{-1} are both positive, while at pHs lower than the IEP they are both negative. Hence, decreasing the pH changes the orientation of the O–H groups of the water molecules from positive (pointing towards the negatively charged protein at the surface) to negative (pointing away from the positively charged protein). The orientation of the interfacial water molecules at the protein/water interface thus closely follows the electric field induced by the charge state of the protein, as illustrated in Figure 6.2.

The Im$\chi^{(2)}$ spectrum of a concentrated aqueous solution of urea does not significantly differ from that of pure water, as seen in Figure 6.3 a). This result illustrates that urea is not very surface active. The observed spectrum is consistent with the previously reported notion that urea molecules fit well into the hydrogen-bond network of liquid water, and that they have very little effect on the strength of the hydrogen bonds.[162]

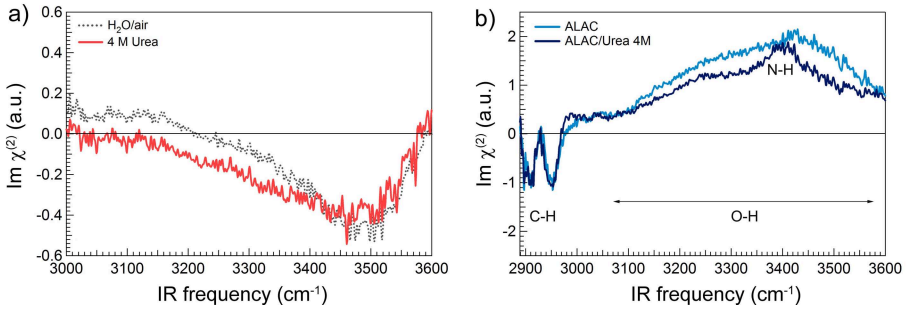

FIGURE 6.3. Imaginary $\chi^{(2)}$ spectra of H_2O and 4 M Urea in H_2O interfaces (a). Imaginary $\chi^{(2)}$ spectra of α-lactalbumin in H_2O and in 4 M urea interfaces at pH=9 (b).

Upon addition of urea to an α-lactalbumin solution the overall amplitude of the Im$\chi^{(2)}$ spectrum decreases and a new band at $\sim$3380 cm^{-1} appears, as seen in Figure 6.3 b). We assign this new band to the NH stretch vibrations of the NH_2 groups of urea, which is consistent with the IR and Raman spectra of urea, and which agrees with the intensity VSFG data of Cremer and coworkers.[147,163,164] The decrease in amplitude of the Im$\chi^{(2)}$ spectrum probably originates from the reduction of the number of water molecules at the protein/water interface due to the additional presence of urea molecules.

In Figure 6.4 we show the Im$\chi^{(2)}$ spectra of α-lactalbumin in 8 M urea at different pH values. Upon changing the pH of the solution, the sign of the NH vibrational band changes, and follows the same trend as the broad OH vibrational band. At the IEP of α-lactalbumin, only a very weak negative signal at lower frequencies arising from the OH vibrations and a small positive peak of the NH vibrations are observed, indicating that nearly equal amounts of urea molecules have their NH vibrations pointing up as pointing down. At

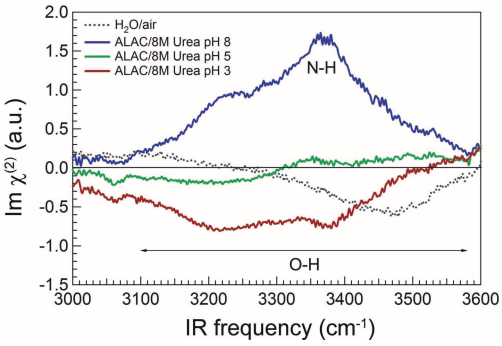

FIGURE 6.4. Imaginary $\chi^{(2)}$ spectra of α-lactalbumin in 8 M urea at different pH values.

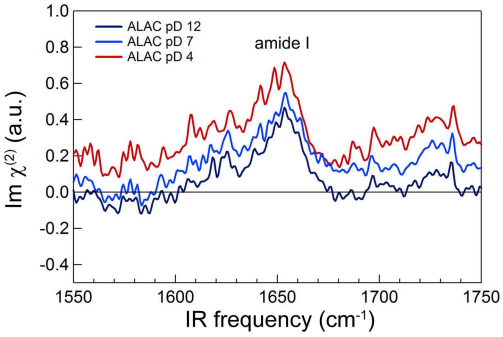

FIGURE 6.5. Imaginary $\chi^{(2)}$ spectra of α-lactalbumin in D_2O at different pD values.

pH values above the IEP (protein negatively charged), the NH vibrations are pointing towards the proteins at the surface, while at pH values below the IEP (protein positively charged) the NH vibrations are pointing downwards into the liquid, in agreement with their expected dipolar orientation.

In Figure 6.5 we show the $\mathrm{Im}\chi^{(2)}$ spectra of α-lactalbumin at different pD values in the frequency range from 1550 to 1750 cm^{-1}. The amide I vibration strongly overlaps with the bending mode of water, which has a frequency at the water/air interface of $\sim$1643 cm^{-1}. This complication can be overcome by using D_2O as a solvent, for which the bending mode possesses a frequency at the water/air interface of $\sim$1209 cm^{-1} (see Figure 6.8 in Appendix 6.A). The most prominent positive spectral feature at $\sim$1650 cm^{-1} originates from the amide I mode, which consists mainly of the C=O stretching vibration with a smaller contribution of the C–N stretching vibration. Interestingly, the $\mathrm{Im}\chi^{(2)}$ spectra of the amide I band do not show a change in sign and only small variations in amplitude when the pD is varied. Quantum chemistry calculations showed that the transition dipole moment of the amide I band is approximately parallel to the C=O bond, and thus a positive sign in the $\mathrm{Im}\chi^{(2)}$ spectrum corresponds to an orientation of the C=O bond towards the bulk of the liquid (the C atom being closest to the surface).[165] Hence, we conclude that the amide groups of α-lactalbumin show a net orientation of their C=O groups pointing into the bulk. This orientation does not change when varying the pD. The observed constant amplitude of the amide I band further suggests that the surface propensity of the protein does not change upon varying the pD, agreeing with the observations for the CH stretch vibrational bands.

The $\mathrm{Im}\chi^{(2)}$ spectra of α-lactalbumin solution in 6.5 M urea at different pD values are shown in Figure 6.6. In the frequency region between 1600 and 1700 cm^{-1}, the spectrum shows a band at $\sim$1620 cm^{-1} associated with the carbonyl stretch vibration of urea, and the amide I band of the protein at $\sim$1650 cm^{-1}. The amide band is still located at 1650 cm^{-1}, even though the addition of urea may lead to a partial denaturation of the protein. At pD values higher than the IEP the carbonyl vibrational band of urea is positive

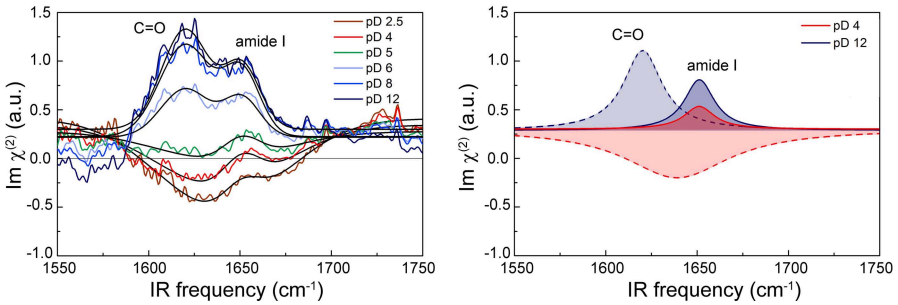

FIGURE 6.6. Left panel: Imaginary $\chi^{(2)}$ spectra of α-lactalbumin in 6.5 M urea at different pD values in the region of amide I vibration. The lines are the result of a fit of the spectra to two bands, one representing the response of urea at $\sim$1620 cm^{-1} (of which the sign depends on the pD), one representing the response of the amide I modes of α-lactalbumin at $\sim$1650 cm^{-1} (of which the sign does not depend on the pD). Right panel: The bands of urea and α-lactalbumin resulting from the fit.

(C=O group of urea is pointing to the bulk), and at lower values it becomes negative, indicating that urea changes its orientation (C=O group pointing to the surface). The orientation of the carbonyl vibrational band of urea thus shows the same pD dependence as observed for the NH vibrational band of urea. In the right panel we show a decomposition of the spectra in the left panel. From this decomposition it is clear that the amide I band of the protein at $\sim$1650 cm^{-1} maintains its positive value regardless of the pD value, similar as we observed in the absence of urea (Figure 6.5). In addition, the urea band shows a blue shift and broadening when the pD of the solution is decreased. These spectral changes could be due to the transient binding of protons to the urea molecules.

We further investigated the pD dependence of Im$\chi^{(2)}$ of the amide II band of α-lactalbumin in 6.5 M urea solution. The amide II band is a combination of the C–N stretch and the in-plane bending of N–H. Changing the pD of the solution did not have a noticeable effect on the intensity of the amide II band (see Figure 6.9 in Appendix 6.A), confirming that the amide groups do not change their net orientation when varying the pD.

From our results we conclude that the orientation of urea closely follows the orientation of the interfacial water molecules, and not the orientation of the protein amide groups. This result strongly indicates that urea is not interacting with the protein directly, and is well embedded in the hydrogen-bond network of water, in agreement with the results of the group of Paul Cremer.[147] Thereby we obtain experimental evidence that the denaturation of proteins by urea does not rely on the hydrogen-bond interactions between urea and the protein amide groups, which agrees with the results of recent molecular dynamics simulations.[166]

6.4 CONCLUSIONS

In conclusion, we performed heterodyne-detected VSFG measurements which enabled us to determine the absolute orientation of water, urea and α-lactalbumin at solution interfaces at different pH values. We find that the orientation of water and urea molecules closely follow the net charge of the protein. We observed that the amide I groups of the protein backbone do not follow the same orientation trend as water and urea, which shows that urea molecules follow more closely the orientation of water than the orientation of the amide groups of the protein backbone. Based on our experimental data we conclude that urea is not binding to the protein backbone, thus supporting an indirect mechanism for protein denaturation.

6.A APPENDIX

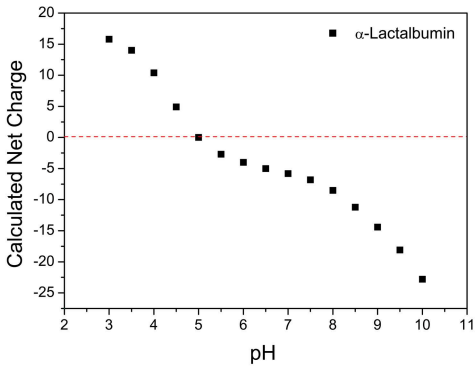

FIGURE 6.7. Calculated net charge of α-Lactalbumin as a function of pH, which was estimated with ProtParam[167] and Protein Calculator v3.4.

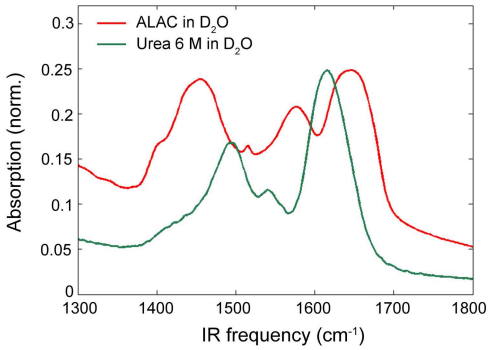

FIGURE 6.8. Linear IR spectra of α-Lactalbumin in D_2O and 6 M Urea in D_2O in the spectral region of the amide I and amide II vibrations.

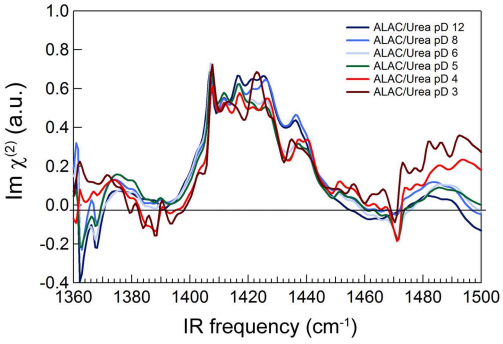

FIGURE 6.9. Imaginary $\chi^{(2)}$ spectra of α-Lactalbumin in 6.5 M urea at different pH values in the spectral region of the amide II vibration.

7

Orientation of Methylguanidinium Ions at the Water/Air Interface

We use heterodyne-detected VSFG to determine the orientation of the main molecular plane of methylguanidinium ions at the surface of aqueous solutions by probing the methyl stretch vibrations under different polarization combinations. We find that for >80% of the methylguanidinium ions the molecular plane is at an angle >20 degrees with respect to the surface plane. Hence, for only a minor fraction of the ions the molecular plane has an orientation (near-)parallel to the surface plane, in contrast to the predictions of recent molecular dynamics simulation studies.

7.1 Introduction

The guanidinium cation ($C(NH_2)_3^+$ or Gdm^+) is one of the strongest and most widely-used protein denaturants.[168] The mechanism underlying its exceptional protein unfolding capacity has been the subject of many experimental and theoretical studies.[169–171] Two main classes of mechanisms have been proposed by which denaturation could occur: either by i) indirect interactions mediated by ion-induced changes of the properties of the water solvent[169,172] or ii) by direct interaction between the Gdm^+ ion and charged or aromatic protein side groups.[173,174]

The notion of an indirect mechanism strongly relies on the specific nature of the interaction between Gdm^+ and water, which has inspired a large number of studies on the structure of such solutions.[143,175,176] In particular, molecular dynamics simulations have given much insight into the ion's fascinating hydration properties.[174,177–179] Due to its planar shape and strongly non-uniform charge distribution, the Gdm^+ ion exhibits a highly anisotropic hydration structure. The net positive charge of the ion makes the lone pairs of the nitrogen atoms poor hydrogen-bond acceptors. As a result, there are few hydrogen bonds formed pointing perpendicular to the molecular plane, essentially rendering the ion hydrophobic along this molecular axis. Instead, the main hydration interac-

tions of the Gdm^+ cation is formed through directional hydrogen bonds donated by the N–H groups oriented in the plane of the ion. Consequently, the water solvent is more structured around Gdm^+ than around most other ions of similar size.

It has been suggested by several authors that the strong anisotropy of the hydration structure and the amphiphilic nature of the Gdm^+ ion are essential for how the ion binds to protein surfaces. While the ion can bind to negatively charged regions by strong in-plane hydrogen bonds, the out-of-plane hydrophobic interaction is thought to align Gdm^+ parallel to hydrophobic and aromatic patches. The strong ion-protein interaction resulting from this alignment has been considered to be an important factor in guanidinium's strong denaturing effect.[173,174,177] The out-of-plane hydrophobicity is even so severe that the existence of Gdm^+- Gdm^+ planar co-ion pairs has been proposed. In both classical and *ab initio* MD simulation studies, Gdm^+ ions have indeed been found to stack. This finding agrees with neutron scattering data.[174,178] This picture was later further experimentally supported by Shih *et al.*,[180] who showed that the red-shift of the nitrogen K-edge X-ray absorption spectroscopy (XAS) measurements could be theoretically reproduced from structures in which guanidinium ions form stacked co-ion pairs. Using quantum chemical calculations on the CCSD(T) level, Inagaki *et al.* found that such structures are stabilized through a subtle energy balance, partly favorable due to π-stacking interactions and the reduction of the hydrophobic effects, while partly repulsive due to net Coulomb interactions.[181] Gdm^+- Gdm^+ co-ion pairing has further been invoked to explain the stabilizing role of arginine-arginine interactions on many protein surfaces.[182–184] While the somewhat unintuitive picture of Gdm^+ co-ion pairing is becoming more and more accepted, this conformation is not supported by the dielectric relaxation spectroscopy (DRS) and conductivity measurements of Hunger *et al.*[176,185]

The anisotropic hydration properties of Gdm^+ leads to quite peculiar behavior of the ion near water/air interfaces. Overall, the water surface region shows a net depletion of guanidinium ions, resulting in an increased surface tension.[186] However, at the surface itself, in the top molecular layer, the concentration of guanidinium ions is enhanced, as was evidenced in recent liquid-jet photoelectron spectroscopy experiments by Werner *et al.*[187] MD simulation studies have found that surface-bound Gdm^+ ions show a strong preferential orientation parallel to the water surface, allowing for the formation of in-plane hydrogen bonds, while de-solvating one of the hydrophobic faces.[188] Similar observations were made in MD simulations where slabs of GdmCl electrolytes were placed between either hydrophobic or hydrophilic plates.[189] The authors found that hydrophobic surfaces induce a stronger orientational parallel ordering of Gdm^+ ions than hydrophilic surfaces, thus further illustrating how the behavior of the ion at interfaces is driven by its amphiphilic nature.

Recently, in a MD simulation study by Ou *et al.* the surface hydration properties of guanidinium were compared to those of methylguanidinium (M-Gdm^+, a derivative of Gdm^+).[190] In particular, the authors studied to what extent solute-induced interfacial solvent density fluctuations can explain the surface

propensity of various orientational configurations of the solute; a topic which recently has attained significant attention for rationalizing the varying surface propensities of simple ions.[191–193] While the net surface activity of M-Gdm$^+$ and Gdm$^+$ was somewhat different, they found that both ions are primarily stabilized at the surface in parallel-oriented configurations.

In this work, we use HD-VSFG to study the orientation of M-Gdm$^+$ ions at the water/air interface. As Gdm$^+$ is fully symmetric, and thus VSFG inactive, we utilize the fact that the methyl group of M-Gdm$^+$ introduces a molecular asymmetry which can be the source of VSFG. By measuring the HD-VSFG response of the symmetric and asymmetric stretch vibrations of the methyl group of M-Gdm$^+$ for different polarization combinations, we determine the orientation of the methyl group and thereby of the M-Gdm$^+$ ion at the water/air interface.

7.2 EXPERIMENTAL

The details of the HD-VSFG setup are presented in Chapter 3. The determination of the imaginary and real part of the second-order susceptibility $\chi^{(2)}$ relies on the generation of a local oscillator signal using a quartz crystal. To determine the absolute sign of the real and imaginary parts of $\chi^{(2)}$, and to obtain an accurate determination of the relative intensities measured in different polarization configurations, we also need to know the effective $\chi^{(2)}$ of quartz in measured polarization combinations. In the co-propagating reflective geometry, the effective second-order susceptibility of quartz has the same sign in an SSP and a PPP polarization configurations, even though the macroscopic second order susceptibilities have different signs.[85] Due to differences in Fresnel factors, the effective susceptibility has not the same value in SSP and PPP. In the geometry of our experiment $\chi^{(2),\mathrm{SSP}}_{\mathrm{eff}}/\chi^{(2),\mathrm{PPP}}_{\mathrm{eff}} \cong 1.14$ in 3000 cm^{-1} region.

The samples were prepared by mixing D_2O ($\geq$99.96 %, Cambridge Isotope Laboratories) and methylguanidine hydrochloride ($\geq$98 %, Sigma-Aldrich).

7.3 THEORY

The key for performing an orientational analysis is to derive the right relations between the microscopic molecular hyperpolarizability $\beta_{i'j'k'}$ tensor elements and the effective nonlinear susceptibility $\chi^{(2)}_{\mathrm{eff}}$, measured at different polarization combinations for a particular vibrational mode. The theory required for such an analysis has been described in detail in the literature.[73,74,76,77,194,195] In Chapters 2.3 – 2.4 we briefly presented the mathematical formulas for the C_{3v} symmetry molecular group at rotationally isotropic achiral interfaces ($C_{\infty v}$) that we need to analyze the results of methyl groups at water interfaces.

One can see that expressions of molecular hyperpolarizabilities for C_{3v} symmetry molecular group (Equations 2.29 and 2.30) can be expressed in term of the orientational parameter D, defined as:

$$D = \frac{\langle cos^3\theta \rangle}{\langle cos\theta \rangle} \tag{7.1}$$

We obtain for the symmetric vibration:

$$\begin{aligned}
\chi^{(2),\mathrm{SS}}_{xxz} =& \frac{1}{2} N_s \beta_{ccc} \langle cos\theta \rangle [(1+R) - (1-R)D] \\
\chi^{(2),\mathrm{SS}}_{xzx} =& \chi^{(2),\mathrm{SS}}_{zxx} = \frac{1}{2} N_s \beta_{ccc} (1-R) \langle cos\theta \rangle [1-D] \\
\chi^{(2),\mathrm{SS}}_{zzz} =& N_s \beta_{ccc} \langle cos\theta \rangle [R + (1-R)D\rangle]
\end{aligned} \tag{7.2}$$

and for the asymmetric vibration:

$$\begin{aligned}
\chi^{(2),\mathrm{AS}}_{xxz} =& - N_s \beta_{aca} \langle cos\theta \rangle (1-D) \\
\chi^{(2),\mathrm{AS}}_{xzx} =& \chi^{(2),\mathrm{AS}}_{zxx} = N_s \beta_{aca} \langle cos\theta \rangle D \\
\chi^{(2),\mathrm{AS}}_{zzz} =& 2 N_s \beta_{aca} \langle cos\theta \rangle (1-D)
\end{aligned} \tag{7.3}$$

where θ is the tilt angle between the methyl C_3 axis and the surface normal z and R is the ratio of hyperpolarizability elements β_{aac}/β_{ccc}, N_s is the number density of the molecules probed at the interface. If one assumes the orientation distribution function to be a δ-function, the tilt angle is given by:

$$\theta_{\mathrm{F}} = arccos(\sqrt{D}) \tag{7.4}$$

The susceptibilities $\chi^{(2),V}_{ijk}$ of the different vibrations V ($V = \{SS,\ AS\}$) determine the effective second-order susceptibilities ($\chi^{(2)}_{\mathrm{eff}}$) measured in SSP and PPP polarization combinations through the following expressions:

$$\begin{aligned}
&\mathrm{SSP}: \\
\chi^{(2),\mathrm{V}}_{\mathrm{eff}} =& L_{yy}(\omega_{\mathrm{SF}}) L_{yy}(\omega_{\mathrm{VIS}}) L_{zz}(\omega_{\mathrm{IR}}) sin\eta_{\mathrm{IR}} \chi^{(2),\mathrm{V}}_{xxz} \\
&\mathrm{PPP}: \\
\chi^{(2),\mathrm{V}}_{\mathrm{eff}} =& - L_{xx}(\omega_{\mathrm{V}}) L_{xx}(\omega_{\mathrm{VIS}}) L_{zz}(\omega_{\mathrm{IR}}) cos\eta_{\mathrm{SF}} cos\eta_{\mathrm{VIS}} sin\eta_{\mathrm{IR}} \chi^{(2),\mathrm{V}}_{xxz} \\
&- L_{xx}(\omega_{\mathrm{SF}}) L_{zz}(\omega_{\mathrm{VIS}}) L_{xx}(\omega_{\mathrm{IR}}) cos\eta_{\mathrm{SF}} sin\eta_{\mathrm{VIS}} cos\eta_{\mathrm{IR}} \chi^{(2),\mathrm{V}}_{xzx} \\
&+ L_{zz}(\omega_{\mathrm{SF}}) L_{xx}(\omega_{\mathrm{VIS}}) L_{xx}(\omega_{\mathrm{IR}}) sin\eta_{\mathrm{SF}} cos\eta_{\mathrm{VIS}} cos\eta_{\mathrm{IR}} \chi^{(2),\mathrm{V}}_{zxx} \\
&+ L_{zz}(\omega_{\mathrm{SF}}) L_{zz}(\omega_{\mathrm{VIS}}) L_{zz}(\omega_{\mathrm{IR}}) sin\eta_{\mathrm{SF}} sin\eta_{\mathrm{VIS}} sin\eta_{\mathrm{IR}} \chi^{(2),\mathrm{V}}_{zzz}
\end{aligned} \tag{7.5}$$

where η_{VIS} and η_{IR} are the incident angles of the VIS (ω_{VIS}) and IR (ω_{IR}) beams, respectively. The generated SF signal (ω_{SF}) is reflected from the surface at an angle η_{SF}. $L_{ii}(i = x, y, z)$ are the Fresnel factors, expressions are given in Eq. (2.24).

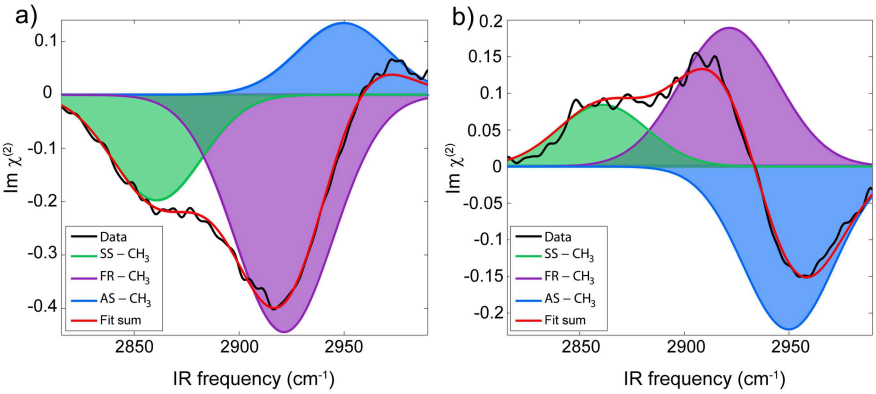

FIGURE 7.1. Imaginary $\chi^{(2)}$ spectra of methylguanidine hydrochloride at different polarization combinations: SSP (a) and PPP (b). Global fitting result is shown in a red line, and contributions of the separate Gaussian peaks are presented in different colors.

One can see from Equations 7.2 and 7.3 that the ratios of the signals measured for different vibrations, for example for the symmetric and asymmetric vibration, will have only one parameter which will depend on θ, namely D. Hence D is the crucial parameter to be determined from VSFG experiment to obtain the molecular orientation of the methyl group at water surfaces. However, D will depend on the distribution function f(θ). Even if this distribution function is known, the D value cannot be used to uniquely determine both the central orientational angle and width of the distribution. We will later come back to what this means in detail for the current investigation.

7.4 RESULTS AND DISCUSSION

In Figure 7.1 we show imaginary $\chi^{(2)}$ spectra of 3 M methylguanidine hydrochloride solutions measured with SSP and PPP polarization combinations. As M-Gdm$^+$ possesses a single methyl group, three possible modes contribute in this frequency region; the symmetric vibration (SS), the Fermi resonance (FR) and the asymmetric vibration (AS). The Fermi resonance is a result of the interaction between symmetric methyl vibration and the overtone of the bending mode ($\sim$1460 cm^{-1}) and it bears the same symmetry as the symmetric mode. We assign the two bands at $\sim$2862 and $\sim$2926 cm^{-1} to the SS and FR mode, respectively, as the sign of these two bands show the same dependence on the polarization combination. The peak at $\sim$2946 cm^{-1} shows the opposite behavior which we thus assign to AS.

The formalism presented in the theory section provides the dependence of $\chi^{(2)}$ on the CH_3 molecular tilt angle relative to the water surface. Thus, by comparing calculations using this formalism to the experimental results mea-

sured in SSP and PPP polarization combinations, we obtain information of the molecular orientation of the methyl group. Essential for making an accurate quantitative interpretation is knowledge of the main optical parameters of the system, mainly the refractive indexes of the medium and interfacial layer as well as the molecular hyperpolarizability values.

It has previously been shown that the molecular tilt angles deduced from VSFG experiments is quite sensitive to the refractive value of interfacial layer (n', see Figure 2.2), used in the analysis.[195] In some studies, n' was taken to be equal to that of the bulk medium value (n_2),[196,197] while in others it was determined using experimental techniques such as ellipsometry.[198] Shen *et al.* derived a formalism for estimating n' when n_2 is known, using a modified Lorentz model for local field correction at the interface, and showed that such a model can be used to determine the molecular orientation of pentyl-cyanoterphenyl molecules at the air/water interface.[195]

Other crucial parameters for the accurate determination of molecular orientation using VSFG are the hyperpolarizability $\beta_{i'j'k'}$ tensor elements (β_{aac}, β_{aca}, β_{ccc}). As expressed in Eq. 2.27, the hyperpolarizability tensor elements are proportional to the product of the dipole moment $\mu_{k'}$ derivative and the Raman polarizability $\alpha_{i'j'}$ derivative tensor elements. Knowledge of those terms allows the elements of the $\beta_{i'j'k'}$ tensor to be determined. Hence, all approaches to obtain $\beta_{i'j'k'}$ tensor elements are based on accurately determining $\alpha_{i'j'}$ and $\mu_{k'}$. There are several methods employed in literature for doing so. Most widely used is the so-called bond additivity method, also called the bond polarizability derivative model, which was first derived by Hirose *et al.*[73,75] In this formalism, the hyperpolarizability tensor elements $\beta_{i'j'k'}$ of CH_3 group are assumed to have C_{3v} symmetry and are expressed in terms of a polarization derivative ratio R of a single CH bond with $C_{\infty v}$ symmetry. The single bond polarizability derivative can be empirically determined by measuring Raman depolarization ratios.[199] For methyl groups attached to different molecules the R values differ, but it was shown from a bond additivity model that $4 > R > 1$. More recently, *ab initio* calculations have been employed to determine hyperpolarizability tensor elements.[200] The advantage of such calculations is that the molecular group does not need to possess a specific symmetry, and thus this method can be used for any complex molecular structure.

Figure 7.2 shows calculated $\chi^{(2)}_{\text{eff}}$ values for the symmetric (SS) and asymmetric (AS) methyl stretch vibrations in both SSP and PPP polarization combinations, plotted against the orientational angle θ relative to the surface normal (see Figure 7.5 in Appendix 7.A for SPS polarization combination). For simplicity, we initially assume a δ-distribution function for angle θ. To estimate the bulk refractive index of a 3 M methylguanidinium hydrochloride solution we assumed that the value would be the same of an equimolar solution of guanidinium hydrochloride. The refractive index of a 8 M guanidinium hydrochloride solution is 1.465 as reported by Sigma Aldrich. We then estimate the value for a 3 M solution using the formalism of Nozaki *et al.*, relating the refractive index and solution molarity.[201] From this approach a value of bulk refractive index of 1.34 was extracted. The refractive index for the corresponding solution sur-

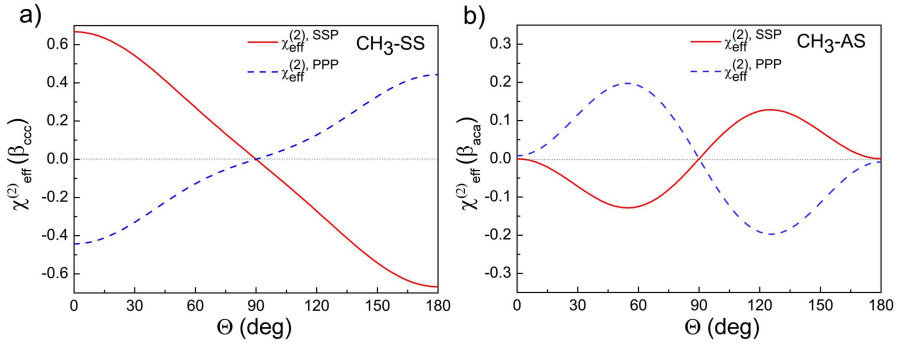

FIGURE 7.2. Calculated $\chi^{(2)}_{\text{eff}}$ (β_{ccc}) versus orientational angle θ for symmetric assuming that $R = 2$ (a) and $\chi^{(2)}_{\text{eff}}$ (β_{aca}) for asymmetric methyl vibration (b). Functions are plotted for SSP and PPP polarization combinations. Details of calculations are given in the text.

face was then estimated following the method proposed by Shen *et al.*,[195] using the bulk refractive index as input, which yielded a value of 1.16. We neglect dispersion of the refractive indexes and use the same values for all frequencies within the VSFG spectrum. It is important to note that for the SS mode the calculated intensity has β_{ccc} as a unit, and the AS mode has β_{aca} as a unit. Hence, the scale of Figure 7.2 a) and b) graphs cannot be compared directly, unless the absolute values of hyperpolarizability tensor elements are known.

Several polarization selection rules for the symmetric and asymmetric CH_3 stretching modes can be concluded from Figure 7.2. For the symmetric mode, the imaginary $\chi^{(2)}$measured with SSP is always at least ∼1.5 times higher than the imaginary $\chi^{(2)}$ measured with PPP and the sign is opposite for the two polarization combinations. For the asymmetric mode the intensity is larger in PPP polarization than SSP (∼2 times) and the sign is also opposite in the two polarization combinations.

With all these mathematical expressions we are now ready to fully fit the experimental data plotted in Fig. 7.1. The expression of the fit procedure is given in the Appendix 7.A. 11 fitting parameters are needed to describe the complete data set; namely, the center frequencies and widths of the AS, FR and SS peaks, the R and D parameters describing the hyperpolarizability ratio ($R = \beta_{aac}/\beta_{ccc}$) and orientational order of the methyl group of M-Gdm$^+$ ion at the water interface, and finally three one dimension-free scaling parameters for scaling the overall intensities. Note however that the relative peak intensities in both polarization combinations is uniquely described by the R and D parameters. The result of the fit is plotted together with the experimental data in Fig. 7.1; the different colors represent the contributions of the respective Gaussian peaks and the red line gives the sum of all the contributing peaks. The resulting fit paramters are given in Table I. The extracted D value is 0.5 ± 0.06. Equation 7.1 can be used to relate this extracted parameter to an angular distri-

TABLE I. Parameters determined from global fitting SSP and PPP spectra of M-Gdm$^+$.

	R	1.0 ± 0.1
	D	0.5 ± 0.06
SS	ω_{SS}	2863 cm^{-1}
	σ_{SS}	23 cm^{-1}
FR	ω_{FR}	2922 cm^{-1}
	σ_{FR}	23 cm^{-1}
AS	ω_{AS}	2950 cm^{-1}
	σ_{AS}	21 cm^{-1}

bution of methyl groups at the water/air interface. The simplest approach is to assume that the distribution can be approximated by a δ-function. Under that approximation a D value of 0.5 ± 0.06 yields a molecular tilt angle θ of $45° \pm 2°$.

As discussed in the introduction, the behavior of the both guanidinium and methylguanidinium cations at the water/air interface has been investigated by Ou *et al.* using MD simulations.[193] They found that close to the Gibbs dividing surface both ions show a strong orientational preference, with the molecular planes aligning parallel to the water surface plane. The average orientation could be well approximated with an angular δ-distribution function at $\theta = 90°$. This prediction stands in rather sharp contrast to our experimentally extracted value of $45° \pm 2°$. Interestingly though, further towards the vapor phase, the simulation of M-Gdm$^+$, in contrast to Gdm$^+$, shows a tendency to orient with the methyl group pointing away from the liquid phase, corresponding to configurations with tilt angles θ close to 0°. This implies that there would be a distribution of M-Gdm$^+$ orientations going from flat at the Gibbs dividing surface, to oriented perpendicular to the surface in the vapor phase. The density profiles reported by Ou *et al.* however shows that the relative contribution from the latter should be rather small, and that the flat configurations ($\theta = 90°$) should strongly dominate.

The experimentally determined value of D of 0.5 ± 0.06 can also correspond to a broad distribution of orientation angles. To construct such a distribution, we use a Gaussian function with central angle θ_c, and which is zero above 90°. This distribution can be rationalized by considering the hydrophobic nature of the methyl group, making it unlikely that surface-bound M-Gdm$^+$ would orient such that the methyl group would be pointing towards the bulk aqueous phase, i.e. $\theta > 90°$). We will refer to such a distribution as a half-Gaussian, defined as:

$$F_{HG}(\theta) = \begin{cases} e^{\dfrac{-(\theta-\theta_c)^2}{2\sigma^2}} & \text{if } 0° < \theta < 90° \\ 0 & \text{if } 90° < \theta < 180° \end{cases} \tag{7.6}$$

D can be evaluated for this distribution using:

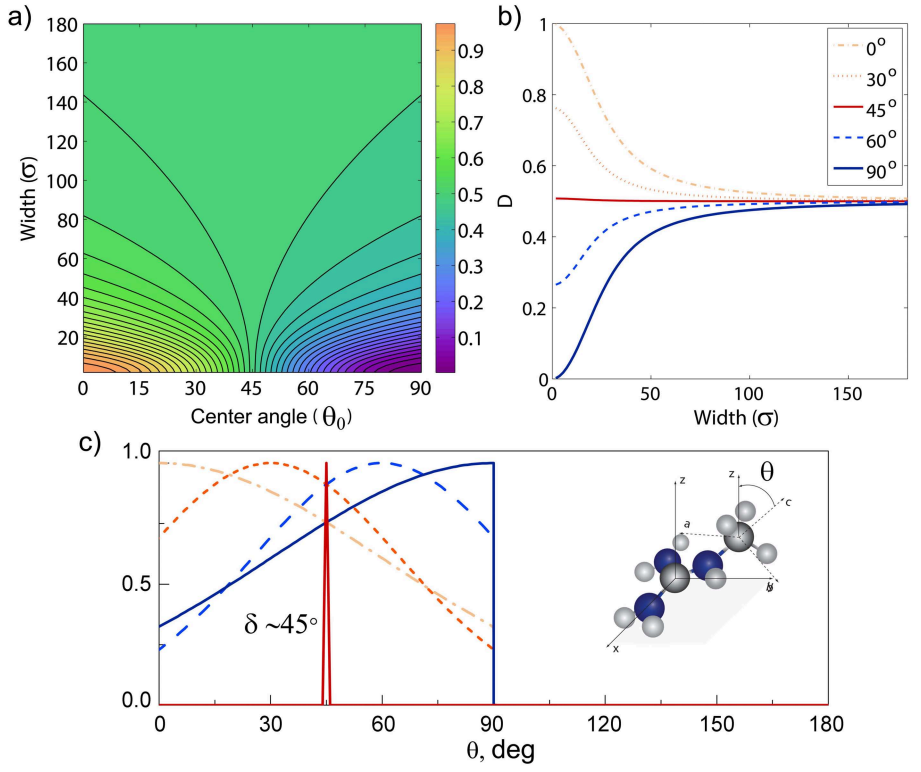

FIGURE 7.3. a) Dependence of D value on the center angle and width as defined in equation 7.7. b) Cuts at various center angles (see legend). c) Half-Gaussian angular distributions at various center angles with corresponding widths, determined from Fig. 7.3b ($\theta_c = 30°$ and $60°$ have width of $\sim 35°$, $\theta_c = 0°$ and $90°$ have width of $\sim 65°$).

$$D = \frac{\int_{0°}^{90°} cos^3\theta sin\theta F_{\mathrm{HG}}(\theta)\, d\theta}{\int_{0°}^{90°} cos\theta sin\theta F_{\mathrm{HG}}(\theta)\, d\theta} \tag{7.7}$$

In Figure 7.3 a) values of the orientational parameter D (calculated from Eq. 7.7) are plotted as a function of the center angle θ_c and width σ, representing different half-Gaussian distribution functions. In Figure 7.3 b) values are shown at various center angles ($\theta_c = 0°$, $30°$, $45°$, $60°$ and $90°$) as a function of the width σ alone. This plot represents vertical cuts of 7.3 a) plot at particular center angles θ_c. The MD simulations of Ou *et al.* suggest that the most probable surface bound configuration would be parallel to the surface flat, which

can be described with a half-Gaussian with center angle θ_c=90°. In this case, to reproduce the experimentally determined D value of 0.5 ± 0.06 we arrive at a minimum width of at least 65°. Figure 7.3 c) shows several half-Gaussian angular distributions with corresponding widths, including one at 90° with a width of 65° and a δ-distribution.

It should hence be clear that by the HD-VSFG technique we cannot distinguish between a δ-distribution centered at ∼45° or a broad half-Gaussian distribution with its maximum at 90° and width ∼65°, as both of them give the same D value. Assuming the second distribution, 80% of all the M-Gdm$^+$ ions would have their methyl groups pointing at an angle smaller than ∼72° relative to the surface normal, meaning that only 20% of the molecules would be lying flat on the surface with an angle < 18° with respect to the surface plane.

Hence, we find that the M-Gdm$^+$ ion is not oriented as parallel to the water/air interface as was predicted with MD simulations. The same notion may apply to the Gdm$^+$ ion, which was found in MD simulations to have a similar flat orientation as the M-Gdm$^+$ ion. Unfortunately, we cannot investigate the orientation of Gdm$^+$ as it is fully symmetric and thus VSFG inactive.

7.5 CONCLUSIONS

We have presented a heterodyne-detected VSFG study of the orientation of methylguanidinium ions at the water/air interface. To this purpose, we measured HD-VSFG spectra of the symmetric and asymmetric methyl stretch vibrations of the ion in SSP and PPP polarization combinations. From these spectra we obtained the ratios of the second-order susceptibility tensor elements that provide information on the molecular orientation of the probed methyl group. Assuming a δ-distribution for the orientation angle, we find that the observed spectra can be well explained if the C_3 axis of the methyl group of methylguanidinium is at an angle of ∼45° with respect to the surface normal. Assuming a half-Gaussian orientational distribution with its maximum at 90° (= parallel to the surface plane), we find that the spectra can only be explained if this distribution has a width >65°. From this, we conclude that >80% of the methylguanidinium ions the molecular plane is at an angle >20° with respect to the surface plane, which implies that only a minor fraction of the ions has an orientation (near-)parallel to the water surface.

7.A APPENDIX

FITTING RESULTS SSP and PPP spectra were globally fitted with three Gaussian peaks and 11 parameters, expressions of each individual peak in both polarization combinations are given by:

$R,\ D,\ x_1 = 0.5N_s\beta_{ccc}\langle cos\theta\rangle,\ x_2 =$ ratio between FR and SS,
$x_3 = -N_s\beta_{aca}\langle cos\theta\rangle$,
ω_{SS} and σ_{SS} − frequency and width of SS,
ω_{FR} and σ_{FR} − frequency and width of FR,
ω_{AS} and σ_{AS} − frequency and width of AS.

Numbers in front of each $\chi^{(2)}_{eff}$ element come from Fresnel factors.
For SSP

$$\begin{aligned}
\chi^{(2),\mathrm{SS}}_{\mathrm{eff}} &= 0.334x_1((1+R)-(1-R)D)\exp\left(\frac{-(\omega-\omega_{\mathrm{SS}})^2}{2\sigma^2_{\mathrm{SS}}}\right)\\
\chi^{(2),\mathrm{FR}}_{\mathrm{eff}} &= 0.334x_1x_2((1+R)-(1-R)D)\exp\left(\frac{-(\omega-\omega_{\mathrm{FR}})^2}{2\sigma^2_{\mathrm{FR}}}\right)\\
\chi^{(2),\mathrm{AS}}_{\mathrm{eff}} &= 0.334x_3(1-D)\exp\left(\frac{-(\omega-\omega_{\mathrm{AS}})^2}{2\sigma^2_{\mathrm{AS}}}\right)
\end{aligned} \tag{7.8}$$

For PPP

$$\begin{aligned}
\chi^{(2),\mathrm{SS}}_{\mathrm{eff}} =&(-0.279x_1((1+R)-(1-R)D)\\
&-0.242x_1((1-R)(1-D))\\
&+0.250x_1((1-R)(1-D))\\
&+0.1372x_1(R+(1-R)D))\exp\left(\frac{-(\omega-\omega_{\mathrm{SS}})^2}{2\sigma^2_{\mathrm{SS}}}\right)\\
\chi^{(2),\mathrm{FR}}_{\mathrm{eff}} =&(-0.279x_1x_2((1+R)-(1-R)D)\\
&-0.242x_1x_2((1-R)(1-D))\\
&+0.250x_1x_2((1-R)(1-D))\\
&+0.1372x_1x_2(R+(1-R)D))\exp\left(\frac{-(\omega-\omega_{\mathrm{FR}})^2}{2\sigma^2_{\mathrm{FR}}}\right)\\
\chi^{(2),\mathrm{AS}}_{\mathrm{eff}} =&(-0.279x_3(1-D)-0.242x_3D+0.250x_3D\\
&+0.137\times(-2x_3)(1-D))\exp\left(\frac{-(\omega-\omega_{\mathrm{AS}})^2}{2\sigma^2_{\mathrm{AS}}}\right)
\end{aligned} \tag{7.9}$$

TABLE II. Parameters determined from global fitting SSP and PPP spectra of M-Gdm$^+$.

	R	1.0 ± 0.1
	D	0.5 ± 0.06
	x_1	-19
	x_2 FR/SS	2.1
	x_3	42
SS	ω_{SS}	2863 cm^{-1}
	σ_{SS}	23 cm^{-1}
FR	ω_{FR}	2922 cm^{-1}
	σ_{FR}	23 cm^{-1}
AS	ω_{AS}	2950 cm^{-1}
	σ_{AS}	21 cm^{-1}

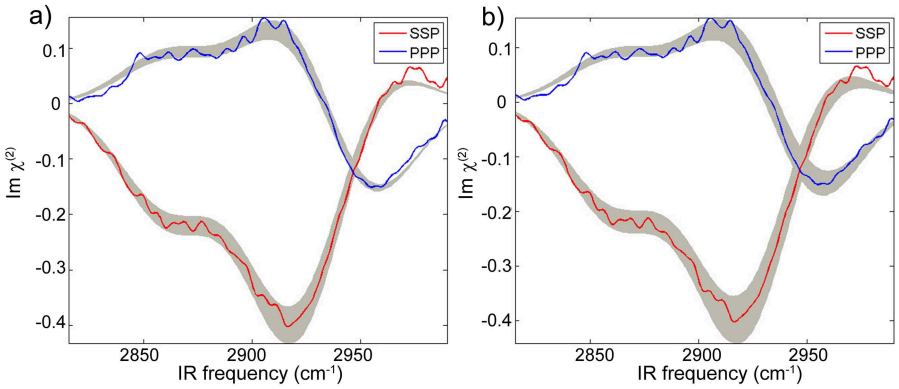

FIGURE 7.4. Imaginary $\chi^{(2)}$ spectra of methylguanidinium hydrochloride at SSP and PPP polarization combinations. Grey areas mark regions when R value is varied ± 0.1 from minimum value (1) (a) and angle θ varied $\pm 5^\circ$ from minimum value of 45° (b).

In Figure 7.5 we show calculated $\chi^{(2)}_{\text{eff}}$ values for the SS and AS methyl stretch vibrations in SSP, SPS and PPP polarization combinations. We do not include SPS polarization combination in our orientational analysis, because it has been demonstrated that the intensities of the asymmetric CH_3 stretching modes of methanol, acetone and acetonitrile, measured with the SPS polarization combination do not correspond to the values predicted by the bond additivity model.[199] For the SSP and PPP polarization combinations, the experimental findings are in excellent agreement with the predicted polarization dependence.[39, 77, 202]

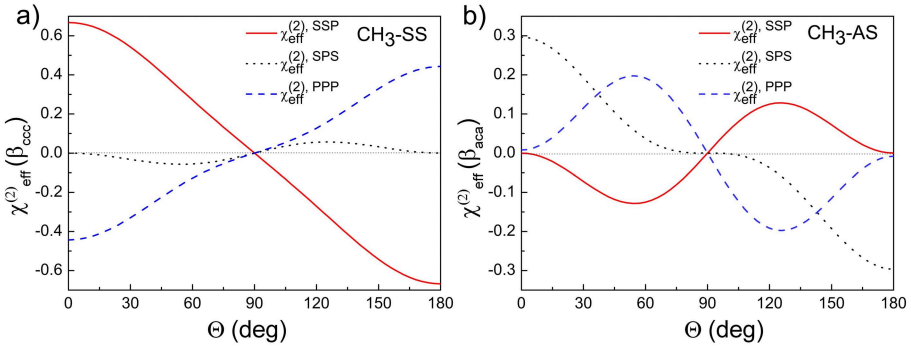

FIGURE 7.5. Calculated $\chi^{(2)}_{\text{eff}}$ (β_{ccc}) versus orientational angle θ for symmetric (a) and $\chi^{(2)}_{\text{eff}}$ (β_{aca}) for asymmetric methyl vibration (b). Functions are plotted for SSP, SPS and PPP polarization combinations. Details of the calculations are given in the Theory section.

8

Observation of a Decrease in the Dissociation of Amino-Acids at the Surface of Water

We use surface-specific intensity VSFG and attenuated total reflection spectroscopy (ATR) to probe the ionization state of the amino-acids L-alanine and L-proline at the air/water surface and in the bulk. The ionization state is determined by probing the vibrational signatures of the carboxylic acid group, representing the non-dissociated acid form, and the carboxylate group, representing the dissociated form, over a wide range of pH values. We find that the carboxylic acid group deprotonates at a significantly higher pH at the interface than in the bulk.

8.1 Introduction

The air/water interface is characterized by a discontinuity and asymmetry in intermolecular interactions, which results in molecular properties that differ from the bulk. For instance, it has been shown that molecules residing at the surface can show a different molecular conformation.[203] The degree of acid dissociation and thus the ionization state of molecules can also be different at the interface compared to the bulk. The degree of acid dissociation of molecules at the air/water interface constitutes an important parameter for the structural properties of molecules near the surface and for the understanding of the reactivity and potential catalytic role of the interface.[204,205]

The acid dissociation constants of molecules in aqueous solution are routinely determined using techniques like potentiometric titration, voltammetry, and electrophoresis.[206] The dissociation constants determined by these techniques represent bulk values, as the signal originating from bulk molecules typically overwhelms the signal arising from those at the surface. Hence, the degree of acid dissociation at the water surface needs to be probed by highly surface-specific techniques.

In previous spectroscopic studies of acid/base pairs it has been found that the surface favors the neutral form of the acid/base pair in comparison to the

bulk. For instance, using highly surface-specific second harmonic generation (SHG) and VSFG, it has been shown for phenol and carboxylic acids that the pK_a increased at the surface, thus favoring the neutral acid species over the anionic conjugate base.[207–210] Similarly, it was found for molecules containing an acid ammonium group that the surface pK_a is lower than the bulk pK_a, thus favoring the neutral amine base species over the cationic quaternary ammonium acid.[207]

A recent infrared reflection-absorption spectroscopy (IRRAS) study of L-phenylalanine that contains both a carboxylic acid group and an amine group, reported a decrease of the pK_a values of both the carboxylic acid and the amine group.[211] Clearly, this behavior cannot be explained from the concept that the surface would favor the neutral species, as for L-phenylalanine this would mean that the surface pK_a of the amine group should be higher than the bulk value. The observation that the pK_a values of both groups were lower than the bulk values was explained from the presence of an enhanced concentration of OH^- in the probed surface region,[211] which for IRRAS has a depth of $\sim$1 μm. This probing depth constitutes thousands of molecular layers, thus making it possible that the pK_a shows a different behavior in the top molecular layers.

Here, we report on a VSFG study of the surface pK_a of the amino-acids L-alanine and L-proline with high surface sensitivity. We compare the surface pK_a with the bulk pK_a that we determine with attenuated total reflection infrared spectroscopy.

8.2 Experimental

ATR spectroscopy is a widely used linear infrared spectroscopic technique that is suited for measuring vibrational spectra of samples that absorb too strong for transmission measurements. The layer thickness that is probed in the ATR geometry is determined by the decay length of the evanescent field, which is a function of wavelength, incident angle and the refractive indexes of the ATR crystal and the sample. At $\sim$1600 cm^{-1} the probed depth is on the order of $\sim$1 μm.[212] We recorded ATR spectra with 0.4 cm^{-1} resolution using a Bruker Vertex80v equipped with an ATR module (Platinum ATR Diamond). The VSFG setup has been described in detail in Chapter 3.

The VSFG and the ATR measurements were performed in solutions of D_2O instead of H_2O to avoid overlap of the ν_{AS,COO^-} ($\sim$1602 cm^{-1}) and ν_{COOD} ($\sim$1720 cm^{-1}) bands with the water bending mode located at $\sim$1670 cm^{-1}. We use a pH meter (Mettler Toledo FE20/EL20) that is calibrated for measuring the pH in H_2O solutions instead of D_2O solutions. The measured pH* of a D_2O solution is transformed to the pD value using the following equation:[213]

$$\mathrm{pD} = \mathrm{pH}^* + 0.44 \tag{8.1}$$

The pD value can be transferred to the pH value of a solution in H_2O of equal acidity using:[213]

$$\mathrm{pH} = 0.929 \times \mathrm{pD} \tag{8.2}$$

The studied samples are solutions of L-Alanine (≥98%) and L-proline (≥99%) in D_2O. These chemicals were obtained from Sigma-Aldrich (St. Louis) and were used without further purification. D_2O (≥99.96%) was purchased from Cambridge Isotope Laboratories. We adjusted the pD of the samples by adding NaOD or DCl (Sigma-Aldrich).

8.3 Results

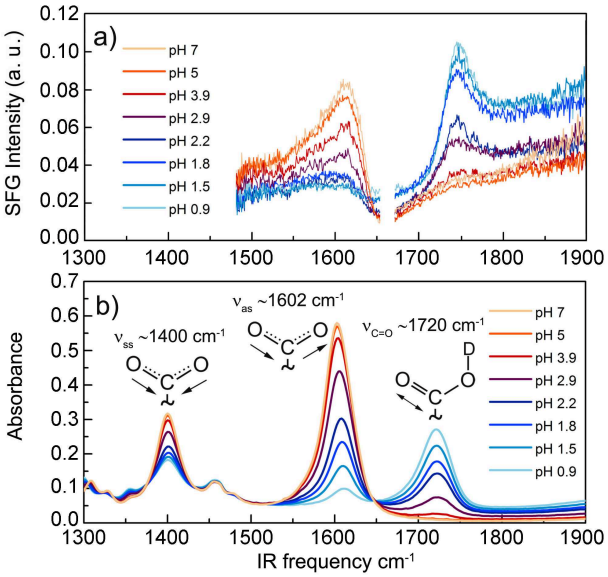

Figure 8.1. Spectra of L-proline in the frequency region of the carbonyl and carboxylate anion vibrations a) VSFG and b) ATR spectra at different pH values. The white area in the VSFG spectra represents a region where no VSFG response was measured.

The surface and bulk pK_a values are determined by measuring the vibrational signatures of the carbonyl and carboxyl groups as a function of pH. Thereby we determine the relative populations of dissociated [A^-] and non-dissociated [HA] at each pH value. The relation of this quantity to the pK_a is given by the Henderson-Hasselbach equation:[214]

$$pK_a = \mathrm{pH} + \log \frac{[\mathrm{HA}]}{[\mathrm{A}^-]} \tag{8.3}$$

In Figure 8.1 we present VSFG (a) and ATR (b) spectra of L-proline at different pH values. We assign the peaks at ∼1400 cm^{-1}, ∼1602 cm^{-1} and

$\sim$1720 cm^{-1} to the symmetric and antisymmetric stretch vibrations of the carboxylate anion (ν_{SS,COO^-} and ν_{AS,COO^-}) and the carbonyl stretch vibration of the carboxylic acid group (ν_{COOD}), respectively. All experiments were performed in deuterated water to avoid spectral overlap with the absorption of the water bending mode. The pH values were determined from the measured pD values of the D_2O solutions as desribed in Experimental section. pH=7 and pD=7.5 both refer to neutral solutions at 293 K ($[H_3O^+] = [OH^-]$ and $[D_3O^+] = [OD^-]$). It is clearly seen in Figure 8.1 that the intensity of the ν_{AS,COO^-} vibrational band increases with increasing pH values, while the intensity of the ν_{COOD} vibrational band decreases, reflecting the shift in the acid-base equilibrium.

To quantify the observed changes of the intensities of ν_{AS,COO^-} and ν_{COOD} vibrational bands, we fit the VSFG spectra at each measured pH value. As described in Chapter 2.6, the VSFG spectra contain resonant and non-resonant

Table I. Fitting parameters for the VSFG spectra of L-proline in ν_{COOD} and ν_{AS,COO^-} vibrational regions.

	ν_{COOD} ω_0=1746 cm^{-1} Γ=20cm^{-1}			ν_{AS,COO^-} ω_0=1628 cm^{-1} Γ=22cm^{-1}		
pH	A_{NR}	φ_{NR}	A_R	A_{NR}	φ_{NR}	A_R
0.9	0.12 ± 0.01	-2 ± 1	3.99 ± 0.06	0.16 ± 0.01	179 ± 12	0.13 ± 0.03
1.5	0.12 ± 0.01	-4 ± 1	3.73 ± 0.04	0.16 ± 0.01	174 ± 4	0.44 ± 0.03
1.8	0.10 ± 0.03	-8 ± 1	3.43 ± 0.06	0.16 ± 0.01	175 ± 2	0.74 ± 0.02
2.2	0.08 ± 0.01	-21 ± 2	2.76 ± 0.06	0.16 ± 0.01	175 ± 2	1.1 ± 0.03
2.9	0.08 ± 0.01	-24 ± 2	1.87 ± 0.05	0.17 ± 0.01	177 ± 2	1.9 ± 0.03
3.9	0	0	0.4 ± 0.1	0.16 ± 0.01	183 ± 1	2.73 ± 0.03
5	–	–	–	0.16 ± 0.01	180 ± 1	3.93 ± 0.03
7	–	–	–	0.16 ± 0.01	179 ± 1	4.27 ± 0.03

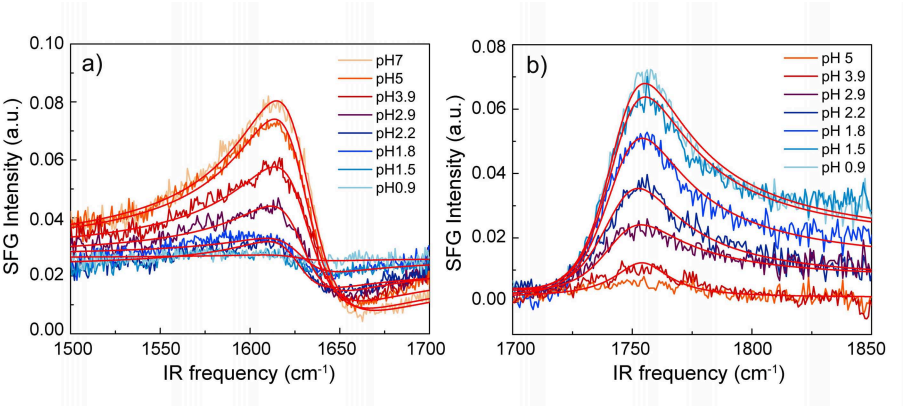

Figure 8.2. VSFG spectra of L-proline in the frequency regions of the ν_{AS,COO^-} (a) and the ν_{COOD} (b) vibrations. The red lines represent the results of the fit described in the text.

contributions. To extract the amplitudes of the resonant contributions of the $\nu_{\mathrm{AS,COO^-}}$ and ν_{COOD} bands at different pH values, we fit VSFG spectra with a non-resonant background and a Lorentzian line shapes for the resonances:

$$I_{\mathrm{VSFG}} \propto \left|\chi^{(2)}_{\mathrm{NR}} + \chi^{(2)}_{\mathrm{R}}\right| = \left|A_{\mathrm{NR}} e^{i\varphi_{\mathrm{NR}}} + \frac{A_i}{\omega - \omega_i + i\Gamma_i}\right|^2 \tag{8.4}$$

where A_{NR} and φ_{NR} is the non-resonant amplitude and phase. A_i, ω_i and Γ_i are the amplitude, center frequency and width of the i-th resonance, respectively.

In fitting the VSFG data, the center frequencies and widths were fixed, and the amplitudes of the resonant and the non-resonant contributions were left free. The measured VSFG spectrum at frequencies >1800 cm^{-1} at pH 7 was subtracted from all spectra before fitting, to remove the weak signal of the low-frequency wing of the broad resonant contribution originating from the vibrational band of the OD stretch vibrations of D_2O centered at ∼2400 cm^{-1}. In Figure 8.2 we show the fitted VSFG spectra of L-proline (red lines) and in Table I we present the parameters obtained from the fit.

TABLE II. Fitting parameters for the L-proline ATR spectra.

		$\omega_0 = 1400\ \mathrm{cm}^{-1}$ $\Gamma = 140\ \mathrm{cm}^{-1}$	$\omega_0 = 1608\ \mathrm{cm}^{-1}$ $\Gamma = 40\ \mathrm{cm}^{-1}$	$\omega_0 = 1720\ \mathrm{cm}^{-1}$ $\Gamma = 45\ \mathrm{cm}^{-1}$
pH	y_0	Peak Area	Peak Area	Peak Area
7	-0.01	8.3 ± 0.7	36.8 ± 0.2	-
5	-0.01	8.1 ± 0.6	36 ± 0.2	-
3.9	-0.01	8.8 ± 0.7	33.8 ± 0.2	1.5 ± 0.3
2.9	-0.007	8.9 ± 0.5	27 ± 0.2	4.6 ± 0.2
2.2	0.002	8.7 ± 0.4	17.6 ± 0.1	9.1 ± 0.2
1.8	0.007	7.9 ± 0.4	13 ± 0.1	11.4 ± 0.1
1.5	0.012	7.4 ± 0.3	8.4 ± 0.1	14.5 ± 0.1
0.9	0.017	7.0 ± 0.4	0.06 ± 0.08	17.7 ± 0.3

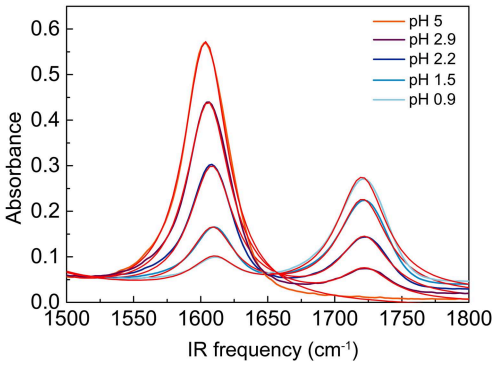

FIGURE 8.3. Experimentally measured ATR spectra of L-proline and Lorentzian model fits.

The ATR spectra were fitted with 3 Lorentzian functions in the frequency region from 1500 to 1800 cm^{-1}. Central frequencies and widths of each Lorentzian peak were kept constant throughout the fits of all spectra. One of the peaks (centered at 1400 cm^{-1}) lays outside the fitted region, but was needed to achieve an accurate fit of the ATR spectra. Figure 8.3 shows fitting results of ATR spectra of L-proline and Table II presents the obtained parameters for each Lorentzian peak.

In Figure 8.4 we plot the pH dependence of the normalized areas (normalized to maximum area) of the ν_{AS,COO^-} and ν_{COOD} vibrations obtained from fitting the VSFG (a) and ATR (b) spectra. Equation 8.3 shows that the pH is equal to the pK_a when the number of dissociated [A^-] molecules is equal to the number of non-dissociated [HA] molecules. From the curves shown in Figure 8.4 we find that for L-proline [COOD] is equal to [COO^-] at a pH value of $\sim 2.2 \pm 0.1$ in the bulk and at a pH value of $\sim 3 \pm 0.2$ at the surface.

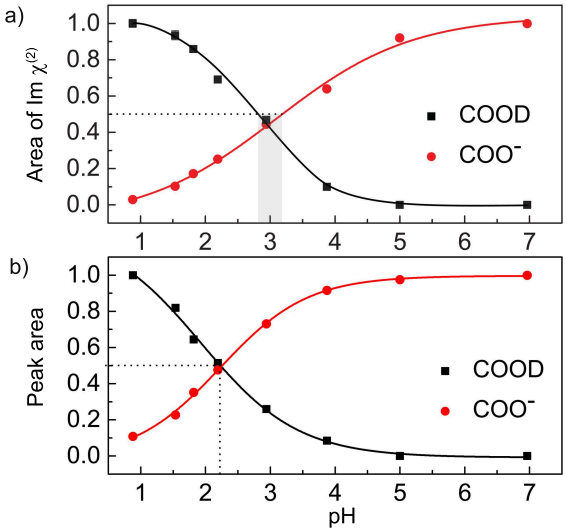

FIGURE 8.4. Areas (normalized) of the bands associated with the ν_{AS,COO^-} and ν_{COOD} vibrations obtained from fitting a) VSFG and b) ATR spectra.

It should be noted that the VSFG intensity not only depends on the number density of the molecules at the interface but also on the molecular orientation. A change in the VSFG intensities of the COO^- and COOD vibrations with a variation of the pH may thus also result from a change in molecular orientation. We checked the potential occurrence of this effect by probing the VSFG spectrum of the CH vibrational bands of L-proline. Intensity of CH vibrational bands of L-proline do not show any prominent changes when varying the pH. This observation indicates that L-proline does not change its orientation at the water surface when the pH is changed.

We also find higher surface pK_a values for the carboxylic acid group of

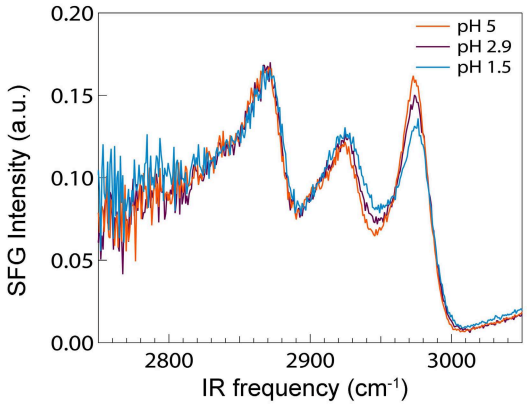

Figure 8.5. VSFG spectra of L-proline (a) and L-alanine (b) in the frequency region of the C–H stretch vibrations at different pH values.

L-alanine ($\sim 2.8 \pm 0.1$ vs 2.5 ± 0.1). Data and results for L-alanine are presented in Appendix 8.A.

We thus find clear evidence that the carboxylic acid groups of amino-acids have a higher surface pK_a than bulk pK_a. This result does not follow the principle that the surface would favour the neutral species of acid/base pairs, as the deprotonation of the carboxylic acid group renders an overall neutral base with an anionic carboxylate group and a cationic quaternary ammonium group. The higher surface pK_a values of L-proline and L-alanine imply that the cationic species of the amino-acids are favoured over the neutral species in the top molecular layers.

8.4 Discussion

The enhanced surface pK_a values of the carboxylic acid group of the amino-acids can be explained as follows. The deprotonation of the carboxylic acid group yields a negatively charged carboxylate group. This process is highly favoured by the formation of strong hydrogen bonds between the negatively charged carboxylate group and the surrounding water molecules. As a result, amino-acids occur as zwitterions in solution whereas in the gas phase non-zwitterionic structures are present. This difference is rationalized by the fact that water strongly stabilizes the zwitterionic form of an amino-acid by forming strong hydrogen bonds.[215] For example, the zwitterion of L-glycine in the gas phase was calculated to be unstable, whereas it is more stable than neutral glycine when solvated by water.[216] It has been found that five water molecules are needed to stabilize the zwitterionic form of L-proline.[217] At the water surface the solvation interactions cannot extend as far as in the bulk and thus the carboxylate group will be less stabilized, which results in a less favourable solvation of the negative charge of the carboxylate anion. As a consequence,

higher bulk pH values are required to induce the dissociation of carboxylic acid groups of molecules at the surface which means that the surface has a higher pK_a value than the bulk. This explanation also implies that the surface pK_a is not determined by the overall charge of the molecule, but rather by the energetics of the local solvation interactions of the acid/base groups with the surrounding water molecules.

An alternative explanation for the increased surface pK_a of the carboxylic acid group of amino-acids would be that the top molecular layers contain an excess concentration of protons. Many MD simulations found that hydrated protons have an enhanced surface propensity at the air/water interface,[218–220] although the different studies do not agree on the amount of the enhancement. The notion that protons are attracted to the interface gets experimental support from surface tension measurements, and from VSFG and SHG experiments of the water/air interface.[221–223] The presence of excess protons at the surface implies that the pH at the water surface would be lower than the bulk pH, which in turn means that the surface number densities of dissociated and non-dissociated molecules become equal to each other at a higher bulk pH value.

8.5 Conclusions

In conclusion, we study the surface pK_a of the carboxylic acid group of the amino-acids L-alanine and L-proline with surface vibrational sum-frequency generation spectroscopy. We observe that the surface pK_a of the carboxylic acid group of L-proline is higher by 0.8 ($\pm$0.2) units than the bulk value, implying a decrease in acidity by a factor of 6. This observation indicates that the surface pK_a is not determined by the overall charge state of the amino-acid, but rather by local solvation interactions of the anionic carboxylate group, or possibly the presence of an excess concentration of protons in the top molecular layers of the aqueous solution. The higher surface pK_a of the carboxylic acid groups of amino-acids may have consequences for the conformation and chemical reactivity of proteins at aqueous surfaces.

8.A Data and Results for L-alanine

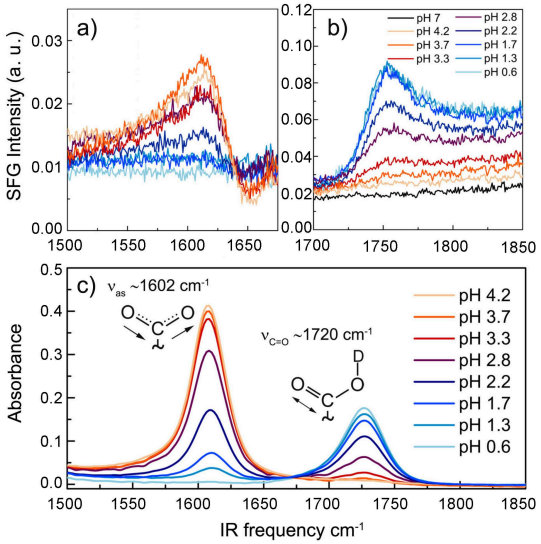

Figure 8.6. VSFG spectra of L-alanine in the frequency regions of the $\nu_{\mathrm{AS,COO^-}}$ (a) and the ν_{COOD} (b) vibrations. ATR spectra in the region 1500 - 1850 cm^{-1} (c).

8.A.1 Fitting L-alanine VSFG Spectra

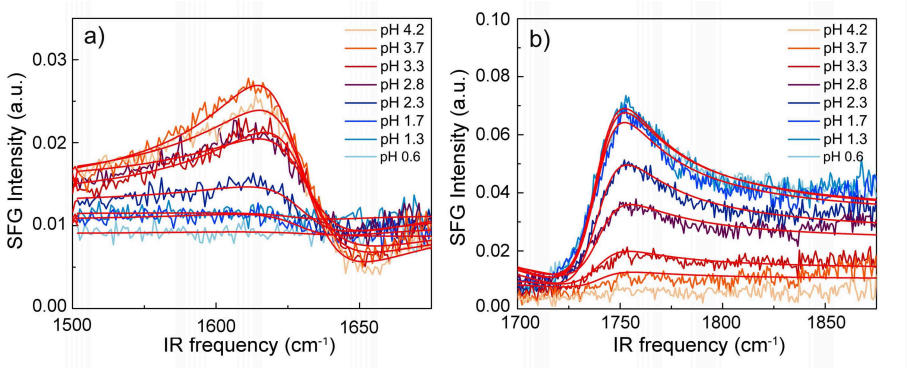

Figure 8.7. VSFG spectra of L-alanine in the frequency regions of the $\nu_{\mathrm{AS,COO^-}}$ (a) and the ν_{COOD} (b) vibrations.

Table III. Fitting parameters for the L-alanine in ν_{COOD} and ν_{AS,COO^-} vibrational regions.

	ν_{COOD} ω_0=1740 cm^{-1} Γ=17 cm^{-1}			ν_{AS,COO^-} ω_0=1630 cm^{-1} Γ=18 cm^{-1}		
pH	A_{NR}	φ_{NR}	A_R	A_{NR}	φ_{NR}	A_R
0.6	0.18 ± 0.01	7 ± 1	2.6 ± 0.1	–	– ± 2	–
1.3	0.17 ± 0.01	6 ± 1	2.7 ± 0.1	0.12 ± 0.01	141 ± 16	0.08 ± 0.01
1.7	0.17 ± 0.01	4 ± 1	2.45 ± 0.04	0.10 ± 0.01	162 ± 1	0.22 ± 0.01
2.3	0.16 ± 0.01	10 ± 1	2.18 ± 0.04	0.11 ± 0.01	170 ± 2	0.44 ± 0.02
2.8	0.15 ± 0.01	9 ± 1	1.38 ± 0.04	0.11 ± 0.01	178 ± 1	0.83 ± 0.02
3.3	0.12 ± 0.01	2 ± 1	0.82 ± 0.03	0.12 ± 0.01	181 ± 1	1.14 ± 0.02
3.7	0.10 ± 0.01	5 ± 1	0.43 ± 0.05	0.11 ± 0.01	191 ± 1	1.38 ± 0.02
4.2	–	–	–	0.11	170	1.43 ± 0.02

8.A.2 Fitting L-alanine ATR Spectra

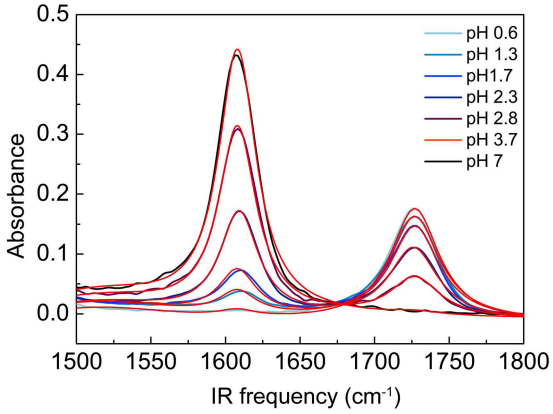

Figure 8.8. Experimentally measured ATR spectra of L-alanine and Lorentzian model fits.

Table IV. Fitting parameters for the L-alanine ATR spectra.

		$\omega_0 = 1515$ cm^{-1} $\Gamma = 140$ cm^{-1}	$\omega_0 = 1608$ cm^{-1} $\Gamma = 30$ cm^{-1}	$\omega_0 = 1727$ cm^{-1} $\Gamma = 40$ cm^{-1}
pH	y_0	Peak Area	Peak Area	Peak Area
7	-0.01	9.8 ± 0.4	20.8 ± 0.2	0.4 ± 0.1
4.2	-0.013	9.4 ± 0.4	19.8 ± 0.1	0.6 ± 0.1
3.7	-0.013	9.5 ± 0.3	19.4 ± 0.1	1.1 ± 0.1
3.3	-0.013	9.2 ± 0.3	18.5 ± 0.1	1.9 ± 0.1
2.8	-0.013	8.6 ± 0.3	14.9 ± 0.4	4.2 ± 0.1
2.3	-0.015	7.2 ± 0.2	8.4 ± 0.1	7.5 ± 0.2
1.7	-0.014	7.1 ± 0.3	3.5 ± 0.1	9.9 ± 0.1
1.3	-0.015	7.3 ± 0.3	1.8 ± 0.08	11.0 ± 0.1
0.6	-0.017	5.9 ± 0.3	0.5 ± 0.08	12 ± 0.1

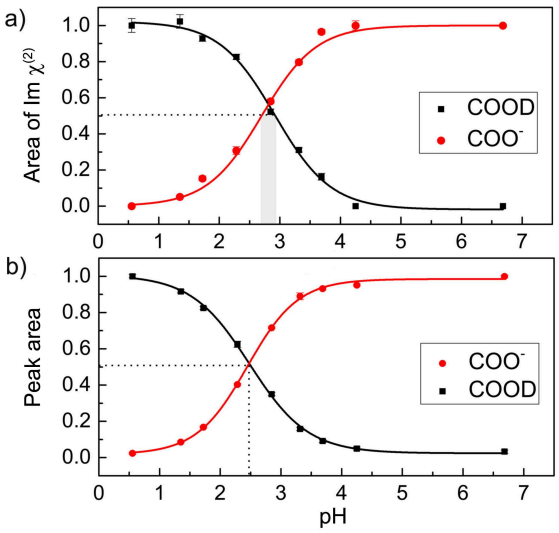

Figure 8.9. pH dependence of the peak areas of the $\nu_{\mathrm{AS,COO^-}}$ and ν_{COOD} vibrations obtained from fitting the VSFG (a) and ATR (b) spectra of L-alanine.

Bibliography

[1] Vrushali R. Hande and Suman Chakrabarty. Structural order of water molecules around hydrophobic solutes: Length-scale dependence and solute-solvent coupling. *The Journal of Physical Chemistry B*, 119(34):11346–11357, 2015. PMID: 26039676.

[2] Hassan Khesbak, Olesya Savchuk, Satoru Tsushima, and Karim Fahmy. The role of water H-bond imbalances in B-DNA substate transitions and peptide recognition revealed by time-resolved FTIR spectroscopy. *Journal of the American Chemical Society*, 133(15):5834–5842, 2011. PMID: 21446714.

[3] Yaakov Levy and Jos N. Onuchic. Water mediation in protein folding and molecular recognition. *Annual Review of Biophysics and Biomolecular Structure*, 35(1):389–415, 2006. PMID: 16689642.

[4] G.M. Cooper. *The Cell: A Molecular Approach, 2nd edition*. Sunderland (MA): Sinauer Associates, 2000.

[5] Roger B. Gregory. *Protein-Solvent Interactions*. Marcel Dekker, Inc., 1995.

[6] Pascale Mentré. Water in the orchestration of the cell machinery. Some misunderstandings: a short review. *Journal of Biological Physics*, 38(1):13–26, 2012.

[7] G. Careri, M. Geraci, A. Giansanti, and J. A. Rupley. Protonic conductivity of hydrated lysozyme powders at megahertz frequencies. *Proceedings of the National Academy of Sciences*, 82(16):5342–5346, 1985.

[8] Martin Chaplin. Do we underestimate the importance of water in cell biology? *Nat. Rev. Mol. Cell Biol.*, 7:861–866, 2006.

[9] P. Ball. Water as an active constituent in cell biology. *Chem. Rev.*, 108:74–108, 2008.

[10] Pavel Jungwirth. Biological water or rather water in biology? *The Journal of Physical Chemistry Letters*, 6(13):2449–2451, 2015. PMID: 26266717.

[11] Maria M. Rhodes, Kamila Réblové, Jiřé Šponer, and Nils G. Walter. Trapped water molecules are essential to structural dynamics and function of a ribozyme. *Proceedings of the National Academy of Sciences*, 103(36):13380–13385, 2006.

[12] Piotr Setny, Riccardo Baron, Peter Michael Kekenes-Huskey, J. Andrew McCammon, and Joachim Dzubiella. Solvent fluctuations in hydrophobic cavity-ligand binding kinetics. *Proceedings of the National Academy of Sciences*, 110(4):1197–1202, 2013.

[13] Ken Dill and Sarina Bromberg. *Molecular Driving Forces: Statistical Thermodynamics in Biology, Chemistry, Physics, and Nanoscience*. Garland Science, 2010.

[14] H. S. Frank and J. W. Evans. Free volume and entropy in condensed systems. 3. Entropy in binary liquid mixtures; partial molar entropy in dilute solutions; structure and thermodynamics of aqueos electrolytes. *J. Chem. Phys.*, 13:507–532, 1945.

[15] W. Kauzmann. Some factors in the interpretation of protein denaturation. volume 14 of *Advances in Protein Chemistry*, pages 1 – 63. Academic Press, 1959.

[16] D. Chandler. Interfaces and the driving force of hydrophobic assembly. *Nature*, 437:640–647, 2005.

[17] Manoj V. Athawale, Sumanth N. Jamadagni, and Shekhar Garde. How hydrophobic hydration responds to solute size and attractions: Theory and simulations. *The Journal of Chemical Physics*, 131(11), 2009.

[18] K.J. Tielrooij, D. Paparo, L. Piatkowski, H.J. Bakker, and M. Bonn. Dielectric relaxation dynamics of water in model membranes probed by terahertz spectroscopy. *Biophysical Journal*, 97(9):2484–2492, August 2009.

[19] P. G. Hudge, D. S. Gond, R. N. Gacche, M. P. Lokhande, and A. C. Kumbharkhane. Dielectric relaxation study of DNA in aqueous solution using time domain reflectometry. *Indian Journal of Physics*, 87(6):543–550, 2013.

[20] Animesh Patra, Trung Quan Luong, Rajib Kumar Mitra, and Martina Havenith. The influence of charge on the structure and dynamics of water encapsulated in reverse micelles. *Phys. Chem. Chem. Phys.*, 16:12875–12883, 2014.

[21] Benjamin Born and Martina Havenith. Terahertz dance of proteins and sugars with water. *Journal of Infrared, Millimeter, and Terahertz Waves*, 30(12):1245–1254, 2009.

[22] Gottfried Otting and Kurt Wuethrich. Studies of protein hydration in aqueous solution by direct NMR observation of individual protein-bound water molecules. *Journal of the American Chemical Society*, 111(5):1871–1875, 1989.

[23] Talia Harris, Or Szekely, and Lucio Frydman. On the potential of hyperpolarized water in biomolecular NMR studies. *The Journal of Physical Chemistry B*, 118(12):3281–3290, 2014. PMID: 24417324.

[24] Nathaniel V. Nucci, Maxim S. Pometun, and A. Joshua Wand. Site-resolved measurement of water-protein interactions by solution nmr. *Nature structural & molecular biology*, 18(2):245–249, 2011.

[25] John T. King and Kevin J. Kubarych. Site-specific coupling of hydration water and protein flexibility studied in solution with ultrafast 2D-IR spectroscopy. *Journal of the American Chemical Society*, 134(45):18705–18712, 2012. PMID: 23101613.

[26] Carien C.M. Groot and Huib J. Bakker. Proteins take up water before unfolding. *The Journal of Physical Chemistry Letters*, 7(10):1800–1804, 2016. PMID: 27120433.

[27] Brigitte Buchli, Steven A. Waldauer, Reto Walser, Mateusz L. Donten, Rolf Pfister, Nicolas Blöchliger, Sandra Steiner, Amedeo Caflisch, Oliver Zerbe, and Peter Hamm. Kinetic response of a photoperturbed allosteric protein. *Proceedings of the National Academy of Sciences*, 110(29):11725–11730, 2013.

[28] Ayanjeet Ghosh, Jun Wang, Yurii S. Moroz, Ivan V. Korendovych, Martin Zanni, William F. DeGrado, Feng Gai, and Robin M. Hochstrasser. 2D IR spectroscopy reveals the role of water in the binding of channel-blocking drugs to the influenza m2 channel. *The Journal of Chemical Physics*, 140(23), 2014.

[29] Kathryn Rebecca Fega, David Scott Wilcox, and Dor Ben-Amotz. Application of raman multivariate curve resolution to solvation-shell spectroscopy. *Appl. Spectrosc.*, 66(3):282–288, 2012.

[30] Giuseppe Bellavia, Laurent Paccou, Samira Achir, Yannick Guinet, Jürgen Siepmann, and Alain Hédoux. Analysis of bulk and hydration water during thermal lysozyme denaturation using raman scattering. *Food Biophysics*, 8(3):170–176, 2013.

[31] Scott A. Lee, Nong-Jian Tao, and Allan Rupprecht. A raman scattering study of the interactions of DNA with its water of hydration. *Journal of Biomolecular Structure and Dynamics*, 31(11):1337–1342, 2013. PMID: 23140399.

[32] Jian-Sheng Jiang and Axel T. Brünger. Protein hydration observed by X-ray diffraction. *Journal of Molecular Biology*, 243(1):100 – 115, 1994.

[33] D. I. Svergun, S. Richard, M. H. J. Koch, Z. Sayers, S. Kuprin, and G. Zaccai. Protein hydration in solution: Experimental observation by X-ray and neutron scattering. *Proceedings of the National Academy of Sciences*, 95(5):2267–2272, 1998.

[34] Eva Nittinger, Nadine Schneider, Gudrun Lange, and Matthias Rarey. Evidence of water molecules–a statistical evaluation of water molecules based on electron density. *Journal of Chemical Information and Modeling*, 55(4):771–783, 2015. PMID: 25742501.

[35] Katrin Amann-Winkel, Marie-Claire Bellissent-Funel, Livia E. Bove, Thomas Loerting, Anders Nilsson, Alessandro Paciaroni, Daniel Schlesinger, and Lawrie Skinner. X-ray and neutron scattering of water. *Chemical Reviews*, 116(13):7570–7589, 2016. PMID: 27195477.

[36] Jonathan D. Nickels, Hugh O'Neill, Liang Hong, Madhusudan Tyagi, Georg Ehlers, Kevin L. Weiss, Qiu Zhang, Zheng Yi, Eugene Mamontov, Jeremy C. Smith, and Alexei P. Sokolov. Dynamics of protein and its hydration water: Neutron scattering studies on fully deuterated GFP. *Biophysical Journal*, 103(7):1566–1575, 2012.

[37] J.H. Hunt, P. Guyot-Sionnest, and Y.R. Shen. Observation of C-H stretch vibrations of monolayers of molecules optical sum-frequency generation. *Chemical Physics Letters*, 133(3):189 – 192, 1987.

[38] A.L. Harris, C.E.D. Chidsey, N.J. Levinos, and D.N. Loiacono. Monolayer vibrational spectroscopy by infrared-visible sum generation at metal and semiconductor surfaces. *Chemical Physics Letters*, 141(4):350 – 356, 1987.

[39] R. Superfine, J. Y. Huang, and Y. R. Shen. Nonlinear optical studies of the pure liquid/vapor interface: Vibrational spectra and polar ordering. *Phys. Rev. Lett.*, 66:1066–1069, Feb 1991.

[40] Lee J. Richter, Teresa P. Petralli-Mallow, and John C. Stephenson. Vibrationally resolved sum-frequency generation with broad-bandwidth infrared pulses. *Opt. Lett.*, 23(20):1594–1596, Oct 1998.

[41] Na Ji, Victor Ostroverkhov, Chao-Yuan Chen, and Yuen-Ron Shen. Phase-sensitive sum-frequency vibrational spectroscopy and its application to studies of interfacial alkyl chains. *Journal of the American Chemical Society*, 129(33):10056 – 10057, 2007. PMID: 17661466.

[42] Jun Kubota and Kazunari Domen. Study of the dynamics of surface molecules by time-resolved sum-frequency generation spectroscopy. *Analytical and Bioanalytical Chemistry*, 388(1):17–27, 2007.

[43] Avishek Ghosh, Marc Smits, Jens Bredenbeck, Niels Dijkhuizen, and Mischa Bonn. Femtosecond time-resolved and two-dimensional vibrational sum frequency spectroscopic instrumentation to study structural dynamics at interfaces. *Review of Scientific Instruments*, 79(9), 2008.

[44] Ruth A. Livingstone, Yuki Nagata, Mischa Bonn, and Ellen H. G. Backus. Two types of water at the water/surfactant interface revealed by time-resolved vibrational spectroscopy. *Journal of the American Chemical Society*, 137(47):14912–14919, 2015. PMID: 26544087.

[45] Zhen Zhang, Lukasz Piatkowski, Huib J. Bakker, and Mischa Bonn. Communication: Interfacial water structure revealed by ultrafast two-dimensional surface vibrational spectroscopy. *The Journal of Chemical Physics*, 135(2), 2011.

[46] Prashant Chandra Singh, Satoshi Nihonyanagi, Shoichi Yamaguchi, and Tahei Tahara. Ultrafast vibrational dynamics of water at a charged interface revealed by two-dimensional heterodyne-detected vibrational sum frequency generation. *The Journal of Chemical Physics*, 137(9), 2012.

[47] Ken ichi Inoue, Prashant C. Singh, Satoshi Nihonyanagi, Shoichi Yamaguchi, and Tahei Tahara. Ultrafast vibrational dynamics of water at a zwitterionic lipid/water interface revealed by two-dimensional heterodyne-detected vibrational sum frequency generation (2d hd-vsfg). In *19th International Conference on Ultrafast Phenomena*, page 07.Mon.P1.27. Optical Society of America, 2014.

[48] Mischa Bonn, Yuki Nagata, and Ellen H. G. Backus. Molecular structure and dynamics of water at the water/air interface studied with surface-specific vibrational spectroscopy. *Angewandte Chemie International Edition*, 54(19):5560–5576, 2015.

[49] Ran ran Feng, Yuan Guo, Rong Lü, Luis Velarde, and Hong fei Wang. Consistency in the sum frequency generation intensity and phase vibrational spectra of the air/neat water interface. *The Journal of Physical Chemistry A*, 115(23):6015–6027, 2011. PMID: 21306145.

[50] Quan Du, Eric Freysz, and Y. Ron Shen. Surface vibrational spectroscopic studies of hydrogen bonding and hydrophobicity. *Science*, 264(5160):826–828, 1994.

[51] Elizabeth A. Raymond, Teresa L. Tarbuck, Mac G. Brown, and Geraldine L. Richmond. Hydrogen-bonding interactions at the vapor/water interface investigated by vibrational sum-frequency spectroscopy of $HOD/H_2O/D_2O$ mixtures and molecular dynamics simulations. *The Journal of Physical Chemistry B*, 107(2):546–556, 2003.

[52] V. Buch, T. Tarbuck, G. L. Richmond, H. Groenzin, I. Li, and M. J. Shultz. Sum frequency generation surface spectra of ice, water, and acid solution investigated by an exciton model. *The Journal of Chemical Physics*, 127(20), 2007.

[53] E. A. Raymond, T. L. Tarbuck, and G. L. Richmond. Isotopic dilution studies of the vapor/water interface as investigated by vibrational sum-frequency spectroscopy. *The Journal of Physical Chemistry B*, 106(11):2817–2820, 2002.

[54] M. Sovago, R. K. Campen, G. W. H. Wurpel, M. Muller, H. J. Bakker, and M. Bonn. Vibrational response of hydrogen-bonded interfacial water is

dominated by intramolecular coupling. *Physical Review Letters*, 100:173901, 2008.

[55] Piotr A. Pieniazek, Craig J. Tainter, and James L. Skinner. Surface of liquid water: Three-body interactions and vibrational sum-frequency spectroscopy. *Journal of the American Chemical Society*, 133(27):10360–10363, 2011. PMID: 21675746.

[56] Yuen Ron Shen and Victor Ostroverkhov. Sum-frequency vibrational spectroscopy on water interfaces: Polar orientation of water molecules at interfaces. *Chemical Reviews*, 106(4):1140–1154, 2006. PMID: 16608175.

[57] S. Nihonyanagi, S. Yamaguchi, and T. Tahara. Direct evidence for orientational flip-flop of water molecules at charged interfaces: A heterodyne-detected vibrational sum frequency generation study. *JCP*, 130:204704–5, 2009.

[58] T. Ishiyama and A. Morita. Vibrational spectroscopic response of intermolecular orientational correlation at the water surface. *J. Phys. Chem. C*, 113:16299–16302, 2009.

[59] P. A. Pieniazek, C. J. Tainter, and J. L. Skinner. Interpretation of the water surface vibrational sum-frequency spectrum. *J. Chem. Phys.*, 135:044701, 2011.

[60] S. Nihonyanagi, R. Kusaka, K. ichi Inoue, A. Adhikari, S. Yamaguchi, and T. Tahara. Accurate determination of complex $\chi^{(2)}$ spectrum of the air/water interface. *J. Chem. Phys.*, 143:124707–4, 2015.

[61] Akihiro Morita and James T. Hynes. A theoretical analysis of the sum frequency generation spectrum of the water surface. *Chemical Physics*, 258:371 – 390, 2000.

[62] Dave S. Walker and Geraldine L. Richmond. Understanding the effects of hydrogen bonding at the vapor/water interface: Vibrational sum frequency spectroscopy of h2o/hod/d2o mixtures studied using molecular dynamics simulations. *The Journal of Physical Chemistry C*, 111(23):8321–8330, 2007.

[63] B. M. Auer and J. L. Skinner. Vibrational sum-frequency spectroscopy of the liquid/vapor interface for dilute HOD in D_2O. *The Journal of Chemical Physics*, 129(21), 2008.

[64] B. M. Auer and J. L. Skinner. Vibrational sum-frequency spectroscopy of the water liquid/vapor interface. *The Journal of Physical Chemistry B*, 113(13):4125–4130, 2009.

[65] B.M. Auer and J.L. Skinner. Water: Hydrogen bonding and vibrational spectroscopy, in the bulk liquid and at the liquid/vapor interface. *Chemical Physics Letters*, 470:13 – 20, 2009.

[66] Tatsuya Ishiyama, Takako Imamura, and Akihiro Morita. Theoretical studies of structures and vibrational sum frequency generation spectra at aqueous interfaces. *Chemical Reviews*, 114(17):8447–8470, 2014. PMID: 24678883.

[67] Yizhak Marcus. Tetraalkylammonium ions in aqueous and non-aqueous solutions. *Journal of Solution Chemistry*, 37(8):1071–1098, 2008.

[68] R. W. Boyd. *Nonlinear Optics*. Acadmeic Press, 2003.

[69] P.B. Miranda and Y.R. Shen. Liquid interfaces: A study by sum-frequency vibrational spectroscopy. *J. Phys. Chem*, 103:3292–3307, 1999.

[70] Xing Wei, Seok-Cheol Hong, Xiaowei Zhuang, Tomohisa Goto, and Y. R. Shen. Nonlinear optical studies of liquid crystal alignment on a rubbed polyvinyl alcohol surface. *Phys. Rev. E*, 62:5160–5172, Oct 2000.

[71] H. Goldstein. *Classical Mechanics*. New York: Addison-Wesley, 2000.

[72] Chiaki Hirose, Naotoshi Akamatsu, and Kazunari Domen. Formulas for the analysis of the surface SFG spectrum and transformation coefficients of cartesian SFG tensor components. *Appl. Spectrosc.*, 46(6):1051–1072, Jun 1992.

[73] Chiaki Hirose, Naotoshi Akamatsu, and Kazunari Domen. Formulas for the analysis of surface sum-frequency generation spectrum by CH stretching modes of methyl and methylene groups. *The Journal of Chemical Physics*, 96(2):997–1004, 1992.

[74] Hong-Fei Wang, Wei Gan, Rong Lu, Yi Rao, and Bao-Hua Wu. Quantitative spectral and orientational analysis in surface sum frequency generation vibrational spectroscopy (SFG-VS). *International Reviews in Physical Chemistry*, 24(2):191–256, 2005.

[75] Chiaki Hirose, Hiroyoshi Yamamoto, Naotoshi Akamatsu, and Kazunari Domen. Orientation analysis by simulation of vibrational sum frequency generation spectrum: CH stretching bands of the methyl group. *The Journal of Physical Chemistry*, 97(39):10064–10069, 1993.

[76] Rong Lu, Wei Gan, Bao hua Wu, Hua Chen, and Hong fei Wang. Vibrational polarization spectroscopy of CH stretching modes of the methylene group at the vapor/liquid interfaces with sum frequency generation. *The Journal of Physical Chemistry B*, 108(22):7297–7306, 2004.

[77] Rong Lu, Wei Gan, Bao hua Wu, Zhen Zhang, Yuan Guo, and Hong fei Wang. C-H stretching vibrations of methyl, methylene and methine groups at the vapor/alcohol (n = 1 - 8) interfaces. *The Journal of Physical Chemistry B*, 109(29):14118–14129, 2005. PMID: 16852773.

[78] Hong-Fei Wang, Luis Velarde, Wei Gan, and Li Fu. Quantitative sum-frequency generation vibrational spectroscopy of molecular surfaces and interfaces: Lineshape, polarization, and orientation. *Annual Review of Physical Chemistry*, 66(1):189–216, 2015. PMID: 25493712.

[79] Wei Gan, Dan Wu, Zhen Zhang, Ran-ran Feng, and Hong-fei Wang. Polarization and experimental configuration analyses of sum frequency generation vibrational spectra, structure, and orientational motion of the air/water interface. *The Journal of Chemical Physics*, 124(11):114705–16, 2006.

[80] Alexander D. Curtis, Scott R. Burt, Angela R. Calchera, and James E. Patterson. Limitations in the analysis of vibrational sum-frequency spectra arising from the nonresonant contribution. *The Journal of Physical Chemistry C*, 115(23):11550–11559, 2011.

[81] Alexei Lagutchev, Selezion A. Hambir, and Dana D. Dlott. Nonresonant background suppression in broadband vibrational sum-frequency generation spectroscopy. *The Journal of Physical Chemistry C*, 111(37):13645–13647, 2007.

[82] Shoichi Yamaguchi, Kazuya Shiratori, Akihiro Morita, and Tahei Tahara. Electric quadrupole contribution to the nonresonant background of sum frequency generation at air/liquid interfaces. *The Journal of Chemical Physics*, 134(18):184705–8, 2011.

[83] Dennis K. Hore, Mathew Y. Hamamoto, and Geraldine L. Richmond. Mid-infrared second-order susceptibility of α-quartz and its application to visible-infrared surface sum-frequency spectroscopy. *The Journal of Chemical Physics*, 121(24):12589–12594, 2004.

[84] Wei-Tao Liu and Y. R. Shen. Surface vibrational modes of α-quartz(0001) probed by sum-frequency spectroscopy. *Phys. Rev. Lett.*, 101:016101, Jul 2008.

[85] Li Fu, Shun-Li Chen, and Hong-Fei Wang. Validation of spectra and phase in sub-1 cm^{-1} resolution sum-frequency generation vibrational spectroscopy through internal heterodyne phase-resolved measurement. *The Journal of Physical Chemistry B*, 120(8):1579–1589, 2016. PMID: 26509581.

[86] Alexander Geoffrey Lambert. *Sum Frequency Spectroscopy of Adsorption on Hydrophilic Mica Substrates*. PhD thesis, Emmanuel College, University of Cambridge, 2001.

[87] Kazuo Nakamoto. *Infrared and Raman Spectra of Inorganic and Coordination Compounds. Part A: Theory and Applications in Inorganic Chemistry*. John Wiley & Sons, 2009.

[88] Peter Hamm, Robert A. Kaindl, and Jens Stenger. Noise suppression in femtosecond mid-infrared light sources. *Opt. Lett.*, 25(24):1798 – 1800, 2000.

[89] N. Ji, V. Ostroverkhov, C. S. Tian, and Y. R. Shen. Characterization of vibrational resonances of water-vapor interfaces by phase-sensitive sum-frequency spectroscopy. *Phys. Rev. Lett.*, 100:096102, 2008.

[90] S. Nihonyanagi, J. A. Mondal, S. Yamaguchi, and T. Tahara. Structure and dynamics of interfacial water studied by heterodyne-detected vibrational sum-frequency generation. *Annu. Rev. Phys. Chem.*, 64:579–603, 2013.

[91] Y. R. Shen. Phase-sensitive sum-frequency spectroscopy. *Annu. Rev. Phys. Chem.*, 64:129–150, 2013.

[92] R. E. Pool, J. Versluis, E. H. G. Backus, and Misha Bonn. Comparative study of direct and phase-specific vibrational sum-frequency generation spectroscopy: Advantages and limitations. *The Journal of Physical Chemistry*, 115:15362–15369, 2011.

[93] Victor Ostroverkhov, Glenn A. Waychunas, and Y. R. Shen. New information on water interfacial structure revealed by phase-sensitive surface spectroscopy. *Phys. Rev. Lett.*, 94:046102, Feb 2005.

[94] C. Tian, N. Ji, G. A. Waychunas, and Y. R. Shen. Interfacial structures of acidic and basic aqueous solutions. *JACS*, 130:13033–13039, 2008.

[95] S. Nihonyanagi, S. Yamaguchi, and T. Tahara. Water hydrogen bond structure near highly charged interfaces is not like ice. *J. Am. Chem. Soc.*, 132:6867–6869, 2010.

[96] Igor V. Stiopkin, Himali D. Jayathilake, Andrey N. Bordenyuk, and Alexander V. Benderskii. Heterodyne-detected vibrational sum frequency generation spectroscopy. *Journal of the American Chemical Society*, 130(7):2271–2275, 2008. PMID: 18217755.

[97] N. Bloembergen and P. S. Pershan. Light waves at the boundary of nonlinear media. *Phys. Rev.*, 128:606–622, Oct 1962.

[98] A.K. Soper and J.L. Finney. Hydration of methanol in aqueos-solution. *Phys. Rev. Lett.*, 71:4346–4349, 1993.

[99] S. Dixit, S.J. Crain, W.C.K. Poon, J.L. Finney, and A. K. Soper. Molecular segregation observed in a concentrated alcohol-water solution. *Nature*, 416:829–832, 2002.

[100] N. Galamba. Water's structure around hydrophobic solutes and the iceberg model. *J. Phys. Chem*, 117:2153–2159, 2013.

[101] J. G. Davis, K. P. Gierszal, P. Wang, and D. Ben-Amotz. Water structural transformation at molecular hydrophobic interfaces. *Nature*, 491:582–585, 2012.

[102] A. A. Bakulin, M. S. Pshenichnikov, C. Petersen, and H. J. Bakker. Hydrophobic molecules slow down the hydrogen-bond dynamics of water. *J. Phys. Chem*, 115:1821–1829, 2011.

[103] C. Petersen, K.-J. Tielrooij, and H.J. Bakker. Strong temperature dependance of water reorientation in hydrophobic hydration shells. *J. Chem. Phys.*, 130:214511, 2009.

[104] Y. Ishihara, S. Okouchi, and H. Uedaira. Dynamics of hydration of alcohols and diols in aqueous solutions. *J. Chem. Soc. Faraday Trans.*, 93:3337–3342, 1997.

[105] K. Yoshida, K. Ibuki, and M. Ueno. Pressure and temperature effects on ^{2}H spin-lattice relaxation times and ^{1}H chemical shifts in tert-butyl alcohol- and urea-D_2O solutions. *J. Chem. Phys.*, 108:1360–1367, 1998.

[106] D. Laage, G. Stirnemann, and J.T. Hynes. Why water reorientation slows without iceberg formation around hydrophobic solutes. *J. Phys. Chem*, 113:2428–2435, 2009.

[107] J. T. Titantah and M. Karttunen. Long-time correlations and hydrophobe-modified hydrogen-bonding dynamics in hydrophobic hydration. *J. Am. Chem. Soc.*, 134:9362–9368, 2012.

[108] C. S. Tian and Y. R. Shen. Structure and charging of hydrophobic material/water interfaces studied by phase-sensitive sum-frequency vibrational spectroscopy. *PNAS*, 106:15148–15153, 2009.

[109] S. Ye, S. Nihonyanagi, and K. Uosaki. Sum frequency generation (SFG) study of the pH-dependent water structure on a fused quartz surface modifed by an octadecyltrichlorosilane (OTS) monolayer. *Phys. Chem. Chem. Phys.*, 3:3463–3469, 2001.

[110] R. Vacha, S. W. Rick, P. Jungwirth, A. G. F. de Beer, H. B. de Aguiar, J.-S. Samson, and S. Roke. The orientation and charge of water at the hydrophobic oil droplet/water interface. *JACS*, 133:10201–10210, 2011.

[111] L. F. Scatena and G. L. Richmond. Orientation, hydrogen bonding, and penetration of water at the organic/water interface. *J. Phys. Chem.*, 105:11240–11250, 2001.

[112] L. F. Scatena, M. G. Brown, and G. L. Richmond. Water at hydrophobic surfaces: Weak hydrogen bonding and strong orientation effects. *Science*, 292:908–912, 2001.

[113] M. G. Brown, D. S. Walker, E. A. Raymond, and G. L. Richmond. Vibrational sum-frequency spectroscopy of alkane/water interfaces: Experiment and theoretical simulation. *J. Phys. Chem.*, 107:237–244, 2003.

[114] Hidehiko Asanuma, Hidenori Noguchi, Kohei Uosaki, and Hua-Zhong Yu. Water structure at superhydrophobic quartz/water interfaces: A vibrational sum frequency generation spectroscopy study. *The Journal of Physical Chemistry C*, 113(50):21155–21161, 2009.

[115] Eric Tyrode and Jonathan F. D. Liljeblad. Water structure next to ordered and disordered hydrophobic silane monolayers: A vibrational sum frequency spectroscopy study. *The Journal of Physical Chemistry C*, 117(4):1780–1790, 2013.

[116] T. Pfohl, H. Mohwald, and H. Riegler. Ellipsometric study of the wetting of air/water interfaces with hexane, heptane, and octane from saturated alkane vapors. *Langmuir*, 14:5285–5291, 1998.

[117] O.-S. Kwon, H. Jing, K. Shin, X. Wang, and S. K. Satija. Formation of n-alkane layers at the vapor/water interface. *Langmuir*, 23:12249–12253, 2007.

[118] Ellen H. G. Backus, Nuria Garcia-Araez, Mischa Bonn, and Huib J. Bakker. On the role of fresnel factors in sum-frequency generation spectroscopy of metal-water and metal-oxide-water interfaces. *The Journal of Physical Chemistry C*, 116(44):23351–23361, 2012.

[119] A. Morita and J. T. A. Hynes. Theoretical analysis of the sum frequency generation spectrum of the water surface. *Chem. Phys. Lett.*, 258:371–390, 2000.

[120] Satoshi Nihonyanagi, Tatsuya Ishiyama, Touk kwan Lee, Shoichi Yamaguchi, Mischa Bonn, Akihiro Morita, and Tahei Tahara. Unified molecular view of the air/water interface based on experimental and theoretical $\chi^{(2)}$ spectra of an isotopically diluted water surface. *Journal of the American Chemical Society*, 133(42):16875–16880, 2011. PMID: 21899354.

[121] T. Ohto, K. Usui, T. Hasegawa, M. Bonn, and Y. Nagata. Toward ab initio molecular dynamics modeling for sum-frequency generation spectra; an efficient algorithm based on surface-specific velocity-velocity correlation function. *J. Chem. Phys.*, 143:124702–10, 2015.

[122] L. F. Scatena and G. L. Richmond. Aqueous solvation of charge at hydrophobic liquid surfaces. *Chem. Phys. Lett.*, 383:491–495, 2004.

[123] V. Knecht, H.J. Risselada, A.E. Markc, and S.J. Marrink. Electrophoretic mobility does not always reflect the charge on an oil droplet. *J. Colloid Interface Sci.*, 318:477–486, 2008.

[124] Patrice Creux, Jean Lachaise, Alain Graciaa, and James K. Beattie. Specific cation effects at the hydroxide-charged air/water interface. *The Journal of Physical Chemistry C*, 111(9):3753–3755, 2007.

[125] Marcel D. Baer, I-Feng W. Kuo, Douglas J. Tobias, and Christopher J. Mundy. Toward a unified picture of the water self-ions at the air-water interface: A density functional theory perspective. *The Journal of Physical Chemistry B*, 118(28):8364–8372, 2014. PMID: 24762096.

[126] K. Lum, D. Chandler, and J. D. Weeks. Hydrophobicity at small and large length scales. *J. Phys. Chem. B*, 103:4570, 1999.

[127] Wen-Yang Wen. Structural aspects of aqueous tetraalkylammonium salt solutions. *J. Sol. Chem.*, 2:253–276, 1973.

[128] N. Huang, D. Schlesinger, D.Nordlund, C. Huang, T. Tyliszczak, T. M. Weiss, Y. Acremann, L. G. M. Pettersson, and A. Nilsson. Microscopic probing of the size dependence in hydrophobic solvation. *J. Chem. Phys.*, 136:074507–7, 2012.

[129] P.-A. Bergstrom, J. Lindgren, and O. Kristiansson. An IR study of the hydration of Clo_4^-, NO_3^-, I^-, Br^-, Cr^-, and SO_4^{2-} anlons in aqueous solution. *J. Phys. Chem.*, 95:8575–8580, 1991.

[130] F. Hidaka and H. Kanno. Raman OD stretching spectral differences between aqueous and alcoholic tetraalkylammonium chloride solutions. *Chem. Phys. Lett.*, 379, 3-4:216–222, 2003.

[131] K. Tamaki. Surface activity of tetra-n-alkylammonium halides in aqueous solutions. *Bull. Chem. Soc. Jpn.*, 47(11):2764–2767, 1974.

[132] D. Liu, G. Ma, L.M. Levering, and H. C. Allen. Vibrational spectroscopy of aqueos sodium halide solutions and air-liquid interfaces: Observation of increased interfacila depth. *J. Phys. Chem. B*, 108(7):2252–2260, 2004.

[133] D. Verreault and H. C. Allen. Bridging the gap between microscopic and macroscopic views of air/aqueous salt interfaces. *Chem. Phys. Lett.*, 586:1–9, 2013.

[134] S. Strazdaite, J. Versluis, E. H. Backus, and H. J. Bakker. Enhanced ordering of water at hydrophobic surfaces. *J. Chem. Phys.*, 140:054711, 2014.

[135] P. Jungwirth and D. J. Tobias. Specific ion effects at the air/water interface. *Chem. Rev.*, 106:1259–1281, 2006.

[136] T. Ishiyama and A. Morita. Molecular dynamics study of gas-liquid aqueous sodium halide interfaces. I. flexible and polarizable molecular modeling and interfacial properties. *J. Phys. Chem. C*, 111:721–737, 2007.

[137] S. Nihonyanagi, S. Yamaguchi, and T. Tahara. Counterion effect on interfacial water at charged interfaces and its relevance to the hofmeister series. *J. Am. Chem. Soc.*, 136(17):6155–6158, 2014.

[138] P. Ball. Biophysics: More than a bystander. *Nature*, 478:467–468, 2011.

[139] M. Grossman, B. Born, M. Heyden, D. Tworowski, G. B. Fields, I. Sagi, and M. Havenith. Correlated structural kinetics and retarded solvent dynamics at the metalloprotease active site. *Nat. Struct. Mol. Biol.*, 18(10):1102–1108, 2011.

[140] F. Persson and B. Halle. How amide hydrogens exchange in native proteins. *Proc. Natl. Acad. Sci. U.S.A.*, 112:10383–10388, 2015.

[141] K. Meister, S. Strazdaite, A. L. DeVries, S. Lotze, L. L. C. Olijve, I. K. Voets, and H. J. Bakker. Observation of ice-like water layers at an aqueous protein surface. *Proc. Natl. Acad. Sci. U.S.A.*, 111:17732–17736, 2014.

[142] K. Engelhardt, W. Peukert, and B. Braunschweig. Vibrational sum-frequency generation at protein modified air-water interfaces: Effects of molecular structure and surface charging. *Curr. Opin. Colloid Interface Sci.*, 19:207–215, 2014.

[143] Dmitriy Yu. Vorobyev, Chun-Hung Kuo, Jian-Xin Chen, Daniel G. Kuroda, J. Nathan Scott, Jane M. Vanderkooi, and Robin M. Hochstrasser. Ultrafast vibrational spectroscopy of a degenerate mode of guanidinium chloride. *The Journal of Physical Chemistry B*, 113(46):15382–15391, 2009. PMID: 19905022.

[144] Li Fu, Zhuguang Wang, and Elsa C.Y. Yan. Chiral vibrational structures of proteins at interfaces probed by sum frequency generation spectroscopy. *International Journal of Molecular Sciences*, 12(12):9404, 2011.

[145] J. Wang, S. M. Buck, and Z. Chen. Sum frequency generation vibrational spectroscopy studies on protein adsorption. *J. Phys. Chem. B*, 106:11666–11672, 2002.

[146] K. Engelhardt, M. Lexis, G. Gochev, C. Konnerth, R. Miller, N. Willenbacher, W. Peukert, and B. Braunschweig. pH effects on the molecular structure of β-lactoglobulin modified air-water interfaces and its impact on foam rheology. *Langmuir*, 29:11646–11655, 2013.

[147] X. Chen, L. B. Sagle, and P. S. Cremer. Urea orientation at protein surfaces. *J. Am. Chem. Soc.*, 129:15104–15105, 2007.

[148] J. A. Mondal, S. Nihonyanagi, S. Yamaguchi, and T.Tahara. Structure and orientation of water at charged lipid monolayer/water interfaces probed by heterodyne-detected vibrational sum frequency generation spectroscopy. *J. Am. Chem. Soc.*, 132:10656–10657, 2010.

[149] L. Hua, R. Zhou, D. Thirumalai, and B. J. Berne. Urea denaturation by stronger dispersion interactions with proteins than water implies a 2-stage unfolding. *Proc. Natl. Acad. Sci. U.S.A.*, 105:16928–16933, 2008.

[150] B. J. Bennion and V. Daggett. The molecular basis for the chemical denaturation of proteins by urea. *Proc. Natl. Acad. Sci. U.S.A.*, 100:5142–5147, 2003.

[151] P. J. Rossky. Protein denaturation by urea: Slash and bond. *Proc. Natl. Acad. Sci. USA.*, 105(44):16825–16826, 2008.

[152] A. Wallqvist, D.G. Covell, and D. Thirumalai. Hydrophobic interactions in aqueous urea solutions with implications for the mechanism of protein denaturation. *J. Am. Chem. Soc.*, 120:427–428, 1998.

[153] A. K. Soper, E.W. Castner, and A. Luzar. Impact of urea on water structure: a clue to its properties as a denaturant? *Biophys. Chem.*, 105(2-3):649–66, 2003.

[154] H. Frank and F. Franks. Structural approach to the solvent power of water for hydrocarbons; urea as a structure breaker. *J. Chem. Phys.*, 48:4746–4757, 1968.

[155] Y. L. A. Rezus and H. J. Bakker. Effect of urea on the structural dynamics of water. *Proc. Natl. Acad. Sci. U.S.A.*, 103:18417–18420, 2006.

[156] E. A. Permyakov and L. J. Berliner. α-lactalbumin: structure and function. *FEBS Lett.*, 473:269–274, 2000.

[157] E. D. Chrysina, K. Brew, and K. R. Acharya. Crystal structures of apo- and holo-bovine α-lactalbumin at 2.2- resolution reveal an effect of calcium on inter-lobe interactions. *J. Biol. Chem.*, 275:37021–37029, 2000.

[158] S. Hamada and K. Takeda. Conformational changes of alpha-lactalbumin and its fragment, phe31-ile59, induced by sodium dodecyl sulfate. *J. Protein Chem.*, 12(4):477–482, 1993.

[159] K. Kuwajima. The molten globule state of α-lactalbumin. *FASEB j.*, 10:102–109, 1996.

[160] J. C. Conboy, M. C. Messmer, and G. L. Richmond. Dependence of alkyl chain conformation of simple ionic surfactants on head group functionality as studied by vibrational sum-frequency spectroscopy. *J. Phys. Chem. B*, 101:6724–6733, 1997.

[161] K. Meister, S. Lotze, L. L. C. Olijve, A. L. DeVries, J. G. Duman, I. K. Voets, and H. J. Bakker. Investigation of the ice-binding site of an insect antifreeze protein using sum-frequency generation spectroscopy. *J. Phys. Chem. Lett.*, 6:1162–1167, 2015.

[162] D. Bandyopadhyay, S. Mohan, S. K. Ghosh, and N. Choudhury. Molecular dynamics simulation of aqueous urea solution: Is urea a structure breaker? *J. Phys. Chem. B*, 118:11757–11768, 2014.

[163] J. E. Stewart. Infrared absorption spectra of urea, thiourea, and some thiourea-alkali halide complexes. *J. Chem. Phys.*, 26:248–254, 1957.

[164] J. W. Otvos and J. T. Edsall. Raman spectra of deuterium substituted guanidine and urea. *J. Chem. Phys.*, 7:632–632, 1939.

[165] M. Okuno and T. a. Ishibashi. Heterodyne-detected achiral and chiral vibrational sum frequency generation of proteins at air/water interface. *J. Phys. Chem. C*, 119:9947–9954, 2015.

[166] R. Zangi, R. Zhou, and B. J. Berne. Urea's action on hydrophobic interactions. *J. Am. Chem. Soc.*, 131:1535–1541, 2009.

[167] Elisabeth Gasteiger, Christine Hoogland, Alexandre Gattiker, S'everine Duvaud, Marc R. Wilkins, Ron D. Appel, and Amos Bairoch. *Protein Identification and Analysis Tools on the ExPASy Server*, pages 571–607. Humana Press, Totowa, NJ, 2005.

[168] T. Arakawa and S. N. Timasheff. Protein stabilization and destabilization by guanidinium salts. *Biochemistry*, 23:5924?5929, 1984.

[169] Celia A. Schiffer and Volker Dtsch. The role of protein-solvent interactions in protein unfolding. *Current Opinion in Biotechnology*, 7(4):428 – 432, 1996.

[170] Darwin O. V. Alonso and Ken A. Dill. Solvent denaturation and stabilization of globular proteins. *Biochemistry*, 30(24):5974–5985, 1991. PMID: 2043635.

[171] Diwakar Shukla, Curtiss P. Schneider, and Bernhardt L. Trout. Complex interactions between molecular ions in solution and their effect on protein stability. *Journal of the American Chemical Society*, 133(46):18713–18718, 2011. PMID: 21973239.

[172] J. Nathan Scott, Nathaniel V. Nucci, and Jane M. Vanderkooi. Changes in water structure induced by the guanidinium cation and implications for protein denaturation. *The Journal of Physical Chemistry A*, 112(43):10939–10948, 2008. PMID: 18839935.

[173] Edward P. O'Brien, Ruxandra I. Dima, Bernard Brooks, and D. Thirumalai. Interactions between hydrophobic and ionic solutes in aqueous guanidinium chloride and urea solutions: Lessons for protein denaturation mechanism. *Journal of the American Chemical Society*, 129(23):7346–7353, 2007. PMID: 17503819.

[174] Philip E. Mason, Christopher E. Dempsey, George W. Neilson, Steve R. Kline, and John W. Brady. Preferential interactions of guanidinum ions with aromatic groups over aliphatic groups. *Journal of the American Chemical Society*, 131(46):16689–16696, 2009. PMID: 19874022.

[175] Koichiro Miyajima, Hiromitsu Yoshida, Yoshihiro Kuroda, and Masayuki Nakagaki. Studies on the aqueous solutions of guanidinium salts. XIII. NMR study of the interactions between guanidinium salt and tetraalkylammonium salts in water. *Bulletin of the Chemical Society of Japan*, 53:2212, 1980.

[176] Johannes Hunger, Stefan Niedermayer, Richard Buchner, and Glenn Hefter. Are nanoscale ion aggregates present in aqueous solutions of guanidinium salts? *The Journal of Physical Chemistry B*, 114(43):13617–13627, 2010. PMID: 20936836.

[177] Philip E. Mason, George W. Neilson, John E. Enderby, Marie-Louise Saboungi, Christopher E. Dempsey, Jr. Alexander D. MacKerell, and John W. Brady. The structure of aqueous guanidinium chloride solutions. *Journal of the American Chemical Society*, 126(37):11462–11470, 2004. PMID: 15366892.

[178] Mario Vazdar, Frank Uhlig, and Pavel Jungwirth. Like-charge ion pairing in water: An ab initio molecular dynamics study of aqueous guanidinium cations. *The Journal of Physical Chemistry Letters*, 3(15):2021–2024, 2012.

[179] Jeremy L. England and Gilad Haran. Role of solvation effects in protein denaturation: From thermodynamics to single molecules and back. *Annual Review of Physical Chemistry*, 62(1):257–277, 2011. PMID: 21219136.

[180] Orion Shih, Alice H. England, Gregory C. Dallinger, Jacob W. Smith, Kaitlin C. Duffey, Ronald C. Cohen, David Prendergast, and Richard J. Saykally. Cation-cation contact pairing in water: Guanidinium. *The Journal of Chemical Physics*, 139(3):035104–7, 2013.

[181] Taichi Inagaki, Shinji Aono, Hiroshi Nakano, and Takeshi Yamamoto. Like-charge attraction of molecular cations in water: Subtle balance between interionic interactions and ionic solvation effect. *The Journal of Physical Chemistry B*, 118(20):5499–5508, 2014. PMID: 24787756.

[182] Deepa Pednekar, Abhijit Tendulkar, and Susheel Durani. Electrostatics-defying interaction between arginine termini as a thermodynamic driving force in protein-protein interaction. *Proteins: Structure, Function, and Bioinformatics*, 74(1):155–163, 2009.

[183] Marco A. C. Neves, Mark Yeager, and Ruben Abagyan. Unusual arginine formations in protein function and assembly: Rings, strings, and stacks. *The Journal of Physical Chemistry B*, 116(23):7006–7013, 2012. PMID: 22497303.

[184] Mario Vazdar, Jiři Vymětal, Jan Heyda, Jiři Vondrášek, and Pavel Jungwirth. Like-charge guanidinium pairing from molecular dynamics and ab initio calculations. *The Journal of Physical Chemistry A*, 115(41):11193–11201, 2011. PMID: 21721561.

[185] Johannes Hunger, Roland Neueder, Richard Buchner, and Alexander Apelblat. A conductance study of guanidinium chloride, thiocyanate, sulfate, and carbonate in dilute aqueous solutions: Ion-association and carbonate hydrolysis effects. *The Journal of Physical Chemistry B*, 117(2):615–622, 2013. PMID: 23241014.

[186] Ronald Breslow and Tao Guo. Surface tension measurements show that chaotropic salting-in denaturants are not just water-structure breakers. *Proceedings of the National Academy of Sciences of the United States of America*, 87(1):167–169, 1990.

[187] Josephina Werner, Erik Wernersson, Victor Ekholm, Niklas Ottosson, Gunnar Öhrwall, Jan Heyda, Ingmar Persson, Johan Söderström, Pavel Jungwirth, and Olle Björneholm. Surface behavior of hydrated guanidinium and ammonium ions: A comparative study by photoelectron spectroscopy and molecular dynamics. *The Journal of Physical Chemistry B*, 118(25):7119–7127, 2014. PMID: 24871810.

[188] Erik Wernersson, Jan Heyda, Mario Vazdar, Mikael Lund, Philip E. Mason, and Pavel Jungwirth. Orientational dependence of the affinity of guanidinium ions to the water surface. *The Journal of Physical Chemistry B*, 115(43):12521–12526, 2011. PMID: 21985190.

[189] Takahiro Koishi, Kenji Yasuoka, Soohaeng Yoo Willow, Shigenori Fujikawa, and Xiao Cheng Zeng. Molecular insight into different denaturing efficiency of urea, guanidinium, and methanol: A comparative simulation study. *Journal of Chemical Theory and Computation*, 9(6):2540–2551, 2013. PMID: 26583851.

[190] Shuching Ou, Di Cui, and Sandeep Patel. Liquid-vapor interfacial properties of aqueous solutions of guanidinium and methyl guanidinium chloride: Influence of molecular orientation on interface fluctuations. *The Journal of Physical Chemistry B*, 117(39):11719–11731, 2013. PMID: 23937431.

[191] Carl Caleman, Jochen S. Hub, Paul J. van Maaren, and David van der Spoel. Atomistic simulation of ion solvation in water explains surface preference of halides. *Proceedings of the National Academy of Sciences*, 108(17):6838–6842, 2011.

[192] Himanshu Mishra, Shinichi Enami, Robert J. Nielsen, Logan A. Stewart, Michael R. Hoffmann, William A. Goddard III, and Agustín J. Colussi. Brønsted basicity of the air-water interface. *Proceedings of the National Academy of Sciences*, 109(46):18679–18683, 2012.

[193] Shuching Ou, Yuan Hu, Sandeep Patel, and Hongbin Wan. Spherical monovalent ions at aqueous liquid-vapor interfaces: Interfacial stability and induced interface fluctuations. *The Journal of Physical Chemistry B*, 117(39):11732–11742, 2013. PMID: 24032752.

[194] C.D. Stanners, Q. Du, R.P. Chin, P. Cremer, G.A. Somorjai, and Y.-R. Shen. Polar ordering at the liquid-vapor interface of n-alcohols (c1-c8). *Chemical Physics Letters*, 232(4):407 – 413, 1995.

[195] X. Zhuang, P. B. Miranda, D. Kim, and Y. R. Shen. Mapping molecular orientation and conformation at interfaces by surface nonlinear optics. *Phys. Rev. B*, 59:12632–12640, May 1999.

[196] X. Zhuang, D. Wilk, L. Marrucci, and Y. R. Shen. Orientation of amphiphilic molecules on polar substrates. *Phys. Rev. Lett.*, 75:2144–2147, Sep 1995.

[197] T. F. Heinz, H. W. K. Tom, and Y. R. Shen. Determination of molecular orientation of monolayer adsorbates by optical second-harmonic generation. *Phys. Rev. A*, 28:1883–1885, Sep 1983.

[198] R. Braun, B.D. Casson, and C.D. Bain. A sum-frequency study of the two-dimensional phase transition in a monolayer of undecanol on water. *Chemical Physics Letters*, 245(4):326 – 334, 1995.

[199] Hui Wu, Wen-kai Zhang, Wei Gan, Zhi-feng Cui, and Hong-fei Wang. An empirical approach to the bond additivity model in quantitative interpretation of sum frequency generation vibrational spectra. *The Journal of Chemical Physics*, 125(13):133203–13, 2006.

[200] D.K. Hore, D.S. Walker, and G. L. Geraldine. Water at hydrophobic surfaces: When weaker is better. *J. Am. Chem. Soc.*, 130:1800–1801, 2007.

[201] Yasuhiko Nozaki. The preparation of guanidine hydrochloride. In *Enzyme Structure, Part C*, volume 26 of *Methods in Enzymology*, pages 43 – 50. Academic Press, 1972.

[202] Yuh Ling Yeh, Chun Zhang, Hermann Held, A. M. Mebel, Xing Wei, S. H. Lin, and Y. R. Shen. Structure of the acetone liquid/vapor interface. *The Journal of Chemical Physics*, 114(4):1837–1843, 2001.

[203] Yohko F. Yano. Kinetics of protein unfolding at interfaces. *Journal of Physics: Condensed Matter*, 24(50):503101, 2012.

[204] Jochen S. Hub, Maarten G. Wolf, Carl Caleman, Paul J. van Maaren, Gerrit Groenhoff, and David van der Spoel. Thermodynamics of hydronium and hydroxide surface solvation. *Chem. Sci.*, 5:1745–1749, 2014.

[205] Aaron M. Jubb and Heather C. Allen. Bisulfate dehydration at air/solution interfaces probed by vibrational sum frequency generation spectroscopy. *The Journal of Physical Chemistry C*, 116(24):13161–13168, 2012.

[206] Jetse Reijenga, Arno van Hoof, Antonie van Loon, and Bram Teunissen. Development of methods for the determination of pK_a values. *Analytical Chemistry Insights*, 8:53–71, August 2013.

[207] Xiaolin Zhao, Shaowei Ong, Hongfei Wang, and Kenneth B. Eisenthal. New method for determination of surface pK_a using second harmonic generation. *Chemical Physics Letters*, 214(2):203 – 207, 1993.

[208] Yi Rao, Mahamud Subir, Eric A. McArthur, Nicholas J. Turro, and Kenneth B. Eisenthal. Organic ions at the air/water interface. *Chemical Physics Letters*, 477:241 – 244, 2009.

[209] P.B. Miranda, Q. Du, and Y.R. Shen. Interaction of water with a fatty acid langmuir film. *Chemical Physics Letters*, 286:1 – 8, 1998.

[210] Cheng Y. Tang, Zishuai Huang, and Heather C. Allen. Binding of Mg(2+) and Ca(2+) to palmitic acid and deprotonation of the COOH headgroup studied by vibrational sum frequency generation spectroscopy. *The journal of physical chemistry. B*, 114(51):17068–17076, December 2010.

[211] Elizabeth C. Griffith and Veronica Vaida. Ionization state of l-phenylalanine at the air-water interface. *Journal of the American Chemical Society*, 135(2):710–716, 2013. PMID: 23240998.

[212] J. Kiefer, K. Frank, and H. P. Schuchmann. Attenuated total reflection infrared (ATR-IR) spectroscopy of a water-in-oil emulsion. *Society for Applied Spectroscopy*, 65(9):1024–8, 2011.

[213] Artur Krężel and Wojciech Bal. A formula for correlating pK_a values determined in D_2O and H_2O. *Journal of Inorganic Biochemistry*, 98(1):161 – 166, 2004.

[214] Henry N. Po and N. M. Senozan. The henderson-hasselbalch equation: Its history and limitations. *Journal of Chemical Education*, 78(11):1499, 2001.

[215] William D. Price, Rebecca A. Jockusch, and Evan R. Williams. Is arginine a zwitterion in the gas phase? *Journal of the American Chemical Society*, 119(49):11988–11989, 1997. PMID: 16479267.

[216] Jan H. Jensen and Mark S. Gordon. On the number of water molecules necessary to stabilize the glycine zwitterion. *Journal of the American Chemical Society*, 117(31):8159–8170, 1995.

[217] G. Yang, L. Zhou, and Y. Chen. Stabilization of zwitterionic versus canonical proline by water molecules. *SpringerPlus*, 5:19, 2016.

[218] Ying-Lung Steve Tse, Chen Chen, Gerrick E. Lindberg, Revati Kumar, and Gregory A. Voth. Propensity of hydrated excess protons and hydroxide anions for the air-water interface. *Journal of the American Chemical Society*, 137(39):12610–12616, 2015. PMID: 26366480.

[219] Barbara Jagoda-Cwiklik, Lukasz Cwiklik, and Pavel Jungwirth. Behavior of the eigen form of hydronium at the air/water interface. *The Journal of Physical Chemistry A*, 115(23):5881–5886, 2011. PMID: 21214229.

[220] Timothy C. Berkelbach, Hee-Seung Lee, and Mark E. Tuckerman. Concerted hydrogen-bond dynamics in the transport mechanism of the hydrated proton: A first-principles molecular dynamics study. *Phys. Rev. Lett.*, 103:238302, Nov 2009.

[221] Lori M. Levering, M. Roxana Sierra-Hernández, and Heather C. Allen. Observation of hydronium ions at the air-aqueous acid interface: Vibrational spectroscopic studies of aqueous hcl, hbr, and hi. *The Journal of Physical Chemistry C*, 111(25):8814–8826, 2007.

[222] Chuanshan Tian, Na Ji, Glenn A. Waychunas, and Y. Ron Shen. Interfacial structures of acidic and basic aqueous solutions. *Journal of the American Chemical Society*, 130(39):13033–13039, 2008. PMID: 18774819.

[223] Poul B. Petersen, Richard J. Saykally, Martin Mucha, and Pavel Jungwirth. Enhanced concentration of polarizable anions at the liquid water surface:SHG spectroscopy and MD simulations of sodium thiocyanide. *The Journal of Physical Chemistry B*, 109(21):10915–10921, 2005. PMID: 16852329.

8

Summary

There is no doubt that water is very important for numerous biological processes. Protein folding, self-assembly, molecular recognition, proton transport are only few examples to illustrate water's necessity. In the past years various spectroscopic methods as well as molecular dynamics simulations have been performed to understand how water influences the function and activity of biomolecules. The main idea arising from all the studies is that water solvating biomolecules has very distinct properties from aqueous bulk water due to direct or non-direct interactions with the biomolecules. However, in general the number of water molecules affected by the biomolecule is very small compared to the number of bulk water molecules, making it difficult to selectively probe the structure and hydrogen-bonding of water in contact with biomolecules. In addition, some molecules, for example oils, have a very low solubility in water, which makes it particularly challenging to probe the solvating water.

Ideally, a technique that can separate the bulk water molecules from the interfacial water molecules is needed. Vibrational sum-frequency generation spectroscopy (VSFG) is capable to differentiate these two different type of water molecules. Its surface specificity arises from the fact that it is a second-order nonlinear process, which occurs only in a non-centrosymmetric medium. Water molecules in the bulk are randomly oriented and thus the VSFG signal cancels out and only at the interface, where the symmetry is broken, a VSFG signal will be generated. This surface specificity is the key feature of VSFG spectroscopy and sets it apart from other spectroscopic techniques.

Conceptually, VSFG is quite simple - two pulsed laser beams, one at a fixed visible wavelength, the other with a broad infrared spectrum, are overlapped in time and space on the sample surface to generate their sum-frequency. The intensity of the VSFG light will be resonantly enhanced when the frequency of the infrared light matches the frequencies of the molecular vibrations at the surface. Thus VSFG spectra, in a way resemble the spectra generated using linear infrared spectroscopic techniques, but only of the interfacial molecules. A detailed description of VSFG theory and experiment is presented in Chapter 2 and Chapter 3. In this thesis the structure and orientation of water and various biologically relevant molecules have been studied using VSFG as well as heterodyne-detected VSFG.

CHAPTER 4: WATER STRUCTURE AT HYDROPHOBIC SURFACES In order to understand how water interacts with hydrophobic molecules we performed VSFG and heterodyne-detected VSFG studies to specifically probe the structure and hydrogen-bond interactions of water molecules in contact with hydrophobic molecules such as alkanes and polydimethylsiloxane (PDMS). We find that the surface water molecules are much more ordered and have stronger hydrogen bonds at hydrophobic interfaces than at the air/H_2O interface. From heterodyne-detected VSFG measurements we were able to determine the absolute orientation of water molecules and we found that most water molecules have their hydrogen atoms pointing towards the hydrophobic layer. With increasing temperature the VSFG intensity decreases and the VSFG spectrum shows a significant blue-shift, indicating that the ordering of the water decreases and the hydrogen bonds get weaker. Additionally, we investigated the effect of the pH of the solution on the VSFG signal. This enhanced water structure at water/hydrophobe interfaces is a result of a highly corrugated surface with the methyl groups protruding into the water. Water network can fold around these methyl groups, which results in an enhanced water structure and the hydrogen-bond interaction. We further discuss how imbalance in donating and accepting hydrogen bonds at the water/hydrophobe interface could lead to an excess hydroxide concentration, which would enhance water structure as well. Both explanations can be present at the water/hydrophobe interface and even enhance each other.

CHAPTER 5: HYDROPHOBIC HYDRATION AND ELECTROSTATIC INTERACTIONS Tetra-n-alkylammonium salts (TTA^+) are often used as model systems to study hydrophobic hydration. TTA^+ cations display both hydrophobic and electrostatic interactions. Thus the question arises whether hydrophobic hydration or electrostatic interaction mainly affects water molecules solvating TTA^+ cations. The hydrophobic interactions can be tuned by changing the length of the alkyl chains. We have investigated water structure and hydrogen bonding at the surface of tetra-n-alkylammonium bromide salt solutions. We find that short-chain tetra-n-alkylammonium bromides (n = 1, 2) do not alter water structure by much, which can be explained by the fact that they are not very surface active. Only a minor blue-shift and slight increase in VSFG spectra were observed due to water molecules forming hydrogen bonds with the counter-ion bromide. In contrast, long-chain TAABr (n = 3, 4) induce very strong changes in the VSFG spectra. At low bulk concentrations water molecules are on average oriented with their dipoles pointing to the bulk due to the electric field created by TAA^+ ions being at the top most layer and Br^- ions located deeper down in the solution. Surprisingly, VSFG spectra are strongly red-shifted in contrast to VSFG spectra of short-chain TAABr solutions, which is due to hydrophobic hydration effect. At high concentrations orientation of water molecules and shift of VSFG spectra reverses as a result of the cluster formations between TAA^+ and Br^- ions at the solution surface.

CHAPTER 6: ORIENTATION OF POLAR MOLECULES NEAR CHARGED PROTEIN INTERFACES Urea is one of the most widely used protein denaturant, yet the underlying mechanism of the denaturation process is still not fully understood. Experimental evidences for direct denaturation mechanism, as well as for indirect have been found. Recently, intensity VSFG studies by the group of Paul Cremer showed that the orientation of urea molecules at the protein interface depends on the net charge of the protein. Moreover, this orientation closely follows the orientation of the interfacial water molecules, which was interpreted as evidence for an indirect mechanism. However, the change of urea orientation might also be caused by a flipping of the protein amide groups with which the urea molecules can form hydrogen bonds. This would indicate towards direct denaturation mechanism. We explored this possibility by studying orientation of water, urea and the amide groups of α-lactalbumin with heterodyne-detected VSFG. We found that the orientation of the amide groups of the protein does not show the same pH dependence as urea and water molecules. This finding clearly shows that urea is not directly binding to the protein, and supports the indirect mechanism of the urea protein denaturation.

CHAPTER 7: ABSOLUTE ORIENTATION OF METHYLGUANIDINIUM AT WATER/AIR INTERFACE The guanidinium cation (Gdm^+) is another widely used denaturant. The mechanism of the denaturation as well as fascinating ion's hydration properties have been studied intensively with molecular dynamics (MD) simulations. These simulations find that at the water surface guanidinium ions are preferentially oriented with their main molecular plane parallel orientation to the water surface. This preferred parallel orientation at the water surface has been explained from the anisotropic hydration of the ion. Recently, the hydration properties of methylguanidinium (M-Gdm^+), a derivative of Gdm^+, have been investigated, and it was found that M-Gdm^+ as well shows a preferred parallel orientation at water surface. We use HD-VSFG to study the orientation of M-Gdm^+ ions at the water/air interface. We perform this study on M-Gdm^+, because Gdm^+ is fully symmetric and is thus VSFG inactive. By measuring the polarization dependence of the VSFG signal for the methyl vibrational modes and assuming the same tilt angle for all M-Gdm^+, we find a tilt angle of $\sim 45^\circ$ of the molecular plane. However, the data can also be explained with a broad angular distribution function formed by a half-Gaussian distribution centered at 90° with respect to the surface normal (i.e.parallel to the water surface) and a width of $\sim 65^\circ$. We conclude, that more than 80% of the M-Gdm^+ ions have an angle larger than 20°, which shows that only a very small fraction of M-Gdm^+ ions possess an (near-)parallel orientation to the surface.

CHAPTER 8: SURFACE pK_a OF AMINO-ACIDS Water molecules at the air/water interface possess different properties from the bulk water molecules due to the fact that the surface atoms are asymmetric in their intermolecular interactions. For instance, the acid dissociation constant (pK_a), of molecules residing at the surface may be very different from the pK_a of molecules solvated in the bulk. There are many various techniques such as potentiometric

titration, voltammetry, etc. to determine the acid dissociation constant of molecules in bulk aqueous solutions. In this chapter we present VSFG study of amino acids L-alanine and L-proline in order to determine surface pK_a. We use attenuated total reflection (ATR) spectroscopy to compare the surface pK_a with bulk pK_a. We find that the surface pK_a is substantially higher than the bulk value for both amino acids. We conclude that higher bulk pH is needed to induce the release of a proton by the carboxylic acid at the surface, due to the lack of stabilizing water. An alternative explanation would be that there exists an excess concentration of protons at the water surface (the water surface being acidic), which implies that acid dissociation at the surface requires a higher bulk pH than acid dissociation in the bulk.

8

Samenvatting

Water is zonder enige twijfel van groot belang voor zeer veel biologische processen. Het vouwen van eiwitten, zelf-assemblage, moleculaire herkenning en proton transport zijn slechts enkele voorbeelden om de noodzaak van water te illustreren. In de laatste jaren zijn verschillende spectroscopische methoden en moleculaire dynamica simulaties gebruikt om te begrijpen hoe water de functie en activiteit van biomoleculen beïnvloedt. Het beeld wat uit al deze studies naar voren komt, is dat water in de omgeving van biomoleculen duidelijke verschillen vertoont ten opzichte van bulk water, als gevolg van directe en indirecte interacties met de biomoleculen. In het algemeen is het aantal water moleculen dat beïnvloed wordt door de biomoleculen echter klein ten opzichte van de totale hoeveelheid water moleculen, wat het moeilijk maakt om de structuur en waterstofbinding van deze watermoleculen in contact met biomoleculen te meten. Bovendien zijn sommige moleculen, bijvoorbeeld oliën, slecht oplosbaar in water, wat het bijzonder uitdagend maakt het water rondom deze moleculen te meten.

Voor de bestudering van dit probleem is een techniek nodig die een onderscheid kan maken tussen de watermoleculen in de vloeistof en de watermoleculen aan het oppervlak. Vibrationele somfrequentie generatie spectroscopie (VSFG) is een techniek die specifiek gevoelig is voor watermoleculen aan het oppervlak. De oppervlaktegevoeligheid van deze techniek is gebaseerd op een niet-lineair proces wat zich alleen voordoet in het geval van symmetriebreking. Watermoleculen in de vloeistof hebben een willekeurige oriëntatie wat resulteert in een opheffing van het VSFG signaal. Aan het oppervlak, waar de symmetrie gebroken is, vindt generatie van VSFG signaal plaats. De oppervlaktegevoeligheid is de kerneigenschap van VSFG en maakt deze uniek ten opzichte van andere spectroscopische technieken.

VSFG is conceptueel vrij eenvoudig – twee gepulste laserbundels, de een met een specifieke golflengte en de ander met een breedbandig spectrum, worden in de ruimte en de tijd overlapt op een oppervlak en genereren zo een somfrequentiesignaal. De intensiteit van het gegenereerde signaal zal versterkt worden als de frequentie van het infrarode licht overeenkomt met de moleculaire vibratiefrequentie van de moleculen aan het oppervlak. VSFG spectra zijn dan ook vergelijkbaar met lineaire infrarood spectroscopische technieken, maar dan specifiek gevoelig voor de moleculen op het oppervlak. Een uitge-

breide uitleg van de VSFG theorie en van de experimentele opstelling wordt gegeven in hoofdstuk 2 en 3. In dit proefschrift is de structuur van water en de oriëntatie op het oppervlak van biologische relevante moleculen zowel met VSFG als fase-opgeloste VSFG bestudeerd.

HOOFDSTUK 4: DE WATERSTRUCTUUR AAN EEN HYDROFOOB OPPERVLAK Om de wisselwerking tussen water en hydrofobe moleculen te begrijpen, hebben we VSFG en fase-gevoelige VSFG studies uitgevoerd om de structuur en de waterstofbinding interacties van watermoleculen in contact met hydrofobe moleculen zoals alkanen en polydimethylsiloxane (PDMS) te meten. De watermoleculen aan het hydrofobe oppervlak blijken meer geordend en hebben sterkere waterstofbindingen dan aan het water-lucht oppervlak. Met behulp van fase-opgeloste VSFG metingen hebben we de absolute oriëntatie van watermoleculen kunnen bepalen en gevonden dat de meeste watermoleculen hun waterstofatomen richten naar de hydrophobe laag. Met toenemende temperatuur neemt de VSFG intensiteit af en laat het spectrum een blauwverschuiving zien, wat wijst op een verminderde ordening en een zwakkere waterstofbinding van de watermoleculen. We hebben ook onderzocht wat het effect is van de pH van de oplossing op het VSFG signaal. De meer geordende waterstructuur aan het hydrofobe oppervlak is een resultaat van een zeer gecorrugeerd oppervlak waarbij de methylgroepen die in het water steken. Het waternetwerk kan rond deze methylgroepen vouwen, hetgeen resulteert in een meer geordende waterstructuur en een sterkere waterstofbinding interactie. Verder bespreken we hoe de onbalans tussen het doneren en het accepteren van waterstofbruggen aan het hydrofobe oppervlak zou kunnen leiden tot een verhoogde hydroxide concentratie, die de waterstructuur ook meer zou kunnen ordenen. Beide verklaringen zouden van toepassing kunnen zijn op het oppervlak tussen water en hydrofobe moleculen en kunnen elkaar zelfs versterken.

HOOFDSTUK 5: HYDROFOBE HYDRATATIE EN ELEKTROSTATISCHE INTERACTIES Tetra-n-alkylammoniumzouten (TTA^+) worden vaak gebruikt als modelsystemen om hydrofobe hydratatie te bestuderen. TTA^+ kationen vertonen zowel hydrofobe en elektrostatische interacties. Daarbij rijst dus de vraag of hydrofobe hydratatie of elektrostatische interactie bepalend is voor watermoleculen rond de TTA^+ kationen. De hydrofobe interacties kunnen worden gevarieerd door het veranderen van de lengte van de alkyl-ketens. We hebben de waterstructuur en waterstofbinding onderzocht aan het oppervlak van oplossingen van tetra-n-alkylammonium bromidezouten. We vinden dat tetra-n-alkylammonium bromiden (n = 1, 2) met korte ketens de waterstructuur niet veranderen, wat verklaard kan worden door het feit dat ze niet erg oppervlakteactief zijn. Slechts een kleine blauwverschuiving en een lichte intensiteitsstijging van de VSFG spectra werd waargenomen als gevolg van de watermoleculen die waterstofbruggen vormen met het bromide ion. Daarentegen veroorzaken langketenige TAABr (n = 3, 4) kationen sterke veranderingen in de VSFG spectra. Bij lage concentraties orienteren de watermoleculen zich gemiddeld met hun dipolen richting de bulk vanwege het elektrische veld dat

wordt gecreëerd door TAA^+ -ionen in de bovenste laag en Br^- ionen dieper in de oplossing. Verrassend genoeg zijn de VSFG spectra sterk rood verschoven, in tegenstelling tot de VSFG spectra van kortketenige TAABr oplossingen, vanwegehet hydrofobe hydratatie effect. Bij hoge concentraties is de oriëntatie van watermoleculen en de verschuiving van de VSFG spectra omgekeerd ten gevolge van de clustervorming tussen TAA^+ en Br^- ionen aan het oppervlak van de oplossing.

HOOFDSTUK 6: ORIËNTATIE VAN POLAIRE MOLECULEN IN DE IN DE NABIJHEID VAN GELADEN EIWIT OPPERVLAKKEN Ureum is een van de meest gebruikte eiwitdenaturanten, maar het onderliggende mechanisme van het denaturatieproces is nog niet volledig begrepen. Er zijn experimentele bewijzen gevonden voor zowel een direct als een indirect denaturatiemechanisme. Recent bleek uit intensiteit VSFG studies van de onderzoeksgroep van Paul Cremer dat de oriëntatie van ureummoleculen aan het eiwit oppervlak afhankelijk zijn van de netto lading van het eiwit. Bovendien, volgt deze oriëntatie de richting van de watermoleculen aan het interface, wat kan worden uitgelegd als bewijs voor het indirecte mechanisme. De verandering van de ureumoriëntatie kan ook worden veroorzaakt door het omklappen van het amidegroepen van het eiwit waarmee de ureummoleculen waterstofbruggen kunnen maken. Dit zou wijzen in de richting van het directe denaturatiemechanisme. Deze mogelijkheid hebben we onderzocht door het bestuderen van de water en ureum oriëntatie en de oriëntatie van amidegroepen van α-lactalbumine met fase-opgeloste VSFG. We vonden dat de oriëntatie van de amidegroepen van het eiwit niet dezelfde pH afhankelijkheid als de ureum en de watermoleculen vertonen. Uit deze bevinding blijkt duidelijk dat het ureum niet rechtstreeks bindt aan het eiwit, wat wijst op een indirect mechanisme van de eiwitdenaturatie door ureum.

HOOFDSTUK 7: ABSOLUTE ORIËNTATIE VAN METHYLGUANIDINIUM AAN HET LUCHT/WATER OPPERVLAK Het Guanidinium kation (Gdm^+) is een ander veel gebruikt denatureringsmiddel. Het mechanisme van de denaturatie en de fascinerende hydratatie eigenschappen van de ionen zijn intensief bestudeerd met moleculaire dynamica (MD) simulaties. Deze simulaties geven aan dat de guanidiniumionen aan het wateroppervlak bij voorkeur zijn georiënteerd met hun voornaamste moleculaire vlak parallel aan het wateroppervlak. Deze voorkeursoriëntatie parallel aan het wateroppervlak is uitgelegd aan de hand van de anisotrope hydratatie van het ion. Onlangs zijn de hydratatie-eigenschappen van methylguanidinium (M-Gdm^+), een derivaat van Gdm^+, onderzocht en is gevonden dat ook M-Gdm^+ een voorkeursoriëntatie parallel aan het wateroppervlak vertoont. Wij gebruiken fase-opgeloste VSFG om de oriëntatie van M-Gdm^+ ionen aan het lucht /water oppervlak te bestuderen. We meten aan M-Gdm^+, omdat Gdm^+ volledig symmetrisch is en dus VSFG inactief. Door het meten van de polarisatie-afhankelijkheid van het VSFG signaal dat afkomstig is van methyl vibraties, en uitgaande van dezelfde hellingshoek voor alle M-Gdm^+ ionen, vinden we een kantelhoek van het moleculaire vlak van $\sim 45°$. Echter, de gegevens kunnen ook worden verklaard met een brede hoekverdel-

ingsfunctie gevormd door een half-normale verdeling gecentreerd rond 90° ten opzichte van de oppervlaktenormaal (parallel aan het wateroppervlak) en een breedte van ∼65°. We concluderen dat meer dan 80% van de M-Gdm^+ -ionen een hoek groter dan 20° heeft, waaruit blijkt dat slechts een zeer kleine fractie van de M-Gdm^+ ionen (bijna) parallel georiënteerd is aan het oppervlak.

HOOFDSTUK 8: OPPERVLAKTE pK_a VAN AMINOZUREN Watermoleculen aan het lucht/water oppervlak hebben andere eigenschappen dan bulk watermoleculen, vanwege het feit dat aan het oppervlak de intermoleculaire interacties asymmetrisch zijn. De dissociatieconstante (pK_a) van moleculen aan het oppervlak kan bijvoorbeeld heel anders dan de pK_a van moleculen in de bulk. Er zijn veel verschillende technieken zoals potentiometrische titration, voltammetrie, etc. om de dissociatieconstante van moleculen in de bulk van wateroplossingen te bepalen. In dit hoofdstuk presenteren we een VSFG studie van de aminozuren L-alanine en L-proline, met als doel om de oppervlakte pK_a te bepalen. Wij gebruiken ATR spectroscopie om de oppervlakte pK_a te vergelijken met de pK_a in de bulk oplossing. We zien dat de oppervlakte pK_a aanzienlijk hoger is dan de bulk waarde voor beide aminozuren. We concluderen dat een hogere bulk pH nodig is om de afgifte van een proton door het carbonzuur aan het oppervlak te veroorzaken, vanwege het gebrek aan stabiliserend water. Een alternatieve verklaring zou kunnen zijn dat de concentratie van protonen aan het wateroppervlak hoger is (het wateroppervlak wordt zuur), hetgeen impliceert dat de dissociatie van een zuur aan het oppervlak een hogere bulk pH vereist dan in de bulk.

8

Acknowledgements

There are so many people I want to thank that the thought that I might leave someone out terrifies me. If you already opened to read this, I believe that in one way or another you helped me along the process of completing my thesis, even if it was only a smile or a hand on my shoulder when I needed it the most. So first of all, I thank YOU.

A person whom I would never forget to thank is my supervisor Prof. Huib J. Bakker. I sincerely thank you, Huib, for giving me the opportunity to do PhD in your group, for your patience with corrections, for motivation and for your broad knowledge. I thank you most for the moments of clearance after discussing some data, which usually resulted in me leaving your office with a thought "that actually makes sense".

There are people with whom I worked directly on some projects, thus I would like to thank them. My thanks go to Dr. Ellen Backus for introducing me to SFG world and helping me on my first hydrophobes' project, to Dr. Niklas Ottoson for collaboration on methylguanidinium project and to Dr. Konrad Meister for many projects we worked on together. A special thanks to Dr. Jan Versluis for teaching me basically everything I know about how to work with laser and optics. Your help, Jan, was unmeasurable! I also want to thank Hinco, Niels and Dion for being so supportive with all the technical "thingies".

Thanks to all Bakker and Rezus former and present group members for a good atmosphere during our group discussions, coffee breaks, group uitjes and regular nights out. I am feeling very lucky that I had a chance to get to know all of you and even more lucky that many of you became more than just colleagues to me. I want to thank my former office mates: Liyuan, for all the lively chats and cups of tea we had together; Sietse, for showing me that a messy table does not necessarily mean a messy mind; Gede, for your happy Bali mood; Biplap and Johannes, for keeping sugar level in my blood extremely high during last months of writing. I thank as well: Oleg, for your critical comments on science and life, I very much admire how your mind works; Artem, for being such an inspiring friend; Stephan, for cosy evenings sometimes accompanied with piano concerts; Konrad, for your endless help on many things, I will be always thankful to you.

I would like to say thanks to my former spectroscopy group in Lithuania for a very warm welcome every time I was coming back for a visit. I also thank my friends Rimgailė and Irmantas, for always keeping in touch no matter where we all are. And thanks to my friend Julija for all the times we had in Amsterdam.

Be galo didelis ačiū mano šeimai – mamai, sesėms Ievai ir Hanai, broliui Tomui, taip pat Mykolo šeimai – Dainai, Rimui, sesei Ūlai ir močiutei Eitautei. Žinau, kad visa tai, kas parašyta šioje knygoje, jums turbūt nelabai aišku, bet Jūsų visų palaikymas man buvo svarbiausias! Labai ačiū tau, Mykolai, už šį nuotykį ir už visus nuotykius, kurie mūsų dar laukia.